MODELING AND EXPERIMENTAL INVESTIGATION OF SPINDLE DYNAMIC ERRORS AND SURFACE GENERATION IN ULTRA-PRECISION DIAMOND TURNING

HUANG PENG

Ph.D

The Hong Kong Polytechnic University

2016

The Hong Kong Polytechnic University

Department of Industrial and Systems Engineering

Modeling and Experimental Investigation of Spindle Dynamic Errors and Surface Generation in Ultra-Precision Diamond Turning

HUANG PENG

A thesis submitted in partial fulfillment of the

requirements for the degree of Doctor of Philosophy

January 2016

Certificate of originality

I hereby declare that this thesis is my own work and that, to the best of my knowledge and belief, it reproduces no material previously published or written, nor material that has been accepted for the award of any other degree or diploma, except where due acknowledgement has been made in the text.

_____ (Signed)

_____HUANG PENG_____ (Name of student)

II

Abstract

The aerostatic bearing spindle (ABS) is a vital component in ultra-precision machine tools. The performance of the ABS is an important factor in determining the machining quality in ultra-precision machining. Many studies have been conducted to measure the spindle error motions, and three typical measurement techniques, which are reversal, multi-probe and multi-step approaches, have been extensively utilized. However, few studies focus on the spindle dynamic errors. Motivated by this research gap, this study adopts theoretical and experimental approaches to study the spindle dynamic errors and their effects on the machining quality in ultra-precision machining.

The study was divided into two parts. In the first part, the spindle dynamic errors were investigated with theoretical and experimental methods. Firstly, a spindle dynamics model of ABS was developed to characterize the spindle dynamic behavior. A series of experiments, including groove cutting with diamond turning and fabrication of microstructures with slow slide servo (S^3) machining, were conducted. The theoretical and experimental results indicate that the unbalance induced eccentricity has significant effects on the machining accuracy in ultra-precision machining, even though the amplitude of spindle error motion is in the range of several tens of nanometers. The spindle has a double frequency vibration under excitations, including spindle unbalance and cutting force. The double frequency vibration can generate a low frequency enveloping

phenomenon. In addition, the results indicate that the axis average line (AAL) of the spindle rotation axis will drift away from the bearing center with increase of spindle speed due to the hydrodynamic effect of the ABS. This drift of the AAL of the spindle rotation axis with increase of spindle speed is nonlinear. The drift makes significant contribution to the machining accuracy in the fabrication of microstructures with S^3 machining, where two different spindle speeds are employed.

In the second part, a comprehensive dynamic surface generation model with consideration of the spindle dynamics, cutting mechanism and machining error is proposed. Firstly, an algorithm for the cutting force calculation and surface generation is developed. This algorithm takes into account the effect of minimum chip thickness and elastic recovery. A groove cutting experiment was conducted to verify the effectiveness of the algorithm. The experimental results indicate that the algorithm is capable of addressing the minimum chip thickness and elastic recovery in the micro cutting process. This algorithm is integrated into the comprehensive dynamic surface generation model. The simulated and measured surface topographies indicate that the low frequency enveloping phenomenon due to double frequency vibration of the spindle has a significant effect on the surface topography. The surface topography in cylindrical turning changes with different spindle speeds, even though the feed rate per revolution remains unchanged.

In ultra-precision machining, the requirement of ultra-high machining accuracy and ultra-smooth surface roughness makes the effects of spindle errors on form

accuracy and surface finish of machined components highly significant, even though the spindle errors can be down to the nanometric range. Thus, it is very significant for this research to investigate the effect of spindle errors on machining accuracy and surface roughness with experimental and theoretical methods. Based on the investigation, the spindle unbalance induced eccentricity, double frequency vibration, as well as the position drift of the AAL of the ABS have been identified. The development of the comprehensive dynamic surface generation model with consideration of spindle dynamics, effect of tool edge radius and machining error can enable optimization of the cutting conditions in ultra-precision diamond turning.

Publications arising from the thesis

Journal Paper

[1] **Huang P.**, Lee W.B., Chan C.Y., "Investigation of the effects of spindle unbalance induced error motion on machining accuracy in ultra-precision diamond turning", International Journal of Machine Tools and Manufacture, 94, 48-56 (2015).

[2] **Huang P.**, Lee W.B., Chan C.Y., "Investigation on the position drift of the axis average line of the aerostatic bearing spindle in ultra-precision diamond turning", International Journal of Machine Tools and Manufacture, 108, 44-51 (2016).

[3] **Huang P.**, Lee W.B., "Cutting force prediction for ultra-precision diamond turning by considering the effect of tool edge radius", International Journal of Machine Tools and Manufacture, 109, 1-7 (2016).

Conference Paper

[1] **Huang P.**, Lee W.B., Chan C.Y., "Tool setting error induced structure distortion in fast tool servo assisted diamond turning of micro lens array", Proceedings of EUSPEN, Leuven, Belgium, 243-244 (2015).

Acknowledgements

Foremost, I would like to express my sincere gratitude to my chief supervisor, Prof. W.B. Lee, Chair Professor of the Department of Industrial and Systems Engineering and Director of the Partner State Key Laboratory of Ultra-precision Machining Technology of The Hong Kong Polytechnic University, for his continuous support of my Ph.D. study and research. His guidance, encouragement, patience and valuable advice are of great help in enabling me finish my Ph.D. study. Besides my supervisor, I would like to thank Professor C.F. Cheung and Dr. C.Y. Chan for the inspiring discussions with them and their valuable suggestions on my research work.

My sincere thanks also go to Dr. Shaojian Zhang, Dr. Xiaodong Zhang, Dr. Minjun Ren, Dr. Peng Wang, Dr. Guoqing Zhang, Dr. Gaobo Xiao, Dr. Lingbao Kong, Dr. Xin Zhao, Dr. Hongbing Wu, and Mr. Haitao Wang for their kind help, inspiring discussions and valuable advice on my research work. Many thanks to Mr. Zhongchen Cao for his kind help on my research work as well as my personal matters. Special thanks to Mr. Zhiwei Zhu for his continuous support, encouragement, knowledge sharing, and pertinent comments helping me to improve my work.

Finally, I would like to express my utmost thanks to my parents, my brother and all my family for their support, understanding and patience during the course of my study journey.

x

Table of Contents

List of Figures

List of Tables

xx

List of Abbreviations

ABS	=	aerostatic bearing spindle
AAL	=	axis average line
AOR	=	axis of rotation
A_1, A_2, B_1, B_2	=	coefficient matrix for the steady solution under unbalance force
A_{cw}, A_{tw}	=	cutting coefficients (N/m)
A_{ct}, A_{tt}	=	cutting coefficients, dimensionless
a_x, a_y, b_x, b_y	=	coefficients related to specific nodes from A_1, A_2, B_1, B_2
CSI	=	coherence scanning interferometry
CS	=	coordinate system
C-$\xi\eta\zeta$	=	coordinate system fixed on the rigid disc
c	=	radial clearance of bearing (m)
c_{xx1}, c_{yy1}, c_{xx2}, c_{yy2}	=	damping of the spindle (N.s/m)
db	=	elemental width of cut (m)
d_{disk}	=	disk diameter (m)
$d_{spindle}$	=	spindle diameter (m)
d_1	=	relative distances between the AAL and the tip of the diamond tool in rough machining (m)

d_2	=	relative distances between the AAL and the tip of the diamond tool in S^3 machining (m)
d_e	=	relative position drift of the AAL between different spindle speeds (m)
DOF	=	degree of freedom
EFCS	=	end fly cutting servo
E	=	elasticity modulus of the spindle (N/m^2)
e	=	eccentric distance of rotor at steady state (m)
e_1, e_2	=	eccentricities of the rotor of the aerostatic bearing during the rough and S^3 turning, respectively (m)
e_ξ, e_η, e_ζ	=	coordinates of the unbalance mass in the coordinate of C-$\xi\eta\zeta$
F_{bx1}, F_{by1}, F_{bx2}, F_{by2}	=	reaction forces from the two bearing at the ends of spindle (N)
FTS	=	fast tool servo
FRF	=	frequency response function
F_c	=	cutting force (N)
F_t	=	thrust force (N)
G_1	=	gyroscopic matrix of the spindle system
G_l	=	mesh point subset of G_{swept}
$G_{\hat{\theta}_t}$	=	mesh point set related to $S_{\hat{\theta}_t}$
G_{swept}	=	mesh point set swept by the cutting tool
h	=	local film thickness of bearing (m)

J_d	=	diametric moment of inertial of rigid disc $(Kg.m^2)$
J_p	=	polar moment of inertial $(Kg.m^2)$
K_1	=	stiffness matrix of the spindle system
K_{cc}, K_{tc}	=	cutting force coefficients (N/m^2)
K_{te}, K_{ce}	=	cutting force coefficients (N/m)
k_{xx1}, k_{yy1}, k_{xx2}, k_{yy2},	=	stiffness of the spindle (N/m)
L	=	length of bearing (m)
$l_{spindle}$	=	spindle length (m)
m_{Disc}	=	mass of the rigid disc (kg)
m_p	=	unbalance mass (kg)
M_1	=	mass matrix of the spindle system
N_1, N_2	=	shape functions of Timoshenko beam
n	=	spindle speed (rev/min)
n_1, n_2	=	spindle speeds used in rough turning and S^3 machining respectively (rev/min)
nFTS	=	nano fast tool servo
PSI	=	phase shifting interferometry
PSD	=	position sensitive device
P	=	pressure at the feeding hole (N/m^2)
P_s	=	supply pressure (N/m^2)
q_x, q_y	=	coordinates of the spindle shaft
Q_x, Q_y	=	coordinates of the nodes of the system

RTT	=	rotating tools turning
R	=	radius of bearing (m)
$round(\cdot)$	=	rounding operator
S^3	=	slow slide servo
SPDT	=	single point diamond turning
STR	=	surface topography repeatability
$S_{\hat{\theta}_t}$	=	workpiece surface point set at azimuth $\hat{\theta}_t$
S_{swept}	=	workpiece surface point set swept by the cutting tool
S_{update_l}	=	updated surface point set related to G_l
${}^i_j T_P$	=	initial position transformation matrix
${}^i_j T_{Pe}$	=	initial position error transformation matrix
${}^i_j T_S$	=	ideal motion transformation matrix
${}^i_j T_{Se}$	=	error motion transformation matrix
t_c	=	elemental uncut chip thickness (m)
$t_{c\min}$	=	minimum chip thickness (m)
$t_{c\max}$	=	upper limit of chip thickness for elastic recovery (m)
t_{disk}	=	disk thickness (m)
$t_{elastic}$	=	elastic recovery (m)
3-D		three dimensional
UHS	=	ultra high speed
u, v	=	translation displacement of the spindle (m)

X_0, Z_0	=	initial positions of cutting tool tip in the reference coordinate system
$\mathrm{x_t}$, $\mathrm{y_t}$	=	coordinates of the tool tip in inertial coordinates
x_{O_s}	=	coordinates of the intersection point O_s of AAL and OXY plane (m)
$x_{O_s'}$	=	coordinate of the new intersection point O_s' of AAL and OXY plane due to position drift of AAL (m)
z	=	axial coordinate of bearing (m)
z_a, z_b	=	boundary coordinates of axial coordinate of mesh points
δ_{xij}^P, δ_{yij}^P, δ_{zij}^P	=	initial translational position error along the X, Y and Z axes
δ_{xij}^S, δ_{yij}^S, δ_{zij}^S	=	translational motion error along X, Y and Z axes
ε_{xij}^P, ε_{yij}^P, ε_{zij}^P	=	initial angular position error around X, Y and Z axes
ε_{xij}^S, ε_{yij}^S, ε_{zij}^S	=	angular motion error around X, Y and Z axes
Ω	=	spindle speed (rad/s)
ε	=	eccentricity ratio of bearing
θ	=	angular coordinate of bearing (rad)
θ_0	=	initial azimuth of the tool tip in the workpiece cylindrical coordinate system

		(rad)
$\hat{\theta}_t, \hat{z}$	=	nearest mesh point of the coordinates of the cutting tool tip in the workpiece cylindrical coordinate system
μ	=	dynamic viscosity of lubricant (N.s/m^2)
ν	=	Poisson's ratio
ξ_t, η_t	=	trajectory of the tool tip in the coordinate of C-$\xi\eta\zeta$
ρ_t, θ_t, z_t	=	coordinates of the cutting tool tip in the workpiece cylindrical coordinate system
$\rho(\cdot)$	=	surface height of the workpiece at the corresponding mesh point
$\rho_{spindle}$	=	spindle mass density (kg/m^3)
ρ_{disk}	=	disk mass density (kg/m^3)
φ	=	attitude angle of the rotor at steady state (rad)
φ_1, φ_2	=	corresponding attitude angle during rough and S^3 turning (rad)
χ	=	shear factor
ϕ_i	=	azimuth angle of the elemental thrust force (rad)
ϕ_x, ϕ_y	=	rotation angles of the spindle (rad)
ω	=	spindle speed (rad/s)

Chapter 1 Introduction

1.1 Background

With the development of industry, the demand of high precision components is increasing in many fields, such as optics, biomedicine, and astronautics. This makes ultra-precision machining an important machining process which can produce high precision components with a nano-metric surface roughness and a sub-micrometric form tolerance. For instance, ultra–precision diamond turning can be used to fabricate rotational symmetric parts such as spherical and aspherical parts with sub-micrometric form accuracy (Lee et al. 2000). With the assistance of fast tool servo/slow slid servo, a functional surface with micro-scale structures can be fabricated (Kong et al. 2010). The quality of fabricated parts can be estimated by the form accuracy and surface roughness. They are governed by many factors such as machine tool performance, process parameters (spindle speed, feed rate, cutting depth etc.), tool wear, material properties (material pile up, swelling and recovery etc.).

The aerostatic bearing spindle is extensively employed as a vital component for ultra-precision machine tools, and spindle error motions provide a critical indicator. For an ultra-precision machine, many aspects such as slide motion accuracy, stiffness, damping and thermal stability have been greatly improved relative to conventional machines, however the effect of spindle error motions on

the form and surface finish of machined parts can become large, even though their amplitude is normally a few tens of nanometers in an ultra-precision machine. Therefore, many measurement techniques, including the reversal method, the multi-probe and multi-step method (Marsh et al. 2006) have been proposed to evaluate the performance of spindle at operating speeds. The measured spindle error motions consist of synchronous and asynchronous components. The former contribute to the form error and the latter to the surface finish. Most measuring processes are usually conducted during air cutting, and this makes the effect of spindle dynamics in actual machining overlooked. In some ultra-precision machining processes, such as fast tool servo/slow slide servo and raster milling, the cutting force may be intermittent and can excite the spindle to vibrate, and the unbalance induced eccentricity can contribute to the form error. Therefore, it is necessary to understand the spindle dynamics characteristics during the ultra-precision machining process with theoretical and experimental methods.

With regard to the machining dynamics, the cutting force is a very important parameter. Many cutting force models based on orthogonal cutting have been proposed in the past (Merchant 1945). These cutting force models are used for a number of specific machining processes such as turning, milling and grinding. In addition, some studies calculate the cutting force by taking into account certain factors including the cutter vibration and run out (Wang et al. 2015). Most

cutting force models are based on the sharp tool edge assumption, and this is reasonable enough in conventional cutting. For ultra precision machining, the cutting depth can be down to several micrometers and is comparable to the cutting tool edge radius. This makes the effect of the cutting tool edge radius significant and some models have been established by considering such effect (Fang 2003). Therefore, there is need to calculate the cutting force in a specific ultra precision machining process by taking into consideration the effect of the tool edge radius.

A surface generation model is an efficient method to simulate and predict the surface finish under given cutting conditions. Generalized models have been proposed to predict the surface topography in manufacturing processes by considering certain errors such as tool run out and machine deformation (Ehmann and Hong 1994). Some models which take into account the vibrations in turning have also been proposed (Lin and Chang 1998, Cheung and Lee 2000). Tool vibration is considered in predicting the surface topography in peripheral milling (Arizmendi et al. 2009). However, the machining and spindle dynamics have been overlooked in most established models. There is a need to fill such a research gap and develop a surface generation model to predict and optimize the surface quality by considering the machining and spindle dynamics.

1.2 Research Objectives

The research aims to investigate the effect of spindle dynamics on the ultra-precision machining process with theoretical and experimental methods,

and to develop a dynamic model to predict the surface generation by consideration of the influence of the tool edge radius in ultra-precision machining. The objectives of the research are:

(1) To investigate the influence of spindle dynamic errors on the machining accuracy in ultra-precision machining.

(2) To establish a spindle dynamic model which takes into account the excitation under spindle unbalance and the cutting force.

(3) To develop a dynamic surface generation model for predicting the machined surface topography taking into consideration the spindle dynamics in ultra-precision machining.

1.3 Organization of the thesis

The thesis contains seven chapters. In Chapter 1, the background of the spindle error motions and surface generation modeling in ultra-precision machining is discussed, and the challenges to be overcome are presented. Chapter 2 gives a literature review of a variety of machining techniques for ultra-precision machining, the measurement approaches of spindle error motions and current research on the modeling of surface generation.

In Chapter 3, a spindle dynamics model is developed to analyze the dynamic characteristics of the aerostatic bearing spindle and the effects on the machining error in the case of spindle unbalance. A series of cutting experiments are also conducted to identify the influences of spindle dynamics.

In Chapter 4, the drift of the spindle rotation axis of the aerostatic bearing spindle

at different spindle speeds, due to the hydrodynamic effect, is discussed. Its effect on the fabrication of the microstructure with slow slide servo machining is investigated in a specially designed experiment.

Chapter 5 and Chapter 6 discuss the development of the comprehensive dynamic model for surface generation. In Chapter 5, an algorithm for computing the cutting force and surface topography is firstly proposed. In the algorithm, the cylindrical workpiece is discretized and the position and attitude of the cutting tool is described in workpiece coordinates. The algorithm of the cutting force calculation and the surface updating is developed with consideration of the concept of minimum chip thickness and elastic recovery in micro cutting.

In Chapter 6, a comprehensive dynamic model for surface generation is established by taking into account the spindle dynamics, cutting mechanism and machining error model. The spindle dynamics are discussed in Chapter 3 and Chapter 4, and the cutting mechanism is discussed in Chapter 5, and only the machining error model is discussed in Chapter 6. Based on the comprehensive dynamic model, the surface topography, with consideration of the machining dynamics, can be obtained.

Chapter 7 makes the overall conclusions for the thesis, and gives some suggestions for future studies.

Chapter 2 Literature review

2.1 Ultra-precision diamond turning

Ultra-precision diamond turning is extensively utilized to fabricate parts with high accuracy. This technology is suitable for producing rotational symmetric and free form components with nanometric roughness and form error as low as the sub-micrometer level (Cheung and Lee, 2000). Diamond turning normally adopts a single crystal diamond tool with a very sharp tool edge (Ikawa et al. 1991). This allows diamond turning to be used to fabricate optical components made of non-ferrous materials including aluminum, brass, copper, silver and gold (Cheung and Lee, 2001).

In terms of ultra-precision diamond turning, the Large Optics Diamond Turning Machine (LODTM) is the representative machine tool, and is still the most accurate machine tool over the world (Meinel et al. 1986). This machine was built to fabricate large scale optical components at the Lawrence Livermore National Laboratory (LLNL). The LODTM is capable of machining a workpiece with a maximum size of 1.65 meter diameter and 0.5 meter length, with mass up to 1360 kilograms (Donaldson and Patterson, 1983; Estler, 1985). The rotating speed of the workpiece is about 50 rpm. To determine the position information of the cutting tool and workpiece, an interferometer system and capacitance gauges are adopted. The air temperature is maintained at a constant value within 0.01°F by the air conditioning system while the temperature of the water used to control

the temperature of the LODTM system is conditioned to a constant value within 0.001°F(Donaldson and Patterson, 1983). Due to these excellent designs, a machining accuracy of 28 nanometers can be achieved by LODTM. Other commercial ultra-precision diamond machines also have been built by many famous companies. Some representative commercial machines include Nanotech 450UPL from Moore Nanotech. Company, Nanoform 700 ultra from Precitech Company, and MTC400 from LT Ultra Company etc..

In the diamond turning process, the spindle rotates at a constant speed while the X and Z linear axes are controlled to generate a given trajectory. Therefore, diamond turning only can be utilized to produce rotationally symmetric parts. To fabricate more complicated components such as compound eyes, off-axis aspheric mirrors, the slow slide servo (S^3) method is extensively applied (Yi and Li 2005; Yin et al. 2011). For the S^3 method, the spindle axis becomes a C-axis and the angular position of the C-axis can be precisely controlled by equipping with a high-precision encoder. The X, Z and C-axes will have accurate motions according to the designed tool path, which is generated in cylindrical coordinates, with consideration of tool nose radius compensation (Tohme 2004). Compared to the fast tool servo (FTS), S^3 is suitable for machining surfaces which are comprised of low frequency components. This is due to the fact that the Z-axis is heavy and driven by the motor with limited speed and acceleration (Fang et al. 2013). However, S^3 can produce parts with better surface quality, high accuracy, and a larger travel range in the Z-axis direction than FTS.

For the tool path generation of S^3, the tool nose radius, included angle, rake angle

and the clearance angle need to be considered when the tool path is generated in cylindrical coordinates (Fang et al. 2008; Fang et al. 2013 and Zhang et al. 2009). To fabricate off-axis, with a large ratio of sag height to diameter, Zhang et al. proposed a coordinate transformation method to decrease the normal angle, included angle and range of tool oscillation, which are obstacles in the conventional S^3 method (Zhang et al. 2013a). Yi and Raasch utilized S^3 to produce a high-order phase-correction plate which was applied to correct the wavefront error of human eyes (Yi and Raasch 2005). To reduce the effect of alignment error on the form error, Zhang et al. machined a compound eye lens with an off-center machining configuration (Zhang et al. 2013b). It is difficult for S^3 to machine three freeform surfaces on one prism, therefore, Zhang et al. proposed a rotating tool turning (RTT) method to solve the problem (Zhang et al. 2012). In this method, two cutting tools are mounted on the spindle while the workpiece is fixed on a rotating table.

As the S^3 machining process is conducted in cylindrical coordinates, three inherent disadvantages exist that limit the machining for microlens arrays over large area: (a) the cutting velocity changes along the radial direction leading to inconsistent surface quality over the cutting area; (b) to reduce the effect of varying interpolation error along the radial direction, numerous sampling points must be used for machining over a large area; (c) the limitation of the tracking bandwidth of the servo system will restrict the spindle speed and can distort the machined lenslet (Zhu et al. 2015). Motivated by this, Zhu et al. proposed a novel end-fly-cutting-servo (EFCS) method to produce a microlens array over a large area (Zhu et al. 2015). Based on this method, they machined a microlens

array over a very large area. Their results indicate that all the lenslets over the large area have uniform quality. In addition, the volume of the machining data is significantly reduced and high machining efficiency is obtained.

Diamond turning with the assistance of a fast tool servo (FTS) has the similar configuration as that of XZC S^3 machining. In the FTS machining process, the workpiece is mounted on the spindle and rotates with a constant speed. The X-slide moves with a constant speed while the cutting tool is driven by the FTS unit along the Z-axis direction. The FTS can obtain a higher oscillation frequency, but shorter stroke range along the Z-axis direction, than the S^3 machining process.

Patterson and Magrab developed the first FTS which was employed to compensate for the spindle error motions (Patterson and Magrab 1985). FTS can be categorized according to different mechanisms into: piezoelectric FTS, Lorentz force FTS, magnetostrictive FTS, and normal-stress electromagnetic FTS and so on (Trumper and Lu, 2007). Most of the FTS have strokes from 10μm to 6 mm and the bandwidths are in the range of 20 Hz to 2 kHz (Brinksmeier et al. 2010). For the precision turning of a cylindrical shaft, Altintas and Woronko developed a FTS which had a stroke of 36 μm, 3.2 kHz natural frequency and 370 N/μm stiffness (Altintas and Woronko 2002). Lu and Trumper built an ultrafast tool servo with a stroke of 30 μm at a bandwidth of 23 kHz (Lu and Trumper, 2005). Generally, a FTS with long stroke usually has a low bandwidth while a FTS has a high bandwidth if it has a short stroke. To solve this problem, most studies have focused on the development of a hybrid FTS,

including the combination of a piezoelectric actuator and linear motor (Weck et al. 1995; Elfizy et al. 2005), as well as a piezoelectric actuator and voice coil motor (Liu et al. 2010; Liu and Li, 2010).

FTS assisted diamond turning is extensively utilized for the fabrication of optical free form surfaces. For instance, Gao et al. adopted a piezoelectric FTS, which had a bandwidth of 2.5 kHz, to produce a large area sinusoidal grid surface (Gao et al. 2003). Brinksmeier et al. developed two nano-FTSs (nFTS), which have strokes of 500 nm and 350 nm with bandwidths of up to 5 kHz and 10 kHz respectively, producing submicron structured surfaces with nanometer precision (Brinksmeier et al. 2010). Yu et al. developed a FTS to fabricate a micro-structured functional surface on brittle material with ductile regime machining (Yu et al. 2011). Another important application of FTS is noncircular turning (Wu et al. 2007). To meet the requirement of long travel, high frequency and high precision in noncircular turning, Ma et al. designed a new flexure structure to amplify the output of the piezoelectric actuator (Ma et al. 2005). A flexure hinge mechanism with motion magnification was proposed by Wang and Yang to amplify the output displacement of a piezoelectric actuator (Wang and Yang 2013). A further application of FTS is in error compensation, where the FTS is usually employed to compensate for the machining error of the machine tool and the deformation of some thin wall workpieces (Kim et al. 2004; Gao et al. 2007; Stoebener and Dijkman 2007; Beekhuis et al. 2009; Beekhuis et al. 2012).

Apart from the FTSs with one linear motion, some FTSs with rotary motion or

multi degrees of freedom have also been proposed in a number of studies. To fabricate ophthalmic lenses, Ludwick et al. proposed a novel rotary fast tool servo (Ludwick et al. 1999). The tool arm is driven by a brushless motor. Two sets of angular-contact ball bearings are utilized to constrain the shaft which is used to clamp the tool arm. This rotary fast tool servo provides a high acceleration of 500 m/s^2 at the tool tip. Zhu et al. proposed a two-degrees-of-freedom (DOF) fast tool servo (Zhu et al. 2014). Based on this 2-DOF fast tool servo, they developed a pseudo-random diamond turning method to produce freeform optics with scattering homogenization (Zhu et al. 2013)

2.2 Error sources of machine tools

2.2.1 Overview of Error sources

There are a variety of error sources which can contribute to the machining accuracy of machine tools. The contributions of these error sources to the machining accuracy are dependent on the machine's structure loop, which includes the spindle, the linear guideway, the tool holder and the workpiece fixture. The major error sources can be categorized as: kinematic errors, thermal errors, and load induced errors (Sartori and Zhang 1995; Schwenke et al. 2008; Mekid and Ogedengbe 2010).

Kinematic errors are induced from the imperfect geometry and dimensions of machine's components, the errors of the relative locations of these components and the errors of the measurement system of the machine tool (Bryan 1982a; Bryan 1982b; Knapp 1983; Donmez and Blomquist 1986 ; Soons 1992;

Schwenke et al. 2008;). Moreover, these kinematic errors can be categorized into component errors and location errors (Schwenke et al. 2008).

In terms of component errors, a linear movement contains six component errors, including one positioning error, two straightness errors, one roll error and two tilt errors. For a rotational movement, the component errors include one axial error, two radial errors, one angular error and two tilt errors. The location error of a linear or rotational axis is an error between the ideal and actual position and orientation of the axis in the machine coordinate system (Schwenke et al. 2008). For a three linear axis milling system, it contains component errors and location errors, and this machine has 21 kinematic error components, including positioning errors, straightness errors and angular errors of each linear axis, as well as squareness errors (Ni 1997; Mekid and Ogedengbe 2010).

The thermal errors of machine tool are generated by various internal and external heat or cold sources of machine tools, including heat from the drive motors, the cutting heat, friction, the environment temperature and cooling system of the machine tool (Schwenke et al. 2008; Mekid and Ogedengbe 2010). Besides, the expansion coefficient differences of the machine part materials and the non-uniform temperature distribution can also contribute to the thermal distortion of machine tools (Balsamo et al. 1990; Schwenke et al. 2008). The thermal errors are time-varying errors, and this requires that they be compensated by real time compensation methods (Yang and Ni 2005a; Yang and Ni 2005b; Mekid and Ogedengbe 2010).

The stiffness of a machine is finite and the structure of the machine cannot be regarded as a rigid body. Thus, some errors can be caused by the loads, including cutting forces, the weight of the moving components, the inertial force induced by the acceleration/ deceleration of the motion axis and structural vibration (Schellekens et al. 1998; Ramesh et al. 2000; Okafor and Ertekin 2000; Schwenke et al. 2008; Mekid and Ogedengbe 2010). If the weight of a moving slide makes the guideway bend, the load induced errors are usually converted to a straightness error in the vertical direction and a pitch error of the moving axis (Schwenke et al. 2008).

Apart from the error sources mentioned above, some other error sources can also have contributions to the accuracy of machine tools. These error sources includes fixturing error, tool wear, following error, interpolation error and tool alignment error and so on (Ramesh et al. 2000; Lee et al. 2000; Schwenke et al. 2008; Mekid and Ogedengbe 2010).

2.2.2 Measurement of Error sources

The measurement methods for the geometric errors can be categorized into direct and indirect method (Schwenke et al. 2008). The direct measurement methods only measure single errors of a single axis, and no other axes are involved during the measuring process. As opposed to the direct method, the indirect measurement methods require that two or more axes should move simultaneously during the measurement.

2.2.2.1 Direct measurement of machine tool error

Metrological references, including artifacts and linear propagation and wavelength of laser light are extensively adopted in the direct measurement methods. The typical artifacts for direct measurement methods include the straightedge, step gauge and line scale etc. For instance, Gao et al. employed a straightedge to measure the straightness error of the X-axis of the diamond turning machine (Gao et al. 2007). The straightedge was made of Zerodur material which is insensitive to change of temperature. To improve the measuring accuracy, the reversal method was adopted to separate the straightness error from the surface error of the straightedge.

The laser interferometer is a common instrument used for the direct measurement of single errors in machine tools. It can be used to measure the positioning error, straightness error and angular error by adopting different reflectors (Gao et al. 2006; Schwenke et al. 2008). The effect of yaw error of a linear motion axis on the straightness measurement with the laser interferometer under the condition of moving reflector and moving prism has been analyzed by Gao et al. (Gao et al. 2006). The autocollimator is also an important instrument for angular error measurement (Gao et al. 2006). In addition, the position sensitive device (PSD) is also used for direct measurement (Liu et al. 2005; Sze-Wei et al. 2007).

2.2.2.2 Indirect measurement of machine tool error

For indirect measurement methods, one type of indirect method is to place artifact into the working space of the machine tools, and then these artifacts are measured. Some classical examples for this type of indirect measurement are the

measurement of 1D, 2D artefacts and 3D ball plates. The 1D or 2D artifacts are placed in different positions of the working space, and then the coordinates of these artifacts are measured (Kunzmann et al. 1990; Trapet and Wäldele 1991; Trapet et al. 2006). The error vectors, which are the superimposed errors of the kinematic errors of the machine tools, can be detected by comparing measured data with the calibrated coordinates. The 3D ball plate measurement can generate a spatial grid of measurement points based on a set of spacers in the working space with different heights. The spatial grid of measurement data can be directly used as the compensation vectors, where the machine error model is not needed (Schwenke et al. 2008).

Another type of indirect measurement method is called contour measurement, which makes two or more axes simultaneously move along specially designed lines in the working space of machines (Schwenke et al. 2008). These lines can be straight lines, circular paths and so on (Knapp and Weikert 1999; Bryan 1982a; Bryan 1982b; Kakino et al. 1987; Ziegert and Mize 1994; Pahk et al. 1997; Tsutsumi and Saito 2003). The ball bar, for instance, is extensively used for indirect measurement with circular paths, where the circular paths can be generated by two linear axes (Bryan 1982a) or two linear and one rotary axes (Tsutsumi and Saito 2003). The application of the ball bar is usually limited due to its limited stroke (Schwenke et al. 2008). Considering this limitation, a Lasertracer was developed by combining the conventional laser interferometer and the ball bar (Schwenke et al. 2005; Umetsu et al. 2005).

Multilateration measurement is a type of indirect measurement, which utilizes

direct measurement equipment for measurement with different locations and orientations (Schwenke et al. 2008). Zhang et al. developed a displacement method to identify the geometric errors of three–axis machine tools by measuring the displacement errors along 22 lines in the working space of a machine tool (Zhang et al. 1988). The measuring accuracy of squareness, yaw and pitch errors of the machine tool can be dramatically improved based on this method. Chen et al. improved the displacement method by measuring the displacement errors only along 15 lines in the work volume of the machine tool (Chen et al. 2001). Chapman analyzed the limitations of the laser diagonal method, and the loss of measurement accuracy was revealed (Chapman 2003).

In addition to the above mentioned methods, chase-the-ball measurement is also a kind of indirect measurement, where the relative position, as well as the orientation between the tool/probe and the workpiece, remains nominally unchanged when two or more axes move simultaneously. The geometric errors of the machine tool will lead to relative movement between the tool/probe and the workpiece. The R-test is a representative method for chase-the-ball measurement (Weikert 2004; Bringmann and Knapp 2006; Bringmann and Maglie 2009; Ibaraki et al. 2011), and is usually applied to rapidly evaluate the geometric errors of five-axis machine tools including location errors and angular positioning errors of the rotary axes. In addition, the R-test is also used to determine the dynamic accuracy of the 3D path (Ibaraki et al. 2011).

There are two identification methods that are commonly applied to identify the geometric errors in measured data from indirect measurement, including the

analytical method and best fit method (Schwenke et al. 2008). The former is usually adopted for the indirect measurement by using a calibrated artifact and contour measurement, whereas the latter is used for displacement and chase-the-ball measurement.

2.3 Spindle error motion

The spindle is a vital part of a machine tool and it is essential to ensure that the spindle error motion has a small effect on the machining accuracy. The error motion of a spindle contains three spatial components: radial, axial and tilt error motions. These error motions consist of two different kinds of components: asynchronous and synchronous error motions. This classification is dependent on the frequency of the error motion. The asynchronous error motions prevent the spindle from following the same path for each revolution (Martin et al. 1995). The asynchronous error motions contribute to the surface finish while the synchronous error motions have influence on the geometry of the machined part. Compared with the rolling-element bearing spindle, the air bearing spindle has only one rotational element and this makes the amplitude of its error motion relatively low, so the air bearing spindle is extensively adopted in ultra precision machining when a mirror surface finish is required (Devitt 2009).

2.3.1 Measurement with spindle error separation

The general method for measuring the spindle error motions is by using probes to measure the motion of an artifact which is attached to the spindle rotor. The measuring data of this method includes the out-of-roundness of the artifact and the spindle error motions. Thus, it is important to separate the spindle error

motion from the form error of the artifact. To solve this problem, three typical techniques: the reversal method (Donaldson 1972; Marsh et al. 2006; Marsh et al. 2010), the multi-probe method (Whitehouse 1976; Zhang et al. 1997; Estler et al. 1997; Marsh et al. 2006; Marsh et al. 2010) and the multi-step method (Whitehouse 1976; Tong 1996；Estler et al. 1997; Marsh et al. 2006) have been proposed.

The reversal technique is extensively utilized to separate the form error of the artifact from the spindle error motion (Donaldson 1972; Evans et al. 1996). This method needs two measurements to separate the artifact form error from the spindle error motion by rotating both the artifact and the probe 180° between the two measurements. Theoretically, the reversal technique can entirely separate the two errors. Nevertheless, it is difficult to achieve perfect fixturing, accurate rotation angles and data synchronization in reality (Marsh et al. 2010). The centering error during the measuring process with the reversal technique has significant influence on the measurement accuracy and results in the highest measurement uncertainty compared with the other two techniques (Cappa et al. 2014). To calibrate a precision spindle, Grejda et al. designed a new configuration by adopting a rotary table, reversal chuck and stationary displacement sensor to implement the Donaldson and Estler reversal without moving and realigning the displacement sensor (Grejda et al. 2005).

Multi-step and multi-probe techniques are alternative methods to the reversal technique. In the multi-step technique, the probe remains stationary during the measuring process, whereas the artifact is sequentially indexed in a number of

equally spaced increments (Marsh et al. 2006; Marsh et al. 2010). The multi-probe technique utilizes three or more probes to target the artifact simultaneously for the measurement. However, the multi-step and multi-probes techniques are not sensitive to certain harmonics of the error motion (Whitehouse 1976; Tong 1996). For the multi-probe technique, the effect of this problem can be reduced if the number of probes and their angular positions are well-considered, whereas this effect can be reduced by increasing the number of measurements in the multi-step technique (Cappa et al. 2014).

The measuring accuracy of the conventional three-probe method can be affected by factors such as the approximation errors of the governing equation of the method, artifact size effect and mounting error of the probe. Therefore, Tu et al. proposed an exact model to analyze the influence of these factors on the measuring accuracy (Tu et al. 1997). Gao et al. developed a mixed method to measure the workpiece roundness and spindle error motion by using two optical sensors (Gao et al. 1996; Gao et al. 1997a). This method is different from the traditional three point method as it can measure the high frequency components effectively. Zhang et al. proposed a new multi-point method to measure the spindle error motion and workpiece roundness simultaneously (Zhang et al. 1997). This method can resolve the harmonic suppression problem which exists in the three point method. They used four probes to measure the radial spindle error motion, and the axial and tilt error motions were measured by adopting five probes. The measuring accuracy of this method is dependent on the accuracy of the adopted probes. Their method is capable of measuring spindle error motions in real time. Nevertheless, they have not evaluated the measurement uncertainty

as the error motion value significantly varied in each run. The angular error motion of the spindle is usually measured by simultaneously measuring the radial error motion at two different axial positions along the spindle axis. To simplify the measurement, Gao et al. developed a new three-point angular method which utilize 2D slope sensors (Gao et al. 2002). This method can measure the spindle radial and angular error motion and the out-of-roundness of the artifact simultaneously. Liu et al. proposed a new spindle error measurement system, where the artifact used in traditional methods is replaced by a rotational fixture which contains a built-in laser diode (Liu et al. 2004). Gao et al. discussed the generalized three-point method and the sequential three-point method for expressing stepwise variation of the profile, and then they developed a combined three-point method for on-machine roundness measurement of a cylindrical workpiece (Gao et al. 1997b).

Marsh et al. pointed out that the Donaldson reversal, the multi-probe and the multi-step technique are all capable of measuring the sub-nanometer features in spindle error motion and artifact form, and they also discussed some important details for spindle error motion measurement at the nanometer level (Marsh et al. 2006). To separate the artifact form error and the spindle error motion with a sub-nanometer measurement uncertainty, Cappa et al. analyzed the error sources of three separation methods including the Donaldson reversal, the Grejda reversal and the multi-probe technique (Cappa et al. 2014). Based on the analysis, they developed an improved multi-point method which can accurately index the sensors and artifact. The measurement uncertainty of their method was four times smaller than the multi-point method. By optimizing the measurement angle, the

suppression of low-order harmonics was reduced. The test results indicated that the measurement uncertainty was 0.455 nm.

Many studies also pay attention to the measurement of some special spindles, such as heavy or miniature spindles. It is difficult to directly use the reversal method to separate the form error of large scale roll and spindle error motion as the workpiece is too heavy to be reversed. To solve this problem, Lee et al. reversed the spindle instead of the roll workpiece which was held by a crane to remain stationary (Lee et al. 2014). Anandan and Ozdoganlar proposed a multi-orientation error separation technique to separate the artifact form error and spindle error motion of a miniature ultra-high-speed (UHS) spindle, where the orientation of the artifact relative to the spindle was precisely measured by the reflectivity measurement of marks on both the artifact and the spindle (Anandan and Ozdoganlar 2015).

When measurement with an artifact is conducted at very high spindle speed, the unbalance induced by the installation of the artifact will generate additional error motion. In addition, the measured error motion with the artifact is different from the error motion in the machining process where the cutter induces additional error motion. In consideration of this, Nakkiew et al. proposed a new method which employs cutting marks to quantify the radial error motion in end milling (Nakkiew et al. 2006).

Fujimaki and Mitsui utilized an auto-collimation to develop an optical system for measuring the radial error motion of a miniature ultra-high-speed spindle

(Fujimaki and Mitsui 2007). Anandan and Ozdoganlar presented a laser Doppler vibrometry-based methodology to measure the axial and radial spindle error motion of a miniature ultra-high-speed spindle (Anandan and Ozdoganlar 2013a). Based on the proposed measurement system, they analyzed the axial and radial error motions of a hybrid ultra-high-speed spindle with ceramic bearing (Anandan and Ozdoganlar 2013b). They found that the spindle speed combined with the thermal state and over-hang length of artifact or tool had a dramatic effect on the measured spindle error motion for their miniaturized spindle at ultra-high spindle speeds. In addition, their results also indicated that the cyclic variation of the spindle temperature resulting from the nature of the coolant controller significantly affected the spindle error motion. To measure the five degrees of freedom error motion of a high speed micro spindle simultaneously, Murakami et al. developed an optical measurement system and the major measurement errors were also analyzed in detail (Murakami et al. 2010; Murakami et al. 2014).

Current measurement standards assume that there is no fundamental radial error motion in spindle error motion (ANSI/ASME B89.3.4M, 1985 and ISO 230-7:2006). The once per revolution component in the measurement result is attributed to the eccentricity of the artifact installation. This is reasonable for application in a single fixed radial sensitive direction, even though the unbalance induced eccentricity exists (Knapp and Arneson 2014). For other applications the fundamental radial error component of the spindle can have an effect on the machined feature. Lu and Jamalian proposed a 2D method to analyze the radial error motion based on specific applications, and their theoretical and

experimental results indicated that the fundamental component definitely exists in spindle radial error motion (Lu and Jamalian 2011, Lu et al. 2011).

2.3.2 Factors affecting spindle error motion

The spindle error motions can vary with different spindle speeds. Martin et al. analyzed the spindle error motion with a number of experimental tests (Martin et al. 1995). Their tests were conducted at different spindle speeds used for actual machining, and the tests showed that the spindle error motions change with spindle speed. This reveals that the spindle error motions must be measured at the operation speed which is used in the machining process. Lee et al. measured the spindle error motions of a large precision roll lathe based on the reversal method at different spindle speeds (Lee et al. 2012).

Ohishi and Matsuzaki conducted an experimental study to explore the thermal characteristics of the aerostatic journal bearing of a spindle (Ohishi and Matsuzaki 2002). Based on their experimental results, they concluded that the radial heat flow dominated compared with the axial heat flow. The temperatures and the square of spindle speed have a proportional relation. In addition, the temperature along the circumferential direction had a uniform distribution. Chen and Hsu characterized and modeled the thermal growth of a motorized high speed spindle with a ball-bearing (Chen and Hsu 2003). Their study revealed that the dynamic history and spindle speed have a significant impact on the thermal

growth of a high speed motorized spindle. Srinivasa et al. employed a laser ball bar to measure the spindle thermal drift of a machine tool (Srinivasa et al. 1996). Yang et al. measured the spindle thermal errors by adopting a hemispherical ball bar test (Yang et al. 2004).

The form error of a spindle star pattern due to dynamic imbalance has been observed on a machined surface with a magnetic bearing spindle (Khanfir et al. 2005). Marsh et al. investigated the effect of the relation between spindle speed and dominant resonant frequency on workpiece flatness in precision fly cutting (Marsh et al. 2005). Zhang et al. developed a five-degrees-of-freedom dynamic model to analyze the dynamic characteristics of an aerostatic bearing spindle and its effect on surface generation (Zhang et al. 2012). Tauhiduzzaman et al. conducted a series of experiments to investigate the spindle star pattern on the a diamond turned surface and they concluded that the imbalance of the spindle is the main reason (Tauhiduzzaman et al. 2015). Bediz et al. applied fiber-optic laser Doppler vibrometers to characterize the spindle dynamics of a miniature ultra-high-speed spindle (Bediz et al. 2014). Their experimental results revealed that the spindle speed has a significant influence on the natural frequency and damping ratio of the spindle. In addition, the whirling mode pairs of the spindle can split with increasing spindle speed because of the gyroscopic effect.

2.3.3 The effect of spindle error on machining and its compensation

The consequences due to spindle error motions is dependent on specific applications. For radial error motion, these applications can be classified as applications in a single radially sensitive direction and two radially sensitive directions (Lu and Jamalian 2011). Moreover, for application in a single radial sensitive direction, if the radial direction is fixed in the reference frame, it is called an application with a single fixed radial sensitive direction (e.g. cylindrical surface turning with a lathe), while it is called an application with a single rotating radial sensitive direction (e.g. boring a round hole with a single tool mounted on a spindle rotor) if the radial direction rotates in the reference frame. One typical example for the application in two radially sensitive directions is for the turning of an axis-asymmetric pattern with a fast tool servo, where the spindle radial error motions in both the X and Y directions distort the machined feature.

An et al. studied the relation between the tilt spindle error motion and the surface waviness of a machined workpiece by modeling and experimentation in ultra-precision fly cutting (An et al. 2010). Patterson and Magrab designed the first fast tool servo to compensate for spindle error motion, measured by utilizing capacitance sensors (Patterson and Magrab 1985). Gao et al. measured the angular and axial error motion of the spindle of a diamond turning machine by employing an autocollimator and capacitance probe, respectively (Gao et al. 2007). The measurement results indicated that the spindle angular error motion

contains a periodic component which has a significant contribution to the out-of-flatness of the machined flat surface. Based on the measurements, they adopted a fast tool servo unit to compensate the error motions to reduce the out-of-flatness of a large-area sinusoidal metrology grid. Chen and Yang developed a system to compensate for the spindle error motion, in real time, for a precision lathe by utilizing a piezoelectric actuator (Chen and Yang 1989). Kim and Kim developed a fast tool servo to compensate for the spindle thermal growth error in diamond turning, and a flat surface with sub-micrometer accuracy was obtained (Kim and Kim 2003).

2.4 Surface generation

Montgomery and Altintas proposed a comprehensive dynamic milling model which included the tool geometry and the tool and workpiece vibrations (Montgomery and Altintas 1991). In this model, the cutting forces were determined in five different regions according to the location of the cutting edge. Ehmann and Hong developed a generalized surface generation model, where the cutting tool model and the machine tool kinematic model were integrated (Ehmann and Hong 1994). Altintaş and Lee presented a general model to predict the surface topography, with consideration of the structure dynamics, for helical end mills (Altintaş and Lee 1996). This model can define any helical end mill geometry and calculate the cutting force. The cutting force, chatter vibration, chatter stability lobe and the surface form error can be predicted by this model. Omar et al. developed a model for simulating the surface topography in a side milling process, which took into account the influence of the tool runout, tool deflection, cutting tool tilting, flank face wear and the cutting dynamics(Omar et

al. 2007). During the simulation, the cutting chip thickness and related cutting force are calculated, and then the equations of the system dynamics were solved based on the Runge-Kutta 4th-order method. To take into account the runout, Arizmendi et al. established a surface topography prediction model in ball-end milling (Arizmendi et al. 2008). They derived the equations of the cutting edge trajectories and the cutting tool sweep envelope. Arizmendi et al. also established a model to predict the surface topography in peripheral milling processes, by considering the tool vibration during the machining process (Arizmendi et al. 2009). In their model, the tool vibration was measured and included in the equations of the cutting edge paths. The model is capable of predicting the surface topography, the surface roughness and the form error in the milling process.

Cheng et al. presented a theoretical model to predict the surface roughness in ultra-precision raster milling (Cheng et al. 2008). Based on this model, the cutting conditions and the cutting strategy can be optimized in ultra-precision raster milling. Kong et al. developed an integrated kinematics error model to predict the surface generation for ultra-precision raster milling, where a kinematic machining error model was established for machining error budgets (Kong et al. 2012). Zhang and To presented a surface generation model for raster milling that considered the effect of spindle vibration (Zhang and To 2013b). Wang et al. developed a model to predict the surface roughness in raster milling by taking into account the material elastic recovery, cutting parameters and tool geometry (Wang et al. 2012).

In the micro cutting process, the tool edge radius is comparable to the cutting depth, and the minimum chip thickness and elastic recovery have significant influence on the surface generation. Liu et al. developed a dynamic cutting force and vibration model of micro end milling, where the effect of the minimum chip thickness, built-up-edge, elastic recovery and the elastic-plastic nature in ploughing/rubbing was taken into account (Liu et al. 2004). In this model, the cutting chip thickness was calculated with consideration of the minimum chip thickness and elastic recovery. They then developed surface generation models to predict the sidewall and floor surface for micro end milling (Liu et al. 2007a, 2007b). The models for sidewall and floor surface generation were the deterministic and stochastic. For sidewall surface generation, the deterministic model takes into account the influence of the process kinematics, dynamics, tool edge serration and tool runout, whereas the stochastic model quantifies the ploughing induced stochastic surface roughness. In the floor surface generation model, the deterministic model takes into account the minimum chip thickness, the elastic recovery and the transverse vibration. Guo and Ehmann developed a surface generation model for the elliptical vibration texturing process, in which the effects of the minimum chip thickness and elastic recovery were considered (Guo and Ehmann 2013).

Lin and Chang presented a surface topography simulation model for the turning process to analyze the effect of relative vibration between the cutting tool and workpiece on surface roughness (Lin and Chang 1998). Their results indicated that the vibration frequency ratio is the critical factor affecting the surface profile. In addition, the radial-direction vibration has a more significant effect than the

vibrations in the axial and tangential direction. Cheung and Lee developed a model-based simulation system to predict the surface roughness in ultra-precision diamond turning, where the influence of the tool geometry, process parameters and relative vibration between the workpiece and the cutting tool were taken into account (Cheung and Lee 2000). Based on this simulation system, the optimized cutting conditions can be obtained without conducting trials.

Abouelatta and Madl studied the relation between the surface roughness and the cutting vibration in the turning process (Abouelatta and Madl 2001). They derived mathematical models to predict the surface roughness by considering the cutting parameters and machine tool vibration. Jang et al. developed an on-line roughness measuring approach in hard turning by correlating the surface roughness and the cutting vibrations (Jang et al. 1996).

2.5 Summary

With the development of various ultra-precision machining techniques, these techniques are extensively applied to the fabrication of components with high surface quality and high form accuracy. These components are extensively applied in many fields such as national defense, biomedical implants, astronomy and telecommunications. In ultra-precision machining, the form accuracy and the surface roughness are in the sub-micrometer and nanometer range respectively.

A spindle with excellent performance is critical for many ultraprecision machining techniques, so a number of spindle error motion measuring

approaches has been proposed to evaluate the performance of the spindle. A vital point for spindle error motion measurement is the separation of the spindle error motion and the form error of the artifact, and many studies have been conducted on this. However, little attention has been paid to the effects of the dynamic characteristics of the spindle in the machining process. These effects make significant contributions to the surface form accuracy and the surface roughness in ultra-precision machining.

To predict the surface topography, much research has been conducted to develop various models to simulate the surface profile in machining processes, including turning and milling. Both 2D and 3D models have been developed. Many factors, such as tool geometry, cutting conditions, tool run out, relative vibrations between the cutting tool and the workpiece, tool shaft deflection and cutting dynamics are taken into account in most of these models. Nonetheless, the spindle dynamics combined with the cutting mechanism in micro cutting has not been considered in present models.

In consideration of the aforementioned research gap, it is necessary to investigate the spindle dynamics and the effects on the ultra-precision machining process. In addition, a model for predicting the surface topography in ultra-precision machining needs to be developed by considering the spindle dynamics in the cutting process.

Chapter 3 Modeling of spindle dynamics

3.1 Introduction

The spindle error motions have significant influence on the machining accuracy in the machining process. To evaluate the performance of the spindle before it is used for machining, a number of techniques have been developed to measure the spindle error motion. These measuring procedures are normally conducted during the air cutting process, and this allows the spindle dynamics error in an actual machining process to be neglected.

In this Chapter, the spindle dynamics error motions under the effect of the spindle unbalance are investigated. A spindle dynamics model is established to explore the spindle dynamics characteristics. In addition, a series of cutting experiments are conducted on an ultra-precision lathe to identify the effect of the spindle unbalance induced error motions on the form errors. Eccentric error motion and the spindle vibration under the excitation of spindle unbalance are identified.

3.2 Modeling of the unbalance induced error motions of ABS

The system considered contains a spindle shaft and a chuck for simplicity. The spindle shaft is regarded as a Timoshenko beam while the chuck is regarded as a

rigid disc. The bearings of the spindle system are simplified as linear springs and dampers. A diagram of the aerostatic bearing spindle system with a chuck is shown in Fig. 3.1. The translation in the axial direction and torsional deformation of the spindle shaft are negligible and thus are omitted. O-*XYZ* is a fixed coordinate system, and the *Z*-axis coincides with the centerline of the spindle when the spindle shaft is not deformed. The rotation angles of a plane perpendicular to the spindle shaft centerline are denoted by ϕ_x and ϕ_y, and the translations of this plane in the *x* and *y* directions are denoted by u and v.
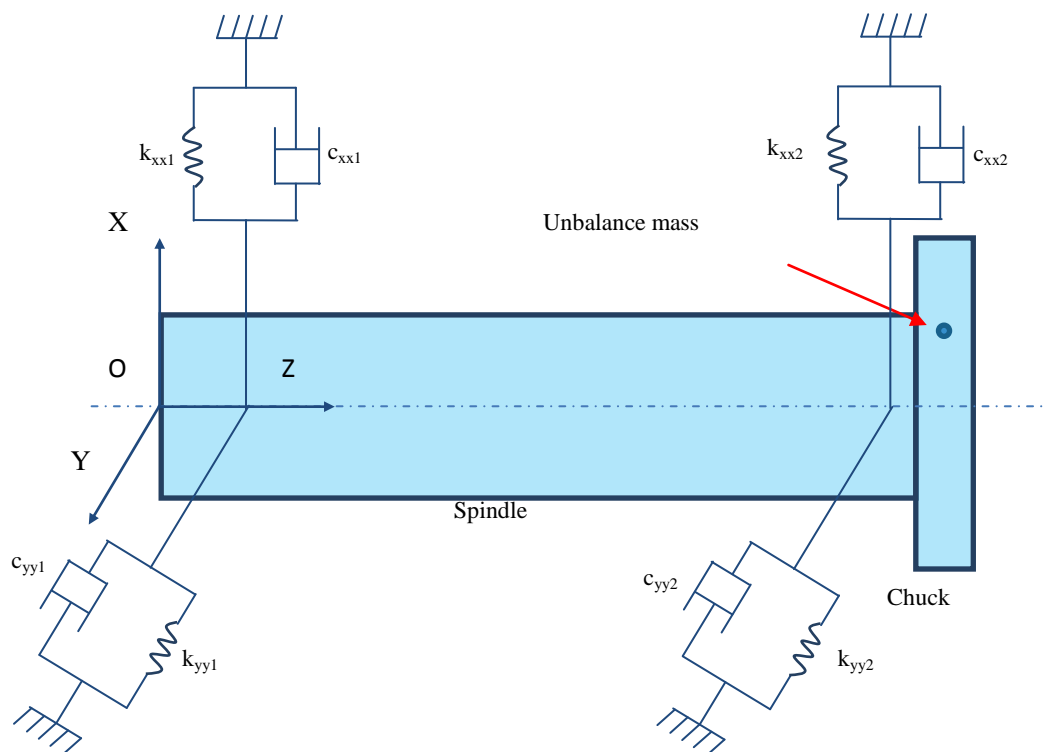

Fig. 3.1 Schematic of spindle system.

3.2.1 Dynamics of ABS

As is mentioned above, the chuck is regarded as a rigid disc. The kinetic energy of the rigid disc can be expressed by:

$$T_d = \frac{1}{2} \begin{Bmatrix} \dot{u}_2 \\ \dot{\phi}_{y2} \end{Bmatrix}^{\mathrm{T}} \begin{bmatrix} m_{\mathrm{Disc}} & 0 \\ 0 & J_d \end{bmatrix} \begin{Bmatrix} \dot{u}_2 \\ \dot{\phi}_{y2} \end{Bmatrix} + \frac{1}{2} \begin{Bmatrix} \dot{v}_2 \\ -\dot{\phi}_{x2} \end{Bmatrix}^{\mathrm{T}} \begin{bmatrix} m_{\mathrm{Disc}} & 0 \\ 0 & J_d \end{bmatrix} \begin{Bmatrix} \dot{v}_2 \\ -\dot{\phi}_{x2} \end{Bmatrix}$$

$$+ \Omega \begin{Bmatrix} \dot{u}_2 \\ \dot{\phi}_{y2} \end{Bmatrix}^{\mathrm{T}} \begin{bmatrix} 0 & 0 \\ 0 & J_p \end{bmatrix} \begin{Bmatrix} v_2 \\ -\dot{\phi}_{x2} \end{Bmatrix} + \frac{1}{2} J_p \Omega^2$$

(3.1)

where J_d is the diametric moment of inertial of rigid disc, J_p is the polar

moment of inertial, m_{Disc} is the mass of the rigid disc and Ω is the spindle speed.

In the present study, the spindle shaft is only considered as containing one

element of Timoshenko beam and two nodes. Node 1 and Node 2 represent the

left and right nodes in Fig. 3.1 respectively. Each node contains two translational

degrees of freedom and two rotational freedoms, so the spindle has totally eight

degrees of freedom. The spindle shaft can be divided into a number of sliced

disks, and each sliced disk is regarded as rigid. The kinetic energy of each sliced

disk can be obtained from:

$$\mathrm{d}T = \frac{1}{2} \rho A \left(\dot{q}_x^T N_1^T N_1 \dot{q}_x + \dot{q}_y^T N_1^T N_1 \dot{q}_y \right) \mathrm{d}z + \frac{1}{2} \rho I_y \left(\dot{q}_x^T N_2^T N_2 \dot{q}_x + \dot{q}_y^T N_2^T N_2 \dot{q}_y \right)$$

$$+ \rho I_y \left(\Omega^2 - 2\Omega \dot{q}_y^T N_2^T N_2 q_x \right) \mathrm{d}z$$

(3.2)

where q_x and q_y are the coordinates of the spindle shaft, $q_x = \begin{bmatrix} u_1 \\ \phi_{y1} \\ u_2 \\ \phi_{y2} \end{bmatrix}$, $q_y = \begin{bmatrix} v_1 \\ -\phi_{x1} \\ v_2 \\ -\phi_{x2} \end{bmatrix}$,

N_1 and N_2 are the shape functions of Timoshenko beam.

The incremental potential energy of a sliced disk is:

$$dU = \frac{1}{2} EI_y \left[\left(\frac{d\phi_y}{dz} \right)^2 + \left(\frac{d\phi_x}{dz} \right)^2 \right] dz + \frac{1}{2} \frac{GA}{\chi} \left(\gamma_{xz}^2 + \gamma_{yz}^2 \right) dz \tag{3.3}$$

where $\gamma_{xz} = \phi_y - \dfrac{du}{dz}$, $\gamma_{yz} = -\phi_y - \dfrac{dv}{dz}$, χ is the shear factor.

The kinetic energy and potential energy of the spindle shaft can be obtained by integrating all the sliced disks.

The thrust aerostatic bearing is simplified with linear stiffness and damping, so the reaction forces from the two bearing at the ends of spindle can be obtained:

$$\begin{bmatrix} F_{bx1} \\ F_{by1} \end{bmatrix} = - \begin{bmatrix} c_{xx1} & c_{xy1} \\ c_{yx1} & c_{yy1} \end{bmatrix} \begin{bmatrix} \dot{u}_1 \\ \dot{v}_1 \end{bmatrix} - \begin{bmatrix} k_{xx1} & k_{xy1} \\ k_{yx1} & k_{yy1} \end{bmatrix} \begin{bmatrix} u_1 \\ v_1 \end{bmatrix} \tag{3.4}$$

$$\begin{bmatrix} F_{bx2} \\ F_{by2} \end{bmatrix} = - \begin{bmatrix} c_{xx2} & c_{xy2} \\ c_{yx2} & c_{yy2} \end{bmatrix} \begin{bmatrix} \dot{u}_2 \\ \dot{v}_2 \end{bmatrix} - \begin{bmatrix} k_{xx2} & k_{xy2} \\ k_{yx2} & k_{yy2} \end{bmatrix} \begin{bmatrix} u_2 \\ v_2 \end{bmatrix} \tag{3.5}$$

The motion equation of the spindle system can be obtained based on Lagrange's principle:

$$\begin{bmatrix} M_1 & 0 \\ 0 & M_1 \end{bmatrix} \begin{bmatrix} \ddot{Q}_x \\ \ddot{Q}_y \end{bmatrix} + \begin{bmatrix} c_{11} & c_{12} + G_1 \\ c_{21} - G_1 & c_{22} \end{bmatrix} \begin{bmatrix} \dot{Q}_x \\ \dot{Q}_y \end{bmatrix} + \begin{bmatrix} k_{11} + K_1 & k_{12} \\ k_{21} & k_{22} + K_1 \end{bmatrix} \cdot \begin{bmatrix} Q_x \\ Q_y \end{bmatrix} = \begin{bmatrix} F_x \\ F_y \end{bmatrix}$$

$$\tag{3.6}$$

where M_1, G_1, and K_1 are the mass matrix, gyroscopic matrix and stiffness matrix of the spindle system respectively, and Q_x and Q_y are the coordinates of the nodes of the system.

3.2.2 The unbalance induced error motions

In ultra-precision machining, the spindle is usually balanced to get a good performance. However, due to the installation of the chuck and the workpiece, an

unbalance mass will be generated. In this model, the unbalance mass is regarded

as concentrated in the rigid disc, as shown in Fig. 3.1. C-$\xi\eta\zeta$ is a coordinate

system fixed on the rigid disc, as shown in Fig. 3.2, where the origin of the

coordinate coincides with the center point of rigid disc and the ζ-axis coincides

with the centerline of the spindle. The coordinates of the unbalance mass in the

coordinate of C-$\xi\eta\zeta$ are $\left(e_{\xi},\ e_{\eta},\ e_{\zeta} \right)$. Thus the generalized unbalance forces in

the directions X and Y are:

$$F_{ex} = m_{p}\Omega^{2}\left(\begin{bmatrix} e_{\xi} \\ 0 \end{bmatrix}\cos\Omega t + \begin{bmatrix} -e_{\eta} \\ 0 \end{bmatrix}\sin\Omega t \right) \tag{3.7}$$

$$F_{ey} = m_{p}\Omega^{2}\left(\begin{bmatrix} e_{\eta} \\ 0 \end{bmatrix}\cos\Omega t + \begin{bmatrix} e_{\xi} \\ 0 \end{bmatrix}\sin\Omega t \right) \tag{3.8}$$

The steady solution under unbalance force is assumed as follows:

$$\begin{cases} Q_{x} = \{A_{1}\}\cos\Omega t - \{B_{1}\}\sin\Omega t \\ Q_{y} = \{A_{2}\}\cos\Omega t + \{B_{2}\}\sin\Omega t \end{cases} \tag{3.9}$$

By substituting Eq. 3.9 into the equation of motion and comparing the

coefficients of $\cos\Omega t$ and $\sin\Omega t$ on the two sides of the equation, one can get

the following equation:

$$\begin{bmatrix} k_{11}+K_{1}-M_{1}\Omega^{2} & -c_{11}\Omega & \left(c_{12}+G_{1}\right)\Omega & k_{12} \\ c_{11}\Omega & k_{11}+K_{1}-M_{1}\Omega^{2} & -k_{12} & \left(c_{12}+G_{1}\right)\Omega \\ -\left(c_{12}-G_{1}\right)\Omega & -k_{21} & k_{22}+K_{1}-M_{1}\Omega^{2} & -c_{22}\Omega \\ k_{21} & -\left(c_{12}-G_{1}\right)\Omega & c_{22}\Omega & k_{22}+K_{1}-M_{1}\Omega^{2} \end{bmatrix}\begin{bmatrix} A_{1} \\ B_{1} \\ B_{2} \\ A_{2} \end{bmatrix} = \Omega^{2}\begin{bmatrix} F_{1c} \\ F_{2c} \\ F_{1c} \\ F_{2c} \end{bmatrix}$$

$$\tag{3.10}$$

where

$$F_{1c} = \begin{bmatrix} 0 \\ 0 \\ m_{\text{Disc}}e_{\xi} \\ 0 \end{bmatrix}, \quad F_{2c} = \begin{bmatrix} 0 \\ 0 \\ m_{\text{Disc}}e_{\eta} \\ 0 \end{bmatrix}$$
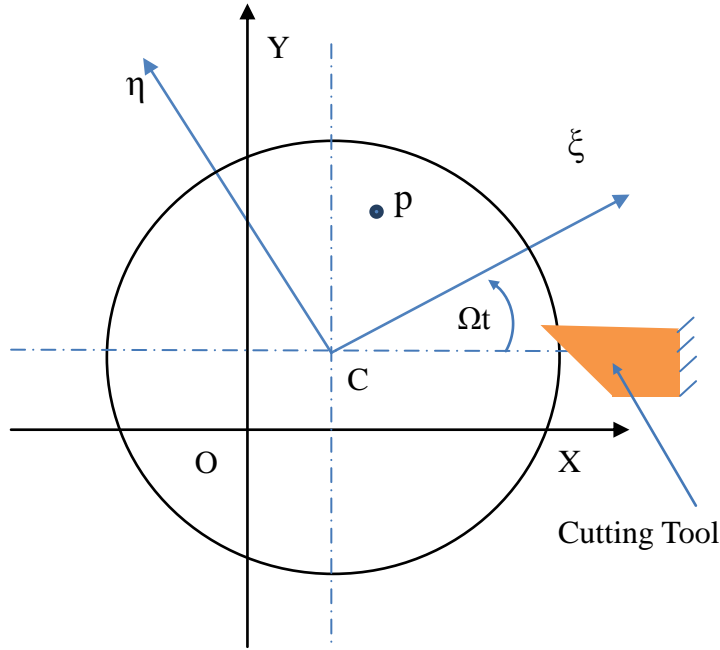
Fig. 3.2 Relation between the inertial and the fixed coordinates.

In the present study, only the stiffness and damping of the aerostatic bearing in the x and y directions are considered. Moreover, the stiffness and damping in one direction are equal to the stiffness and damping in another direction.

The trajectory of the geometric center of the spindle at a node in inertial coordinates can be obtained from:

$$\begin{cases} x_c = a_x \cos \Omega t - b_x \sin \Omega t \\ y_c = a_y \cos \Omega t + b_y \sin \Omega t \end{cases} \tag{3.11}$$

where a_x, b_x, a_y and b_y are coefficients related to a specific node and can be obtained from the solution of Eq. 3.10.

The eccentric error motion of the spindle makes the center of the trajectory of the tool tip in the fixed coordinate of workpiece change with different spindle speeds.

The trajectory of the tool tip can be obtained from Eq. 3.12:

$$\begin{cases} \xi_t = (x_t - x_c)\cos\Omega t + (y_t - y_c)\sin\Omega t \\ \eta_t = (y_t - y_c)\cos\Omega t - (x_t - x_c)\sin\Omega t \end{cases} \qquad (3.12)$$

where x_t and y_t are coordinates of the tool tip shown in Fig. 3.2 in inertial coordinates.

In the cutting process, the spindle may not always remain stable and may vibrate due to the excitation. The unstable transient response of the spindle system with constant cutting force and unbalance excitation is solved, based on the Newmark method. The Newmark method is based on the dynamics equation of the system at time of $t + \Delta t$:

$$M\ddot{Q}_{t+\Delta t} + C\dot{Q}_{t+\Delta t} + KQ_{t+\Delta t} = F_{t+\Delta t} \qquad (3.13)$$

The displacement, velocity and acceleration of the dynamics system yield:

$$\begin{aligned} Q_{t+\Delta t} &= \frac{F_{t+\Delta t}}{\hat{K}} + \frac{M}{\hat{K}}\left[\frac{1}{\alpha\Delta t^2}Q_t + \frac{1}{\alpha\Delta t}\dot{Q}_t + \left(\frac{1}{2\alpha}-1\right)\ddot{Q}_t\right] \\ &+ \frac{C}{\hat{K}}\left[\frac{\beta}{\alpha\Delta t}Q_t + \left(\frac{\beta}{\alpha}-1\right)\dot{Q}_t + \left(\frac{\beta}{2\alpha}-1\right)\Delta t\ddot{Q}_t\right] \end{aligned} \qquad (3.14)$$

$$\dot{Q}_{t+\Delta t} = \dot{Q}_t + \left[(1-\beta)\ddot{Q}_t + \beta\cdot\ddot{Q}_{t+\Delta t}\right]\Delta t \qquad (3.15)$$

$$\ddot{Q}_{t+\Delta t} = \frac{1}{\alpha\Delta t^2}(Q_{t+\Delta t} - Q_t) - \frac{1}{\alpha\Delta t}\dot{Q}_t - \left(\frac{1}{2\alpha}-1\right)\ddot{Q}_t \qquad (3.16)$$

where

$$\hat{K} = K + \frac{1}{\alpha\Delta t^2}M + \frac{\beta}{\alpha\Delta t}C$$

3.3 Simulation of unbalance induced error motion

To analyze the dynamics of the spindle system, simulations are conducted based on the established theoretical model. A Matlab programme based on the model has been written for the simulation. Details of the parameters for simulation are presented in Table 3.1.

Table 3.1 Parameters used for simulation

Damping c_{ij}	250 N.s/m
Radial stiffness k_{ij}	22 N/μm
Shear factor χ	1.11
Spindle mass density $\rho_{spindle}$	7650 kg/m^3
Disk mass density ρ_{disk}	2710 kg/m^3
Elasticity modulus E	200*10^9 Pa
Poisson's ratio ν	0.27
Spindle length $l_{spindle}$	264.9 mm
Spindle diameter $d_{spindle}$	89 mm
Disk thickness t_{disk}	47.3 mm
Disk diameter d_{disk}	203.2 mm
Eccentric distance e_{ξ}	0.5μm

3.3.1 The unbalance induced eccentricity

The simulation is only conducted for Node 2 which represents the cutting point at the workpiece. The displacement of Node 2 in a steady condition with the effect of unbalance mass at spindle speed of 500 rad/s is shown in Fig. 3.3. As

can be seen from Fig. 3.3, the translational displacements in the x and y axis directions at Node 2 are harmonic waves and they have 90° of phase shift but the same amplitude. This means that the center line of the spindle at Node 2 has an eccentric motion with a circular orbit.
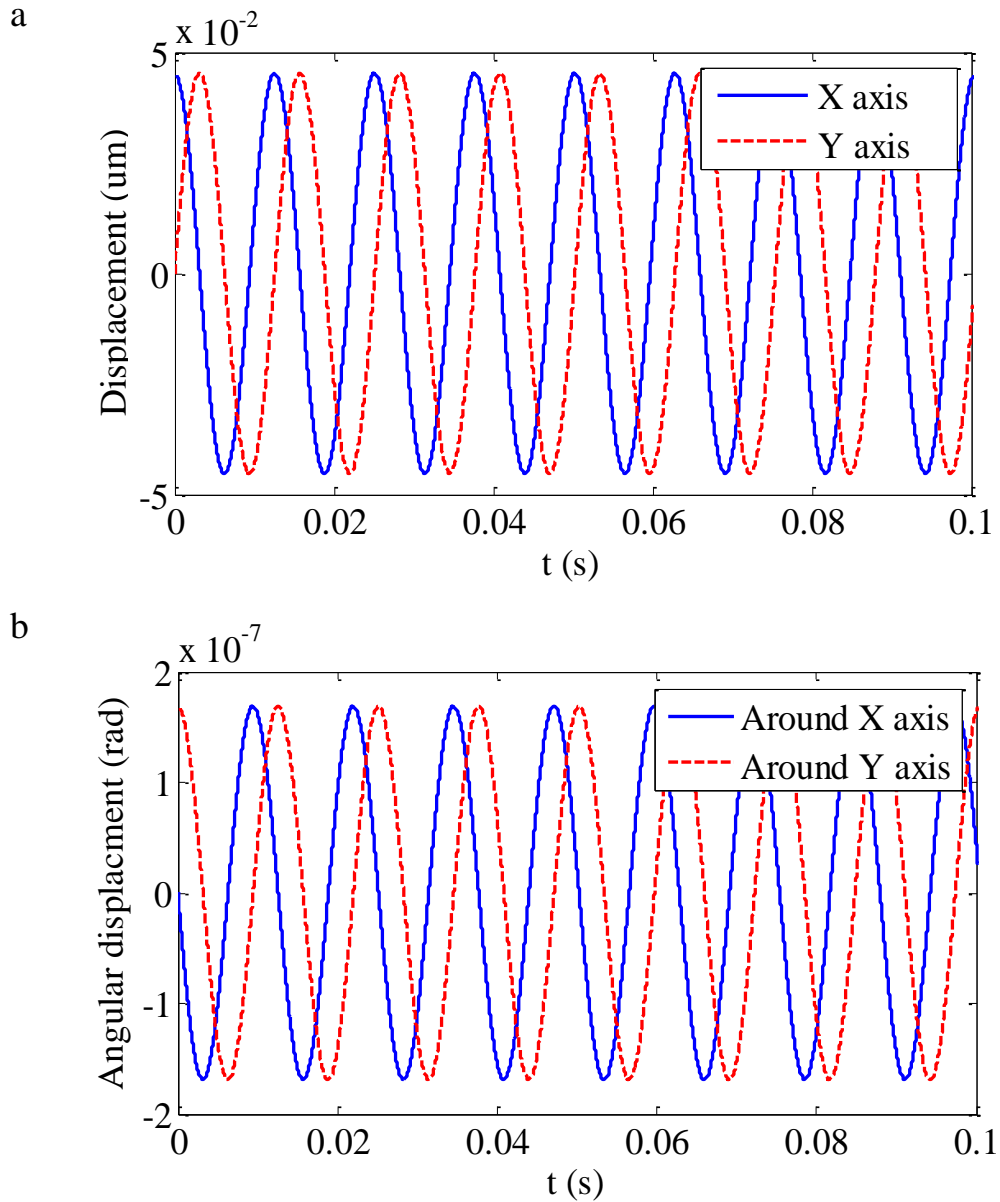
Fig. 3.3 The eccentric motion of spindle at the spindle speed of 500 rad/s: (a) displacement, (b) angular displacement.

The eccentricity error motion of the spindle has influence on the actual trajectory of the tool tip on the workpiece. In this simulation, a simple circular trajectory is

used. The simulated trajectories of the tool tip in coordinates fixed on the workpiece at different spindle speeds are illustrated in Fig. 3.4. As shown in Fig. 3.4, the center of the tool trajectory changes at different spindle speeds while the diameter of the trajectory remains unchanged.
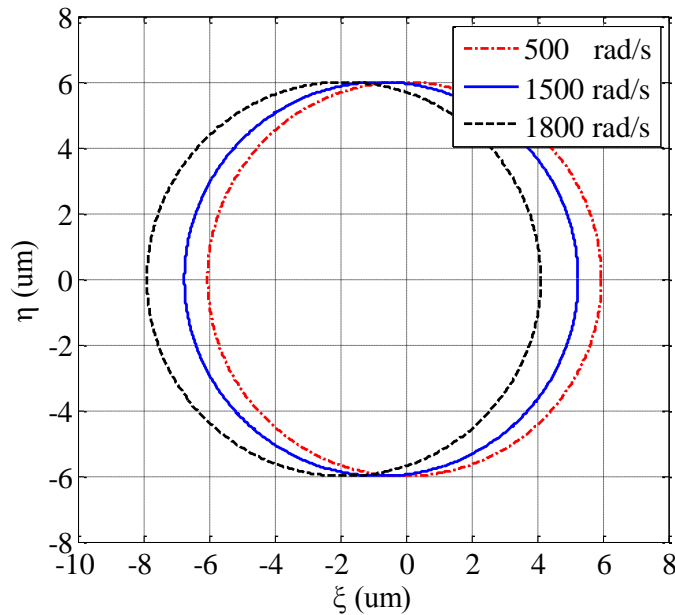
Fig. 3.4 Simulated trajectory of the tool tip in the coordinate fixed on workpiece.

3.3.2 The double-frequency vibration with excitation

The transient response of the translational displacement at Node 2 is simulated as shown in Fig. 3.5, where the displacements in both the *x* and *y* directions fluctuate with time, and the amplitude of displacement is modulated with a relative low frequency envelope. The attenuation of the amplitude of the low frequency envelope depends on the damping of the spindle. Moreover, the enlarged detail in Fig. 3.5 indicates that the fluctuation is the superposition of the low and high frequency components. To make this clear, the simulated data is

analyzed with FFT as shown in Fig. 3.6. The FFT analysis reveals that the vibration of the displacement in the both *x* and *y* directions contains one low frequency and two high frequency components under excitation. The low frequency component is derived from the unbalance induced eccentric error motion. The two high frequencies are related to the first forward and backward whirl modes of the rotating spindle, resulting from the gyroscopic effect which increases the stiffness of the forward mode and simultaneously decrease the stiffness of the backward mode (Bediz et al. 2014 , Filiz et al. 2011, Hosseini et al. 2014).
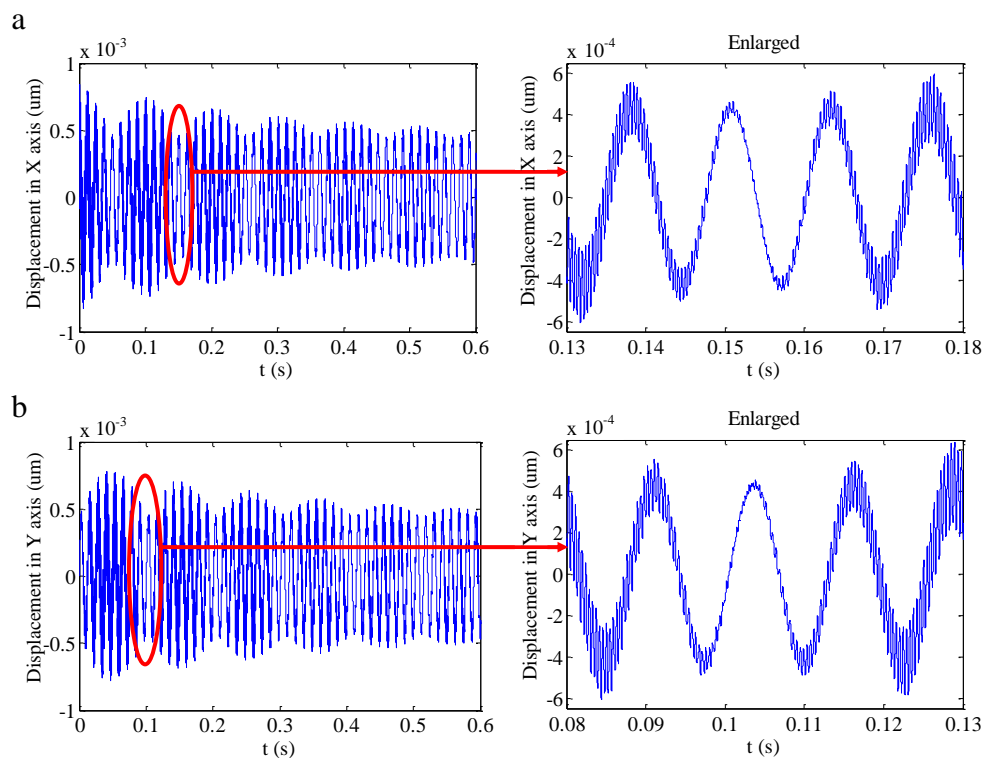
Fig. 3.5 Dynamic transient response at spindle speed of 500 rad/s, cutting force 0.03 N, thrust force 0.05 N: (a) displacement in X axis, (b) displacement in Y axis.
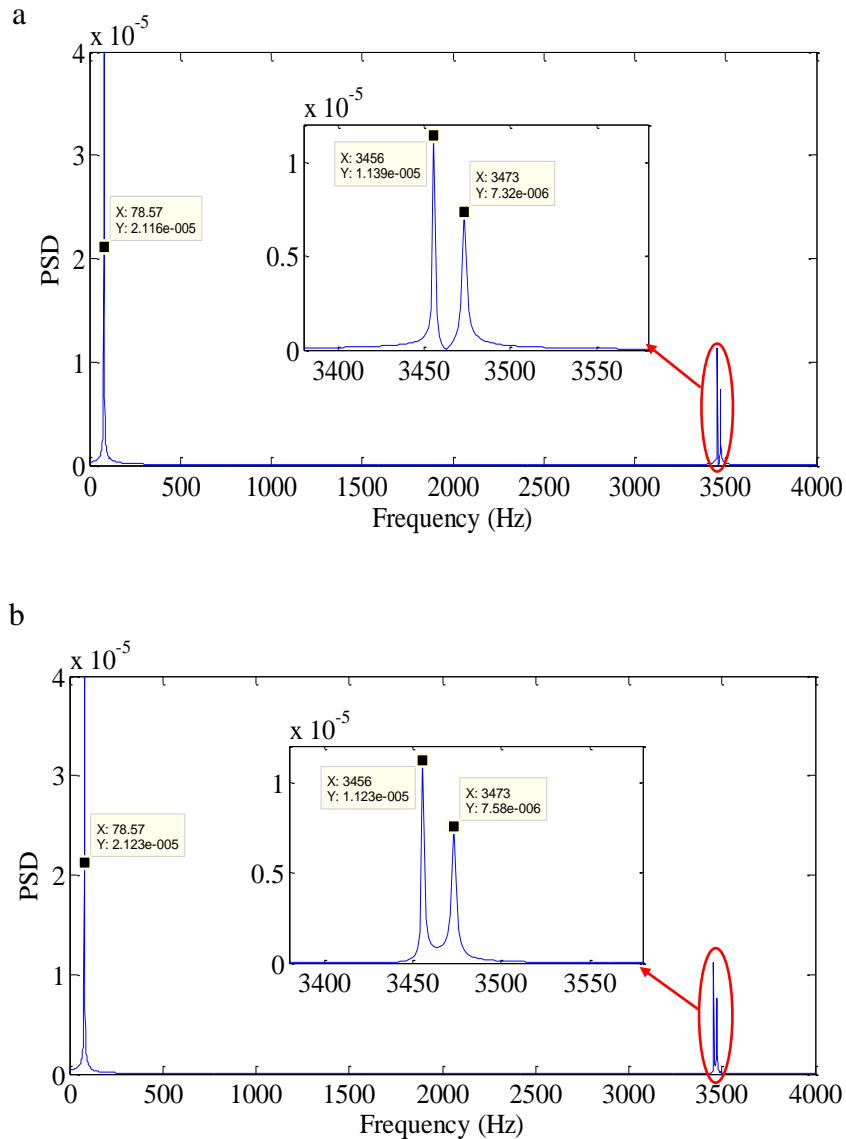
Fig. 3.6 FFT of spindle transient response with excitation: (a) in x direction, (b) in y direction.

3.4 Experimental design and setup

To practically identify the error motions, two experiments were designed. The first experiment was spiral groove cutting which was conducted to investigate the form error measured along the circumference caused by the eccentricity error motion and the form error measured along axial direction of workpiece caused by the double frequency vibration of the spindle. To make the enveloping

phenomenon due to double frequency vibration more clear, a single groove cutting experiment was also carried out to measure the fluctuation of the cutting force.
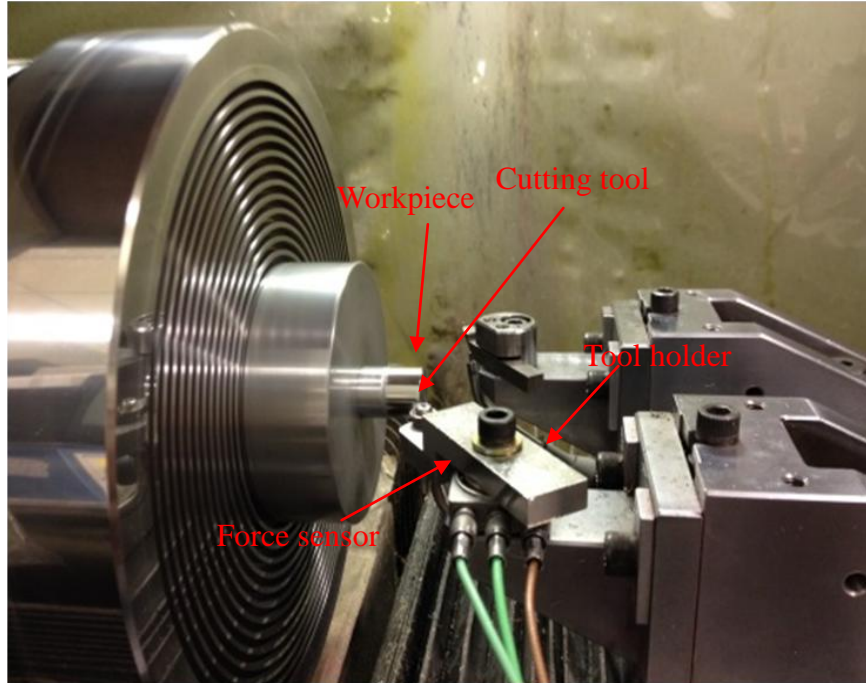
Fig. 3.7 Experimental setup

All experiments were conducted on an ultra-precision machining system (Nanoform 200 from Precitech from USA) (refer to Appendix Ⅳ). A diamond tool with nose radius of 0.24 mm, rake angle of 0° and clearance angle of 10° was used. A force sensor (Kistler 9252A) was mounted between the tool and the tool holder to measure the cutting force. Two aluminum alloy 6061 cylindrical workpieces of diameter 15 mm and length 15 mm were prepared for two groove cutting experiments respectively. The experimental setup is shown in Fig. 3.7.

3.4.1 Spiral groove cutting

The cutting conditions are shown in Table 3.2. A mirror cylindrical surface was

firstly machined and then two groups (named Group 1 and Group 2) were machined on the mirror cylindrical surface group by group. These two groups were located at different positions of the mirror cylindrical surfaces, as shown in Fig. 3.8. Each group contained three spiral grooves machined at three different spindle speeds. The air shower and coolant were used in all the machining process.

Table 3.2 Cutting conditions for spiral groove cutting

Cylindrical mirror surface	Spindle speed	1600 rpm
	Depth of cut	2 μm
	Feed rate	5 μm/rev
Spiral groove	Spindle speed	600 rpm, 1600 rpm and 2600 rpm
	Depth of groove	2 μm
	Pitch of groove	70 μm
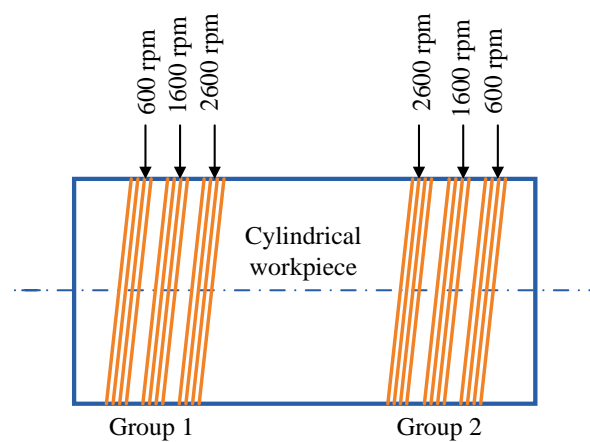
Fig. 3.8 Location of machined grooves on the workpiece

A Talysurf PGI 1240 was employed to measure the machined spiral grooves (refer to Appendix I). As shown in Fig. 3.9a, the stylus moved along the axial direction of the workpiece to measure all the grooves. In order to identify the eccentricity induced form error, the measuring process was repeated by rotating the workpiece with a constant increment of 15° as shown in Fig. 3.9b.

a

Stylus

Cylindrical surface

Spiral groove

b

Depth of groove

Circumferential direction

Cylindrical surface
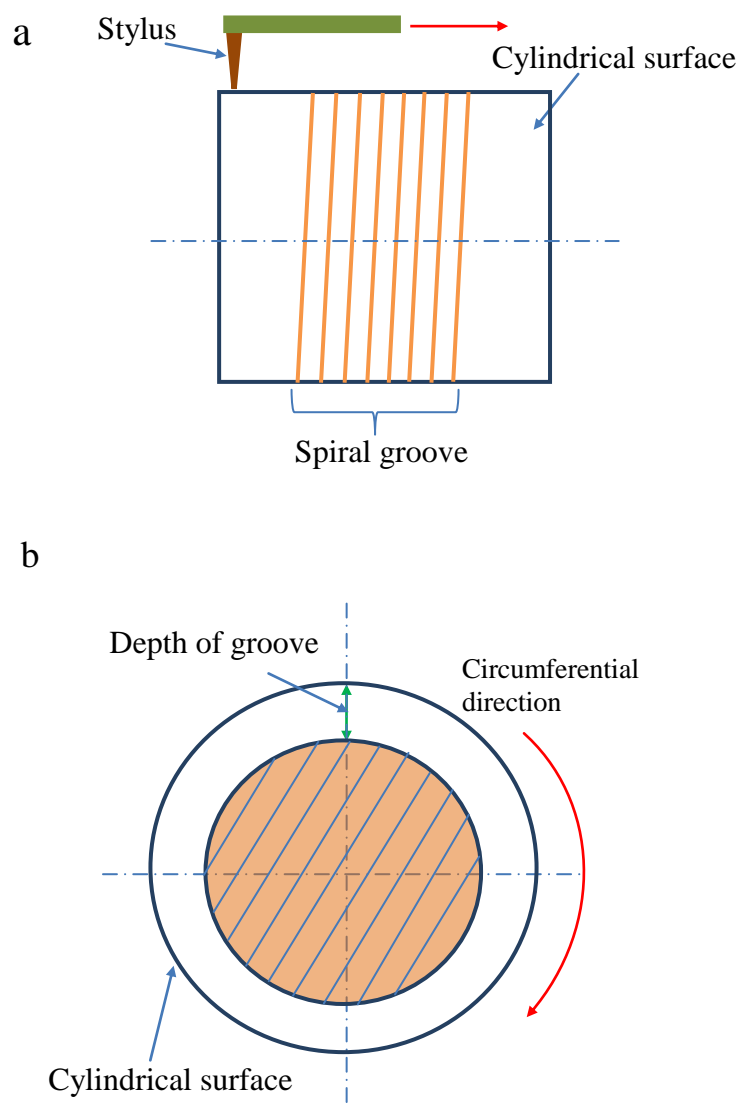
Fig. 3.9 Schematic of the measurement of spiral groove: (a) along axial direction, (b) along circumferential direction.

3.4.2 Single groove cutting

The cutting conditions are shown in Table 3.3. A mirror cylindrical surface was firstly machined. Two single grooves (named Groove 1 and Groove 2) were machined at different positions of the workpiece. The machining of each groove was divided into the cutting process and the rubbing process. During the cutting process, the tool moved along the radial direction of the spindle at a feed rate of 1 mm/min to cut the workpiece. When the tool had arrived at the given depth of groove, it stopped there for two seconds and the tool rubbed the machined surface of groove. The cutting force of all these two processes was recorded for analysis.

Table 3.3 Cutting conditions for single groove cutting

Cylindrical mirror surface	Spindle speed	2000 rpm
	Depth of cut	2 μm
	Feed rate	5 μm/rev
Spiral groove	Spindle speed	2000 rpm
	Depth of groove	3 μm
	Feed rate in axial direction	1 mm/min

3.5 Experimental results and discussion

3.5.1 The eccentricity of machined groove

For each machined spiral groove, it was measured in both the axial and circumferential directions as shown in Fig. 3.9. There were 14 measured points of depth in the axial direction at a given circumferential position of the spiral groove. Since the measurement increment along the circumferential direction was 15°, there were 24 sets of data point for each spiral groove. Each data set contains 14 measured data points, and the mean value of each set was used to represent the depth of groove at its related circumferential position. The variation of depth of groove along circumferential direction is plotted in Fig. 3.10. The black, red and blue curves are the fitting curves of the measured points along the circumferential direction for the spiral grooves machined at 600 rpm, 1600 rpm and 2600 rpm respectively.

a

b
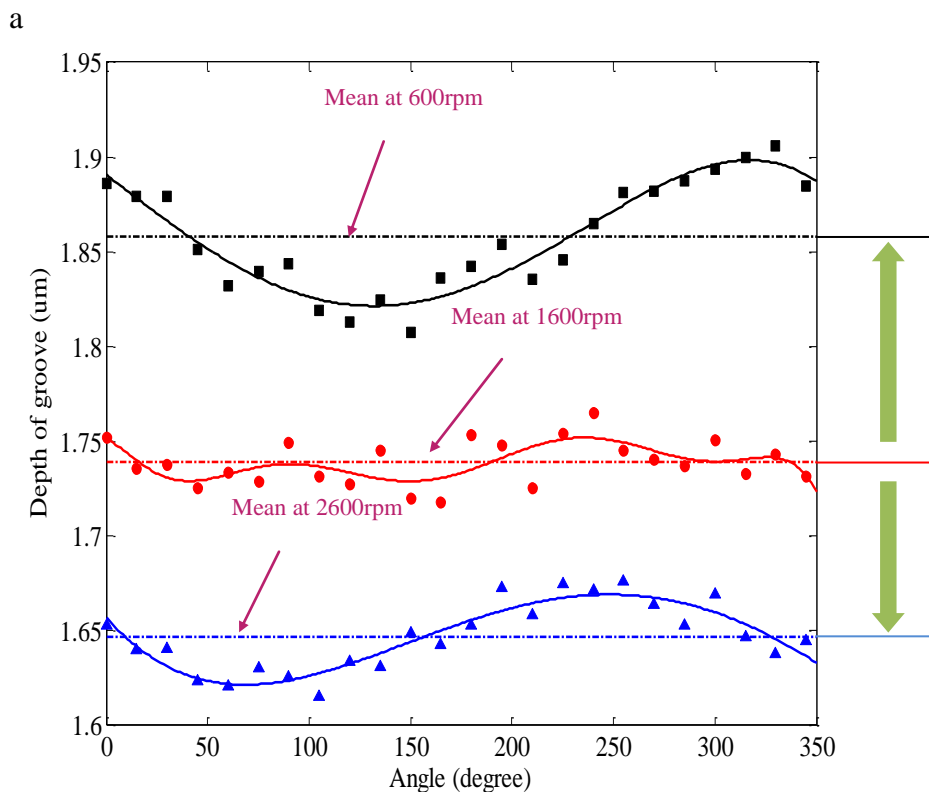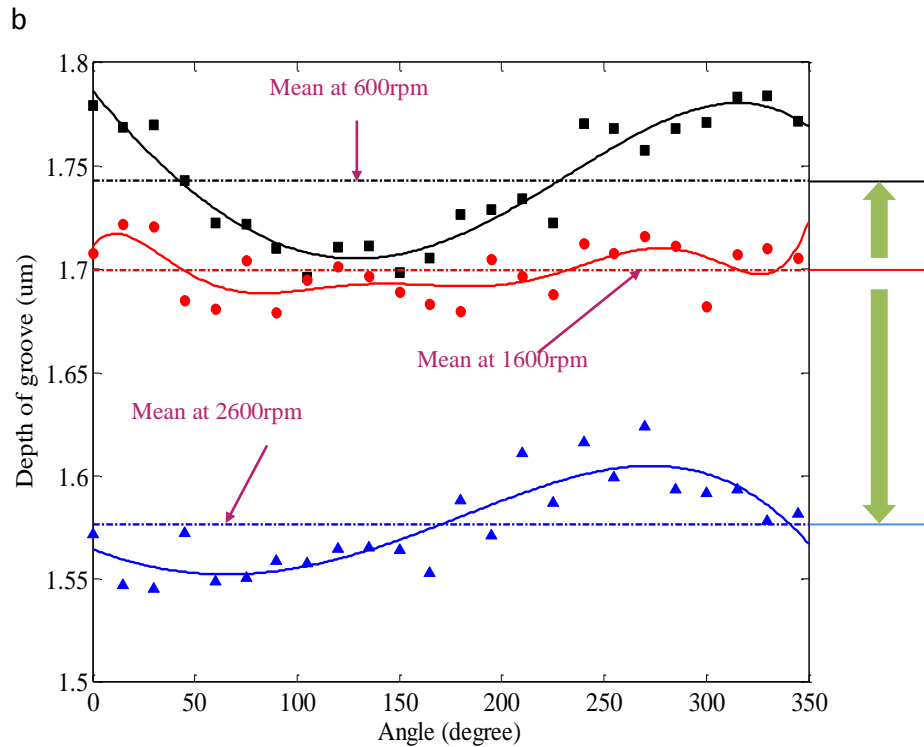
Fig. 3.10 Fluctuation of the depth of machined groove along circumferential direction: (a) Group1, (b) Group 2.

In both Group 1 and Group 2, the fitting curves of the measured points of the depth of grooves along the circumferential direction at spindle speeds of 600 rpm and 2600 rpm are harmonic curves, while the fitting curves at the spindle speed of 1600 rpm in Group 1 and Group 2 have no significant features. The harmonic variation of the depth of groove along the circumferential direction indicates that the center of the actual tool path shifts away from the ideal tool path which is concentric with the machined cylindrical surface, as shown in Fig. 3.11. The shift of the center makes the actual depth of groove fluctuate along the circumferential direction by a harmonic function, and the harmonic frequency is once per revolution. The fluctuation of the depth of the groove machined at a spindle speed of 1600 rpm has no harmonic feature with the once per revolution

frequency as the cylindrical surface is machined at the same spindle speed, which makes the tool path for groove machining concentric with the cylindrical surface. The harmonic fluctuation of depth of grooves machined at the spindle speed of 600 rpm with rotational angle has a phase shift from the harmonic fluctuation at 2600 rpm, as their tool paths have different centers. The results indicate that eccentricity error motion exists in ultra-precision ABS and it makes the machined grooves eccentric when different spindle speeds are used. This shows good agreement with the simulation results shown in Fig. 3.4.
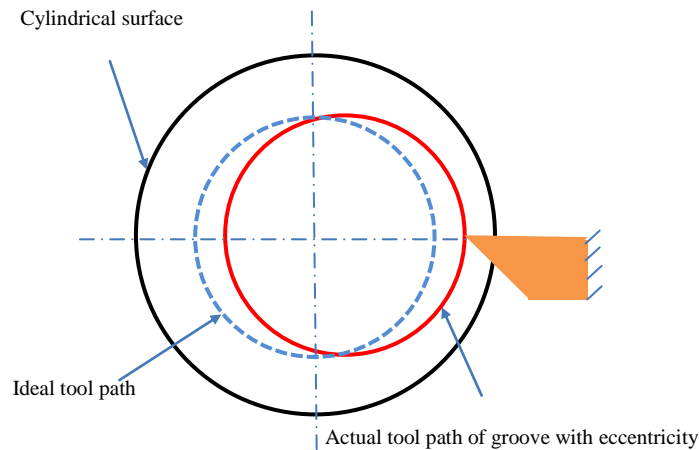
Fig. 3.11 Illustration of shift of the tool path due to eccentric motion of spindle.

3.5.2 Relative distance between the spindle axis and the too-tip

The mean values of the 24 data points of the depth of each groove in Fig. 3.10 are also plotted. As can be seen from Fig. 3.10, the mean values are 1.858μm, 1.739 μm and 1.647 μm in Group 1 while the mean values are 1.743 μm, 1.699 μm and 1.577μm in Group 2 at 600 rpm, 1600 rpm and 2600 rpm respectively. The mean values at the spindle speed of 600 rpm are larger than at 1600 rpm while the mean values at 2600 rpm are smaller than at 1600 rpm both in Group 1

and Group 2. The variation of the mean value indicates that the diameter of the tool path for groove cutting has changed. However, this change cannot be attributed to the unbalance induced eccentric error motion as it is a once per revolution error component of the spindle error motion, which will not affect the diameter of the cylindrical part in turning (Devitt 2009). The variation of the relative distance between the spindle axis and the tool tip is the reason for the change of mean values at different spindle speeds.

The air shower and coolant are used in the machining process and the cutting process is completed within 5 minutes after warming up, so the effect of thermal error on the change of relative distance can be neglected. Moreover, the spiral grooves are machined in several stages along different lengths of the cylindrical workpiece, revealing that the effect of spindle speed on the depth of cut at different speeds is repeatable. An explanation for the result is that the equilibrium position of the spindle axis changes with different spindle speeds due to the hydrodynamic effect of the aerostatic bearing (Yang et al. 2004, Lv et al. 2004), and this will be discussed in Chapter 4

3.5.3 Low frequency enveloping of the vibrations

The cutting force in a single groove cutting process is measured by a force sensor (Kistler 9252A). The thrust force is filtered with a low pass wavelet filter and the filtered thrust force is plotted in Fig. 3.12. As can be seen from Fig. 3.12, the thrust force can be divided into the cutting and rubbing stages. During the cutting stage, the thrust force increase with time. During the rubbing stage, the thrust

force fluctuates with a period of t_1, which is equal to the period of the spindle speed. In addition, the thrust force is also enveloped by waviness of a larger period, which is several times larger than t_1, as illustrated with an enveloping curve in the enlarged detail in Fig. 3.12. This differs with the ideal case in which the thrust force is equal to zero. The FFT results of the measured thrust cutting forces are illustrated in Fig. 3.13. It indicates a frequency pair in the cutting process, qualitatively showing good agreement with the FFTs obtained from the simulated results as shown in Fig. 3.6.
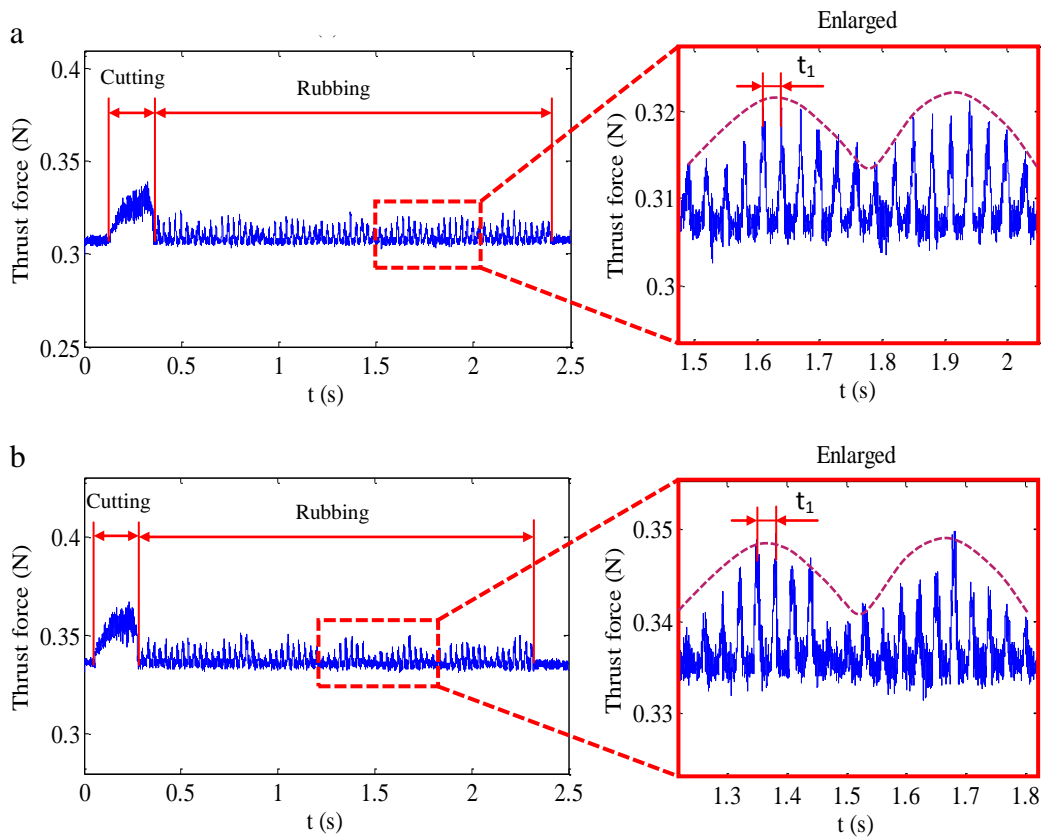
Fig. 3.12 Measured thrust forces in single groove cutting with feed rate of 1mm/min and spindle speed of 2000 rpm: (a) Groove1, (b) Groove 2.
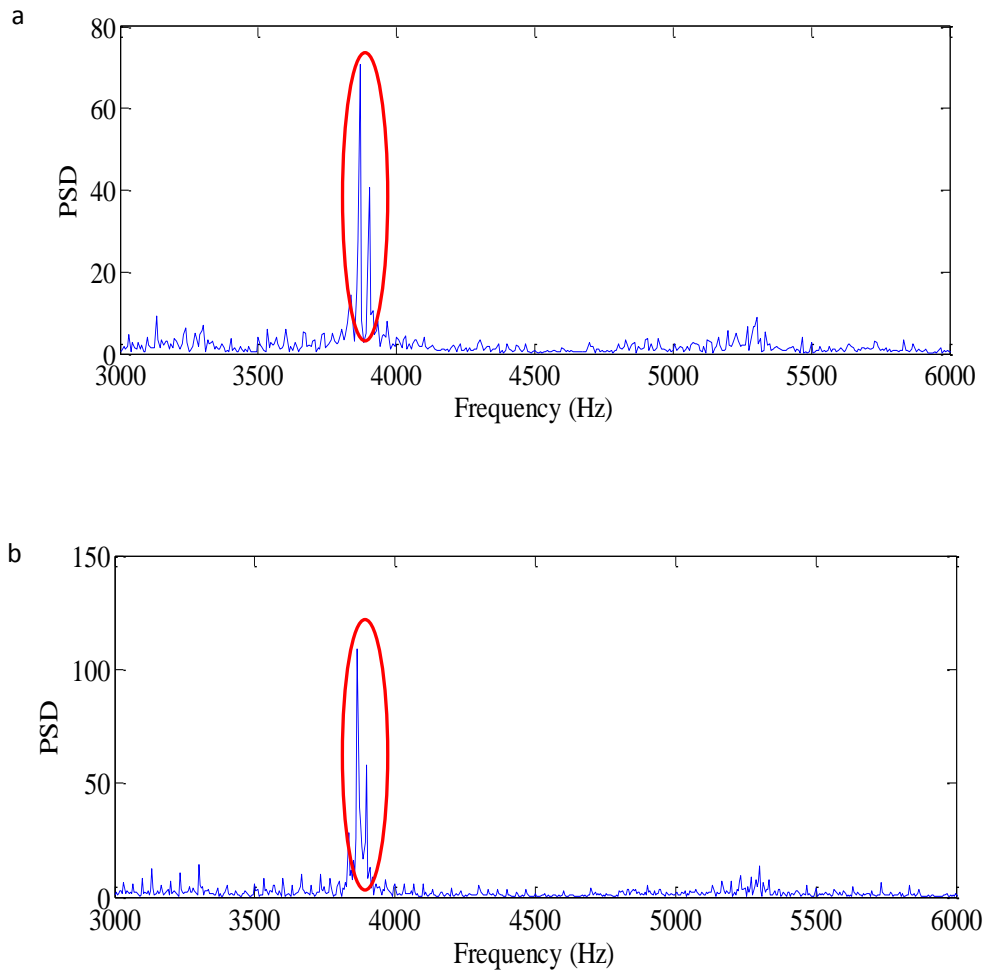
Fig. 3.13 FFT of the measured thrust forces in single groove cutting: (a) Groove1,
(b) Groove 2

Two spiral grooves machined at a spindle speed of 2600 rpm were measured
along the axial direction, at a given circumferential position, with Talysurf PGI
1240 and the measurement results are plotted in Fig. 3.14. There are 14
measurement data points with a uniform pitch along the axial direction for each
groove, and the pitch of two neighboring points relates to one revolution of the
spindle. The measurement data points are fitted with a red curve, as shown in Fig.
3.14. As can be seen from Fig. 3.14, the depth of the spiral groove fluctuates with

a low frequency along the axial direction. This is similar to the enveloping of the fluctuation of the thrust force during the rubbing process, as shown in Fig. 3.12. The experimental results shown in Fig. 3.12 and Fig. 3.14 indicate that the spindle error motion is enveloped with a low frequency component. This is attributed to the double-frequency vibration of the ABS with excitation, as shown in Fig. 3.5 and Fig. 3.6.

In air cutting, if the spindle rotates without any excitation, the spindle will operates in a steady status. Then, the spindle just has eccentricity error motion resulting from the spindle unbalance as shown in Fig. 3.3 and Fig. 3.10. In an actual cutting process, the spindle mass unbalance and the fluctuated cutting force will excite the spindle, forcing the spindle to vibrate. The radial vibration due to the forward and backward modes of the rotating spindle will derive the unique enveloping phenomenon as illustrated in Fig. 3.5 and Fig. 3.12, and it can affect the machining accuracy, as shown in Fig. 3.14.

a

b
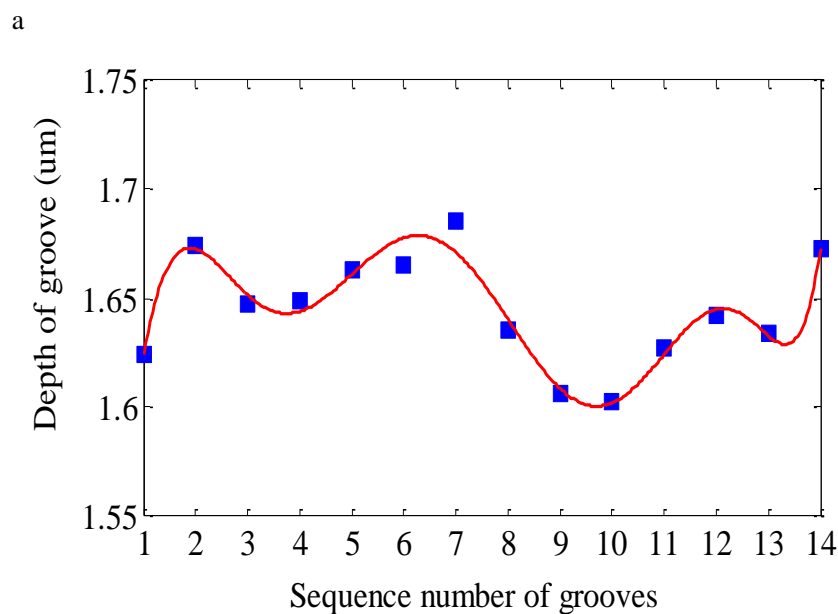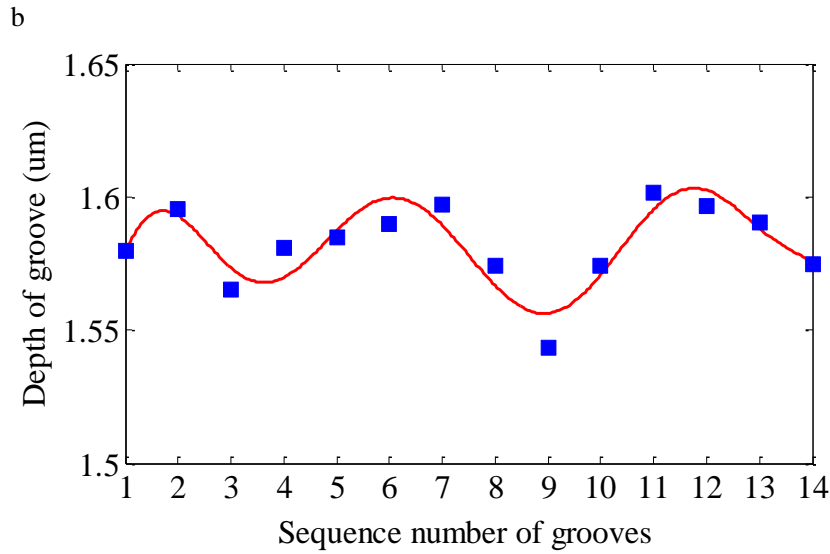
Fig. 3.14 Measured depth of spiral groove along axial direction machined at 2600 rpm: (a) in Group 1 of machined spiral grooves, (b) in Group 2 of machined spiral grooves.

3.6 Summary

In this chapter, the unbalance induced spindle error motion of aerostatic bearing spindle (ABS) and its effect on machining accuracy in ultra precision machining is studied by means of modeling as well as experimental investigations. The specific conclusions are as follow:

(1) The theoretical model reveals that a rotating spindle has double frequency vibration in the radial direction, under excitations such as unbalance mass. The double frequencies are identified from the FFTs of the simulated data and the measured thrust force. These two frequencies are related to the gyroscopic effect induced forward and backward whirl mode.

56

(2) From the groove cutting, the depth of the machined spiral grooves fluctuates along the axial direction with a relatively longer period than the rotating period of the ABS. It is induced from the low frequency enveloping phenomenon causing by the double high frequency vibration of the spindle.

(3) The spindle eccentricity error motion has a significant effect on machining accuracy in ultra precision diamond turning, and it has been identified from the proposed experiments. The eccentricity error motion is induced by the unbalance mass of the spindle system, and its amplitude changes with different spindle speeds. On the other hand, the diameter of the tool trajectory in the workpiece coordinate remains unchanged at different spindle speeds in cylindrical turning.

(4) The relative distance between the spindle axis and the tool tip varies at different spindle speeds. The experiment results indicate that the mean value of the machined depth along the circumference of each groove changes at different speeds due to the variation of the relative distance.

Chapter 4 Investigation on the position drift of the axis average line of aerostatic bearing spindle

4.1 Introduction

With the increasing demand for components with ultra-precision accuracy and ultra-smooth surface roughness in modern industry, the ultra-precision single point diamond turning (SPDT) technique has been extensively adopted to manufacture these components, and accordingly popularize their applications in a variety of fields, including optical and photonic systems, telecommunications, aerospace, and biomedicine. With the SPDT, the spindle of the machine tool is a critical component in guaranteeing the machining accuracy. Due to the properties of low friction, low heat generation and simple structure, aerostatic bearing spindles are widely employed in ultra-precision machine tools (Yoshioka et al. 2006; An et al. 2010; Devitt 2009).

To estimate and control the quality of machined components, it is very important to understand the characteristics of the machine tool spindle before machining. The spindle error motion, which is the most common item to be evaluated, is usually evaluated by non-contact sensors targeting an artifact attached to the spindle rotor (Martin et al. 1995). For instance, Gao et al. developed an angular three-point method which utilized 2D slope sensors (Gao et al. 2002). This method can simultaneously measure the spindle radial and angular error motions

as well as the out-of-roundness of the artifact. Fujimaki and Mitsui utilized an auto-collimation to develop an optical system for measuring the radial error motion of a miniature ultra-high-speed spindle (Fujimaki and Mitsui 2007). Anandan and Ozdoganlar presented a laser Doppler vibrometry-based methodology to measure the axial and radial spindle error motions of a miniature ultra-high-speed spindle (Anandan and Ozdoganlar 2013). The obtained measurement data included both the spindle error motions and the form error of the artifact. Thus, to separate the spindle error motions from the form error of the artifacts, three classical error techniques have been proposed: the reversal, multi-step and multi-probe methods (Fujimaki and Mitsui 2007; Anandan and Ozdoganlar 2013; Cappa et al. 2014; Marsh et al. 2006; Donaldson 1972; Zhang et al. 1997; Anandan and Ozdoganlar 2015). The reversal technique is extensively utilized to separate the form error of the artifact from the spindle error motion (Donaldson 1972; Evans et al. 1996). This method needs two rounds of measurements to separate the two errors by rotating both the artifact and the probe through an angle of 180° around the spindle axis between the two rounds of measurements. Theoretically, the reversal technique can entirely separate the two errors. Multi-step and multi-probe techniques are alternative methods to the reversal technique. In the multi-step technique, the probe remains stationary during the measurement, whereas the artifact is indexed through equal angles (Marsh et al. 2006; Marsh 2010). The multi-probe technique simultaneously utilizes three or more probes to target the artifact. In general, all the three methods are capable of measuring the spindle error motions with a measurement uncertainty at the sub-nanometer level.

As discussed in Ref. (Lu and Jamalian 2011), the spindle error motion is defined as a relative motion between the spindle axis and the corresponding axis average line (AAL) in the reference frame. The AAL should remain stationary during the measurement of the spindle error motion at a given spindle speed. However, the position of this AAL can drift in an unpredicted way due to thermal and air flow instability, and external disturbances. With respect to the aerostatic bearing spindle used in ultra-precision machine tools, the thermal effect has a relatively small effect on the position drift under good cooling conditions. Nevertheless, because of the hydrodynamic effect of the aerostatic bearing, the position of the AAL can drift away from the center of the bearing stator, and this can lead to significant drift of the AAL position (Chen et al. 2010; Matta et al. 2010; Tala-Ighil et al. 2011; Kango et al. 2012).

In ultra-precision machining, the position drift of the AAL of the spindle axis is commonly in the range of several hundreds of nanometers, which may significantly increase the form error of the machine components. However, few studies have been reported on this issue. Thus, this chapter gives a detailed discussion on the position drift of the AAL induced by the hydrodynamic effects and its influence on the generation of the microstructures on the roller surfaces.

4.2 Theoretical analysis

In terms of the spindle error motions, two critical concepts should be introduced before the analysis, namely the axis of rotation (AOR) and axis average line (AAL) (Lu and Jamalian 2011). The AOR is a line fixed on the rotor and vertical to the cross-sectional plane of the rotor, and also the rotor rotates around it. The

AAL is defined as the spatial mean location of the AORs over many revolutions in the reference frame.

4.2.1 AAL drift due to hydrodynamic effect

For the air bearing, either aerostatic or hydrodynamic journal bearings, the air film thickness along the circumferential direction is not homogeneous (Chen et al. 2010; Matta et al. 2010; Tala-lghil et al. 2011; Kango et al. 2012). Therefore, the equilibrium position of the rotor is not at the center of the bearing as shown in Fig. 4.1. In general, the air film thickness is determined by the centricity e and the attitude angle φ at steady state, which can be expressed by:

$$\bar{h}(\theta, \bar{z}) = 1 + \varepsilon \cos(\theta - \varphi) \tag{4.1}$$

where $\bar{h} = (h/c)$, and h and c denote the local film thickness and the radial clearance of bearing respectively; eccentricity ratio $\varepsilon = e/c$; $\bar{z} = (z/(L/2))$, and z and L are the axial coordinate and length of bearing; θ is the angular coordinate.

The distribution of the corresponding pressure along the circumferential direction under the applied load F is governed by the non-dimensional Reynolds equation (Chen et al. 2010):

$$\frac{\partial}{\partial \theta}\left[\bar{h}^3 \frac{\partial \bar{P}^2}{\partial \theta}\right] + \left(\frac{D}{L}\right)^2 \frac{\partial}{\partial \bar{z}}\left[\bar{h}^3 \frac{\partial \bar{P}^2}{\partial \bar{z}}\right] = 2\Lambda \frac{\partial}{\partial \theta}\left[\bar{P}\bar{h}\right] \tag{4.2}$$

where $\bar{P} = (P/P_s)$, P is the pressure at the feeding hole, and P_s is the supply pressure; $\Lambda = \left(6\mu\omega / \left(P_s(c/R)^2\right)\right)$, μ is the dynamic viscosity of lubricant, and ω and R denote the spindle speed and the radius of bearing respectively;

$D=2R$ is the diameter of bearing.

For a specific spindle error motion test, the AAL is stationary in the reference frame and the axis of rotation has a motion relative to AAL shown in Fig. 4.2. The relative motion is then defined as the spindle error motion. Nonetheless, position of the AAL may vary with respect to different working conditions, including different spindle speeds and different surrounding temperatures. For the aerostatic bearing spindle, the spindle speed is a critical factor to determine the equilibrium position of the rotor shown in Fig. 4.1. Different spindle speeds may lead to changes of the equilibrium positions of the rotor, and accordingly, lead to the position drift of the AAL of the rotor.
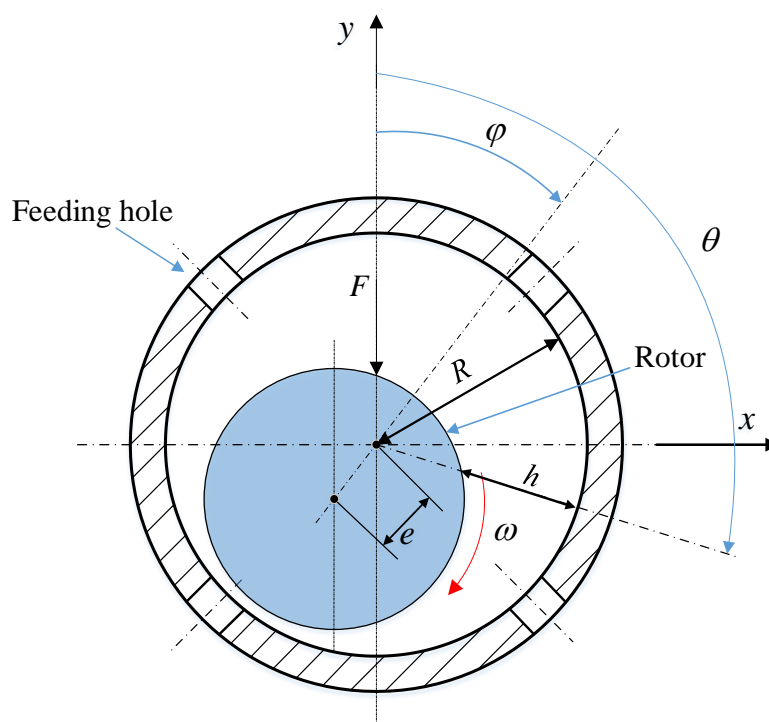
Fig. 4.1 Schematic of aerostatic bearing
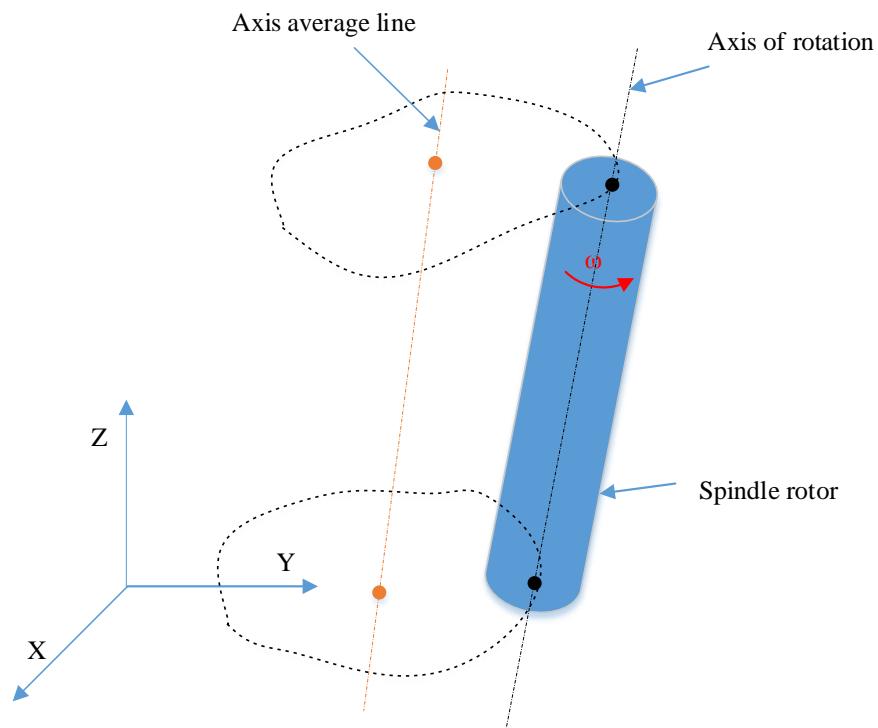
Fig. 4.2 Illustration of spindle error motion

4.2.2 Error model

In slow slide servo (S^3) assisted freeform surface turning, there are usually two machining steps. The first step is to machine a rough surface with a relatively high spindle speed and feedrate per revolution to serve as the reference. Then, this rough surface will be subjected to the S^3 based finish machining with relatively low spindle speed. The low speed is jointly caused by the servo operation of the spindle rotation and the much higher angular sampling ratio, which is required to guarantee the low interpolation error (Zhu and To 2015). Fig. 4.3 shows a S^3 machining on a roller surface. After rough turning of the roller surface, microstructures can then be fabricated on it on basis of the cylinder surface obtained in the first step rough turning. The relative distances between the AAL and the tip of the diamond tool in rough and S^3 machining are denoted

as d_1 and d_2, respectively. Ideally, the AAL remains unchanged for the two machining processes, namely:

$$d_1 = d_2 = \left| x_t - x_{O_s} \right|$$

(4.3)

where the x_t and x_{O_s} are the X-axis coordinates of the cutter tip P_t and the intersection point O_s of AAL and OXY plane. Actually, the AAL will change with respect to different spindle speeds, and this effect lead to the change of the relative distance between the tip of the diamond tool and the AAL. Thus, the actual distance is expressed as:

$$d_2 = \left| x_t - x_{O_s'} \right|$$

(4.4)

where $x_{O_s'}$ is the coordinate of the new intersection point O_s' of AAL and OXY plane due to position drift of AAL. The relative position drift of the AAL between different spindle speeds is denoted as d_e and can be expressed by:

$$d_e = \left| x_{O_s} - x_{O_s'} \right| = \left| e_1 \cdot \sin \varphi_1 - e_2 \cdot \sin \varphi_2 \right|$$

(4.5)

where e_1, e_2 are the eccentricities of the rotor of the aerostatic bearing during the rough and S^3 turning, respectively. φ_1 and φ_2 are the corresponding attitude angle (as defined in Fig. 4.1) during rough and S^3 turning.
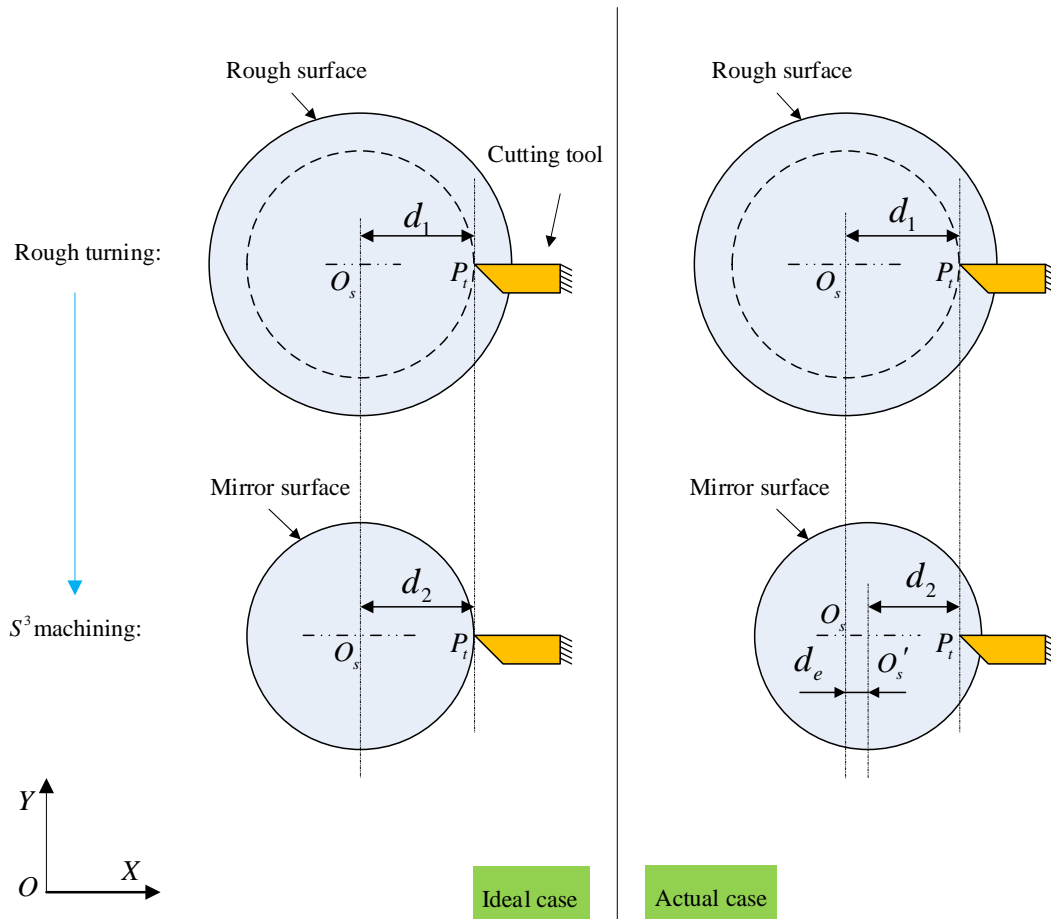
Fig. 4.3 Illustration of AAL drift between machining steps with different speeds

During machining, a variety of motion errors of the machine tool may contribute to the form accuracy of the generated microstructures through S^3 machining. Apart from the position drift of the AAL, the horizontal straightness error of the Z-axial slide parallel to the AOR, the out-of-parallelism between the AOR and the Z-axial slide, the radial spindle error motion and the position error of the X-axial slide may also lead to the form error of the machined microstructures. During rough turning, the comprehensive errors in the radial direction can be expressed by:

$$e_{rough}(x_1, z, \theta) = e_{spindle}(n_1, z, \theta) + e_{parallelism}(z) + e_{straightness}(z)$$
$$+ e_{drift}(n_1, z) + e_{position}(x_1)$$

(4.6)

where n_1 is the spindle speed used in rough turning, and the coordinate of the tip of cutting tool in rough turning is expressed by (x_1, z, θ).

During the fabrication of the microstructures through S^3, the comprehensive errors in the radial direction can be expressed as:

$$e_{S^3}(x_2, z, \theta) = e_{spindle}(n_2, z, \theta) + e_{parallelism}(z) + e_{straightness}(z)$$
$$+ e_{drift}(n_2, z) + e_{position}(x_2) \tag{4.7}$$

where n_2 is the spindle speed used in S^3 machining, and the coordinate of the tip of cutting tool in S^3 machining is expressed by (x_2, z, θ).

The comprehensive error of depth of cutting in S^3 machining consequently yields:

$$\Delta e(x_1, x_2, z, \theta) = e_{rough}(x_1, z, \theta) - e_{S^3}(x_2, z, \theta)$$
$$= \Delta e_{spindle}(n_1, n_2, z, \theta) + \Delta e_{drift}(n_1, n_2, z) + \Delta e_{position}(x_1, x_2) \tag{4.8}$$

As shown in Eq. (4.8), $\Delta e_{spindle}$ and $\Delta e_{position}$ may cause the variation of the error of depth of cut along the circumferential direction, whereas the Δe_{drift} results in a constant error of the depth of cut along the circumferential direction.

4.3 Experimental design

To identify the position drift of the AAL with respect to the variation of the rotation speeds, an experiment for the fabrication of the microstructures on a roller surface is conducted. The cylinder surface of the workpiece is divided into four different regions denoted as A, B, C and D shown in Fig. 4.4. This division makes it be possible to adopt different spindle speeds for rough turning of the

cylinder surface at different regions. Details of the cutting conditions employed for the rough turning are summarized in Table 4.1. There are four different spindle speeds utilized for rough tuning, meanwhile, a slow spindle speed of about 3.5 rpm is used for S^3 machining. The machining process is conducted on a Moore Nanotech 350FG ultra-precision machine tool (refer to Appendix Ⅲ), and the specifications of the machine tool are further shown in Table 4.2. A single crystal diamond cutting tool with 0.25 mm nose radius and zero rake angle is adopted for both rough turning and S^3 machining. The experimental setup is shown in Fig. 4.5.

Table 4.1 Cutting conditions for rough turning

Section	A	B	C	D
Spindle speed	3200 rpm	2200 rpm	1200 rpm	200 rpm
Feed rate	16 mm/min	11 mm/min	6 mm/min	1 mm/min
Cutting Depth	2 μm	2 μm	2 μm	2 μm

Table 4.2 Nanotech 350FG specification

Travel	X-axis: 350 mm; Z-axis: 300 mm
Straightness error	X-axis: 0.3μm over full travel; Z-axis: 0.3μm over full travel
Spindle motion accuracy:	Axial: ≤12.5 nanometers; Radial≤12.5 nanometers
Temperature control of spindle:	±0.5°F
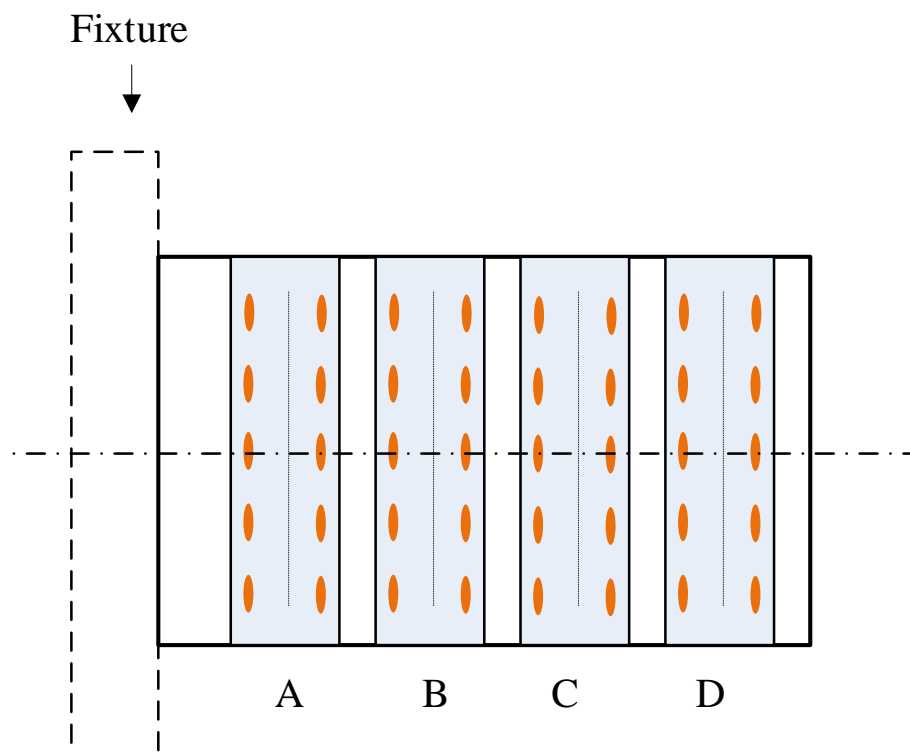
Fig. 4.4 Schematic of the workpiece
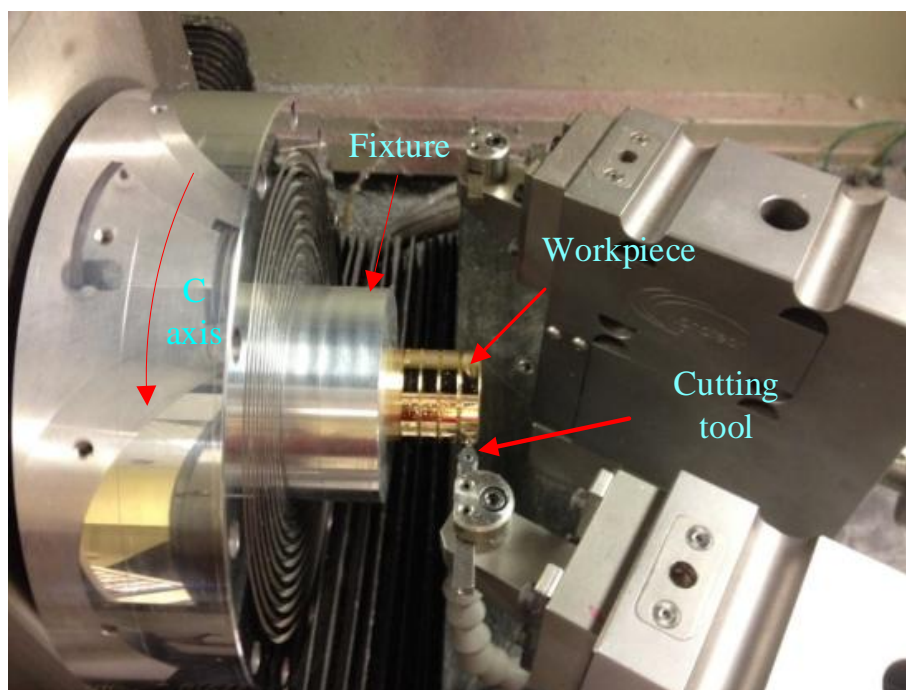
Fig. 4.5 Experimental setup

After the rough turning, the obtained surface of the roller will be employed as the reference for further generation of the microstructures through S^3 machining. To avoid the impact effects of large acceleration and deceleration of the servo motions, a smooth tool path is selected for the fabrication of the microstructures as shown in Fig. 4.6.

Tool path locus

Cylindrical surface

Microstructure
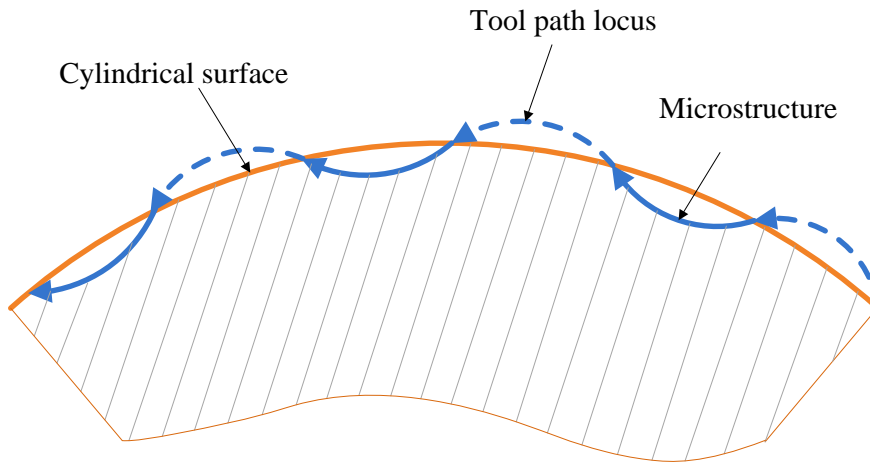
Fig. 4.6 Illustration of smooth tool path

Assuming that the spindle rotates at a constant speed n, the rotational angle of the spindle can be expressed as:

$$\theta = 2\pi \cdot n \cdot t / 60 \tag{4.9}$$

The tool path for the S^3 machining process is obtained by:

$$\begin{cases} C = \mathrm{mod}(\theta, \ 2\pi) \\ X = A_x \cdot \sin(n \cdot C) \\ Z = Z(t) \end{cases} \tag{4.10}$$

where $\mathrm{mod}(\cdot)$ is the modulus operator to transfer the continuous rotational angle of C-axis into the range $[0, \ 2\pi)$; A_x is the amplitude of the tool oscillation along the radial direction; n denotes the number of microstructures

for one revolution. To reduce the influence of the interpolation error, a sampling ratio of 0.02^o is used for C-axis discretization in the S^3 machining.

For each region of the workpiece, when rough turning of each section is completed, the microstructures in this region will be immediately machined by using the S^3 machining. It is noteworthy that the machining time for the fabrication of the microstructures in each region is only several minutes. Thus, effects of the thermal errors on the machining can be ignored here. In the experiment, the amplitude of the generated microstructures is set to be 1 μm, and there are totally 250 microstructures in one revolution. The pitch of the microstructures along axial direction is set as 60 μm. Two brass workpieces (named No.1 and No.2) with a radius of 16 mm are employed in this experiment.

Apart from the AAL drift in radial direction, the angular drift of AAL may also exist with different spindle speeds. To verify the existence of the angular drift, another cutting experiment is also conducted. In this experiment, a given spindle speed is adopted for the rough turning of the cylindrical surface. Then three sets of microstructures are machined on three different axial positions of the cylindrical surface with a constant interval of 7 mm as shown in Fig. 4.7. Two workpiece combined with two rough turning spindle speeds of 200 rpm and 3200rpm are used.
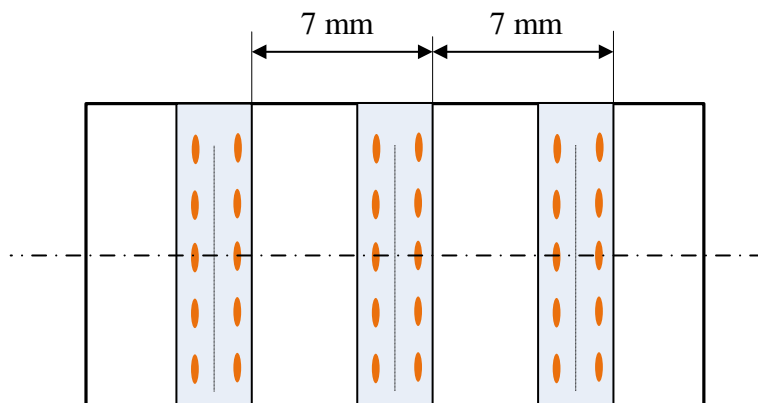
Fig. 4.7 Schematic of workpiece for identification of the drift of AAL along axial direction

4.4 Results and discussion

For each region, as the number of the machined microstructures is large, only 25 groups of microstructures are measured with an even space along the circumferential direction of the roller as illustrated in Fig. 4.8. Each group contains seven microstructures as shown in Fig. 4.8 and Fig. 4.9. The three-dimensional (3-D) micro-topography of the microstructure is obtained by an Optical Surface Profiler (Zygo Nexview) (refer to Appendix Ⅱ), and the microstructure is further analyzed through the corresponding software Mx.

Fig. 4.9 shows the representative results of the 25 groups of the machined microstructures in each region. The practical amplitudes of the microstructures increase with the increase of the spindle speed. For instance, the practical amplitude is about 1.15μm with spindle speed of 200 rpm, while that is about 1.75μm with spindle speed of 3200 rpm. Consequently, the length and maximum width of the microstructures also increase with the increase of the spindle speed.

Nonetheless, the amplitudes of the microstructures in the same section almost remain unchanged along the axial direction of workpiece, and only very small fluctuation is observed which is due to the spindle asynchronous error motion. This phenomenon demonstrates the assumption that the effects of thermal error on the microstructure generation can be neglected during this short time.
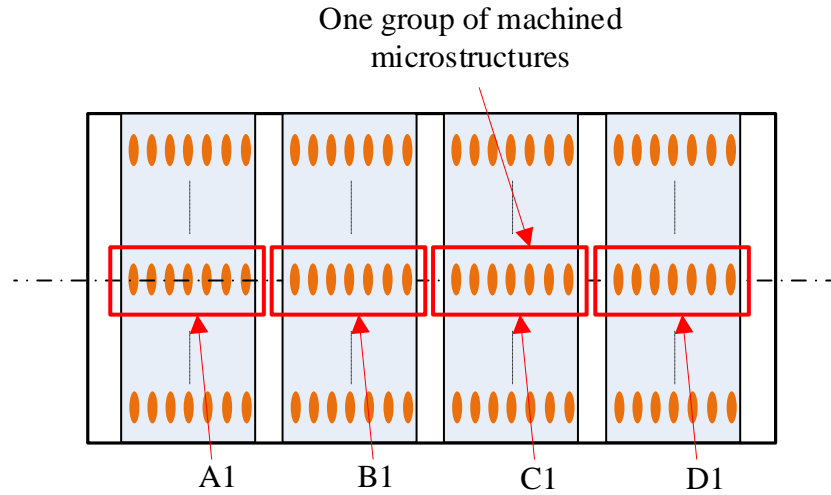
Fig. 4.8 Illustration of one group of measured microstructures in each region
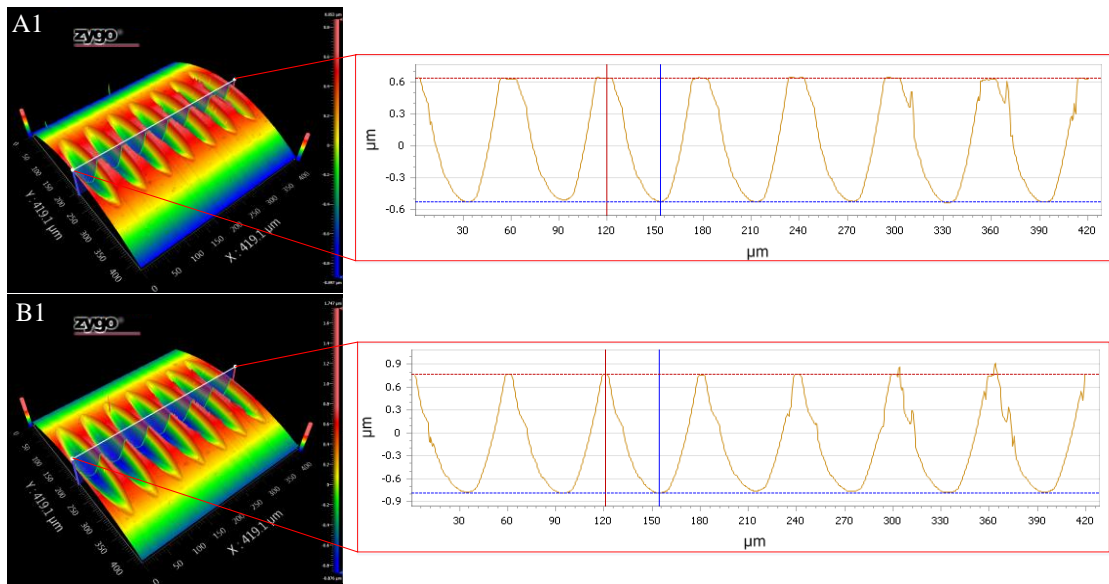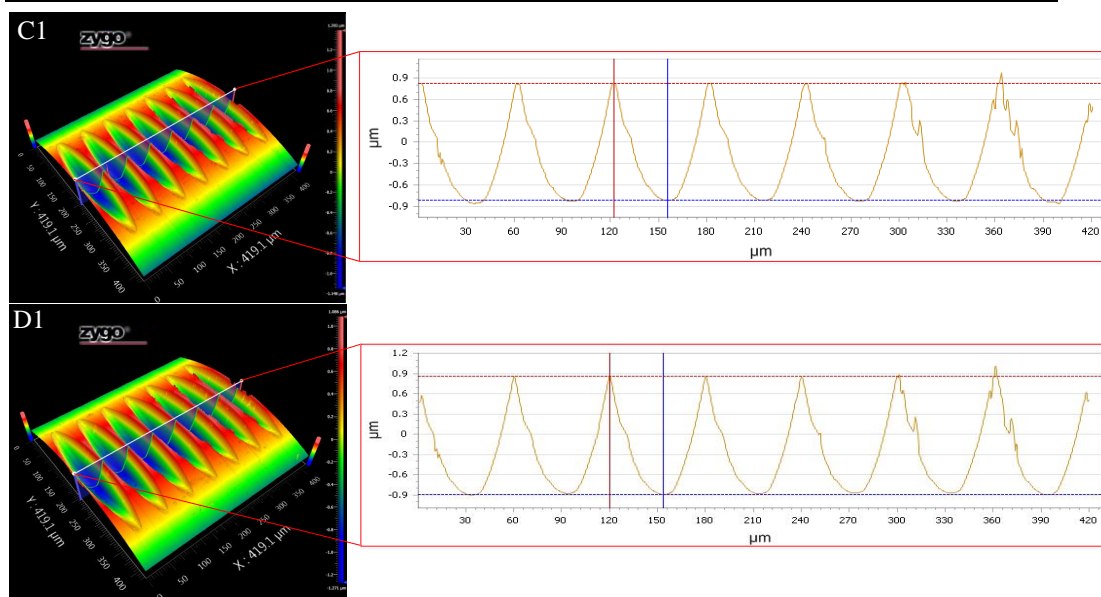
Fig. 4.9 Machined microstructures with different spindle speeds: A1) 200 rpm, B1) 1200 rpm, C1) 2200 rpm, D1) 3200 rpm.

The form error of the microstructures along the circumferential direction has not been evaluated yet. Thereby, the amplitudes of the microstructures obtained in each region are evaluated based on the measurement results of the 25 groups of each region. The amplitude errors of both the two workpieces (i.e. No.1 and No.2) are illustrated in Fig. 4.10, where the amplitude errors have very small fluctuations no matter which spindle speed is used. According to Eq. (4.8), the fluctuations are related to the spindle error motions which include the spindle unbalance induced error motion. As the parameters x_1 and x_2 in Eq. (4.8) for amplitude of microstructures remain unchanged along the circumferential direction, the positioning error has not influence on the fluctuation. For unbalance induced error motion, as it is a fundamental component (once per revolution), it can be observed from the fluctuations if it has significant contribution to spindle error motions. When relatively high spindle speeds, namely 3200 rpm, 2200 rpm and 1200 rpm, are employed, the spindle unbalance

induced eccentricity can be significantly observed as shown in Fig. 4.10b. However, this phenomenon is not significantly observed when using a very low spindle speed (200 rpm). This is consistent with the property of the unbalance induced error motion. This phenomenon is also not be significantly observed in Fig. 4.10a because of the better balancing operation.

Based on the definition of spindle error motion, the AAL is related to the mean value of the position of spindle axis. Therefore, the mean values of the amplitude errors along the circumferential direction is used to evaluate the position drift of the AAL as shown in Fig. 4.11, where the effect of the fluctuation of amplitude error along the circumferential direction is reduced. Considering the relationship shown in Eq. (4.8), the positioning error of the X-axial slide and the position drift of the AAL during turning have contribution to the mean values of the amplitude errors. However, the positioning error is independent on the spindle speed as described in Eq. (4.8). So the variation of the mean value of the amplitude errors with the spindle speeds as shown in Fig. 4.11 is only related to the position drift of the AAL.

In addition, the time interval between the rough turning and S^3 machining and the machining time in S^3 machining are tens of seconds and several minutes, respectively. The form errors of the machined microstructures in each region have few changes along the axial direction. This indicates that the thermal effect can be neglected, and only the position drift of AAL due to the hydrodynamic effect of aerostatic bearing can contribute to the variation of amplitude with respect to spindle speeds.
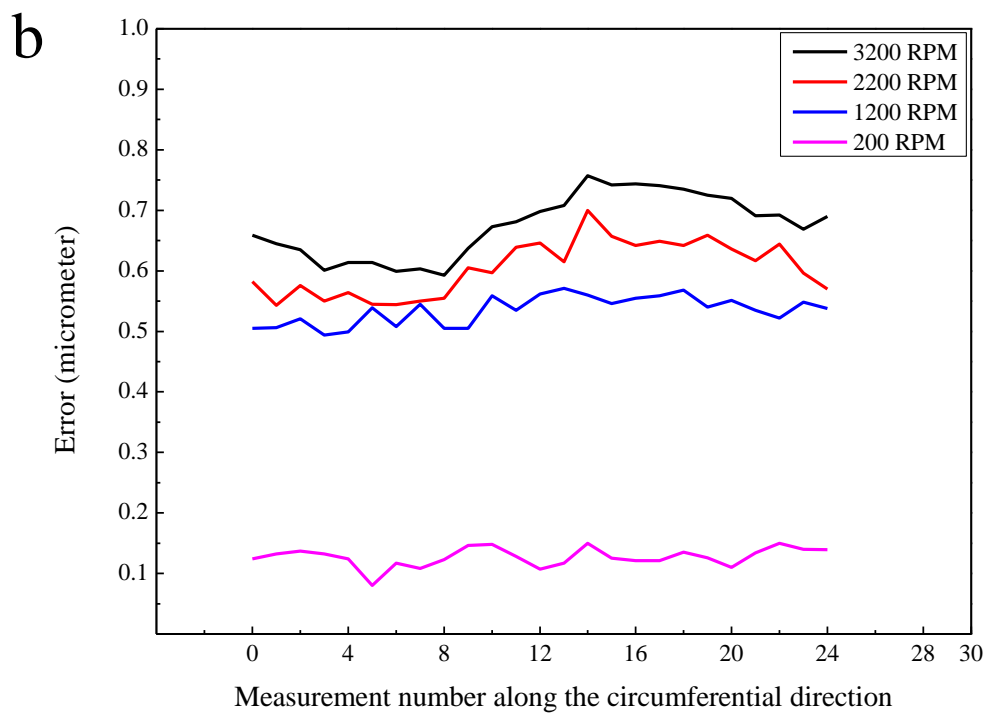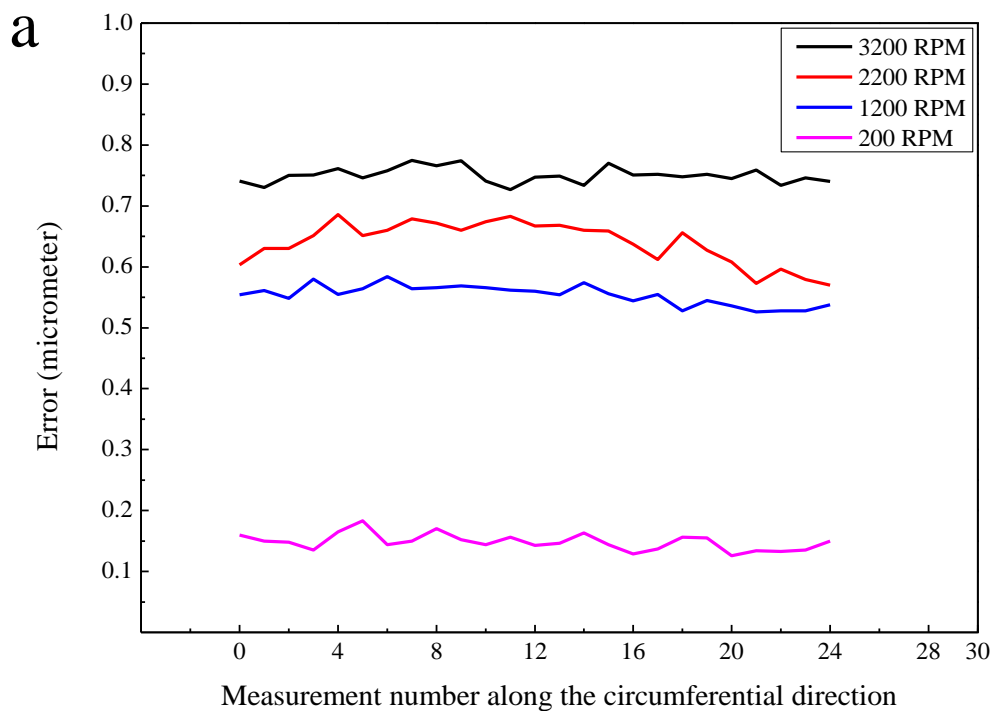
Fig. 4.10 Machined errors on the circumference: a) No.1, b) No.2.
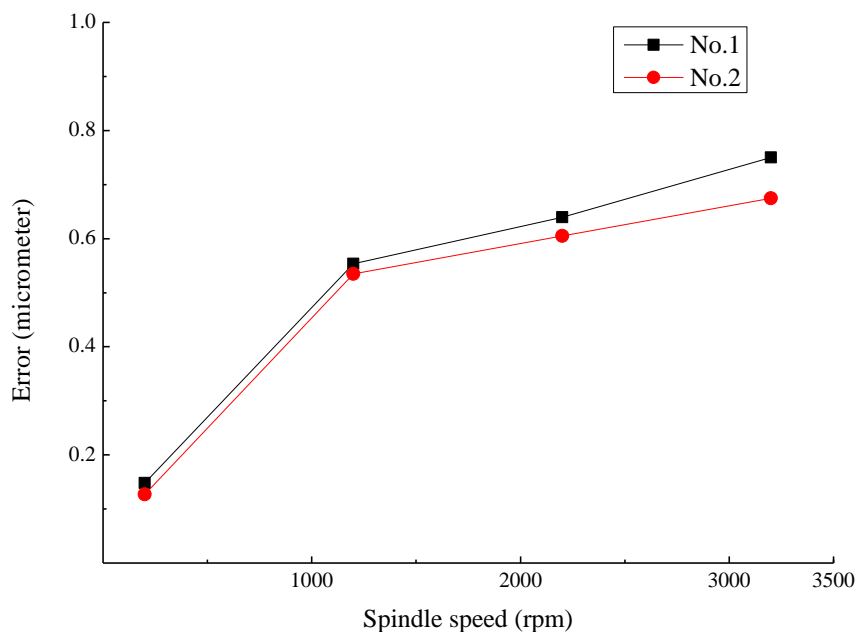
Fig. 4.11 Drift of spindle rotation axis with variation of spindle speed

As illustrated in Fig. 4.3, when different spindle speeds are adopted for rough cutting, the AAL will drift away from its static position. This makes the actual cutting depth smaller in rough cutting, whereas the actual cutting depth becomes larger in S^3 machining where only one very small spindle speed is used for S^3 machining. Larger position drift of the AAL in rough cutting means larger actual cutting depth in S^3 machining. Larger actual cutting depth in S^3 machining generates larger amplitude error of the machined microstructure. As shown in Fig. 4.11, the amplitude errors increase with the increase of the spindle speed. This indicates that the position drift of the AAL increases with the increase of the spindle speed. It can be seen that the variations of the position drift of the AAL in terms of the spindle speed are consistent for the two workpieces. Moreover, the relation between the position drift of the AAL and the spindle speed is nonlinear.

Fig. 4.12 shows the experimental result of the position drift of AAL at different axial positions of the workpiece. For spindle speed of 3200 rpm in the experiment, the increment of position drift for the length of every 7 mm along the axial direction is about 50 nm, whereas the increment is around 110 nm for spindle speed of 200 rpm. This indicates that angular drift of the AAL exists for the aerostatic bearing spindle.
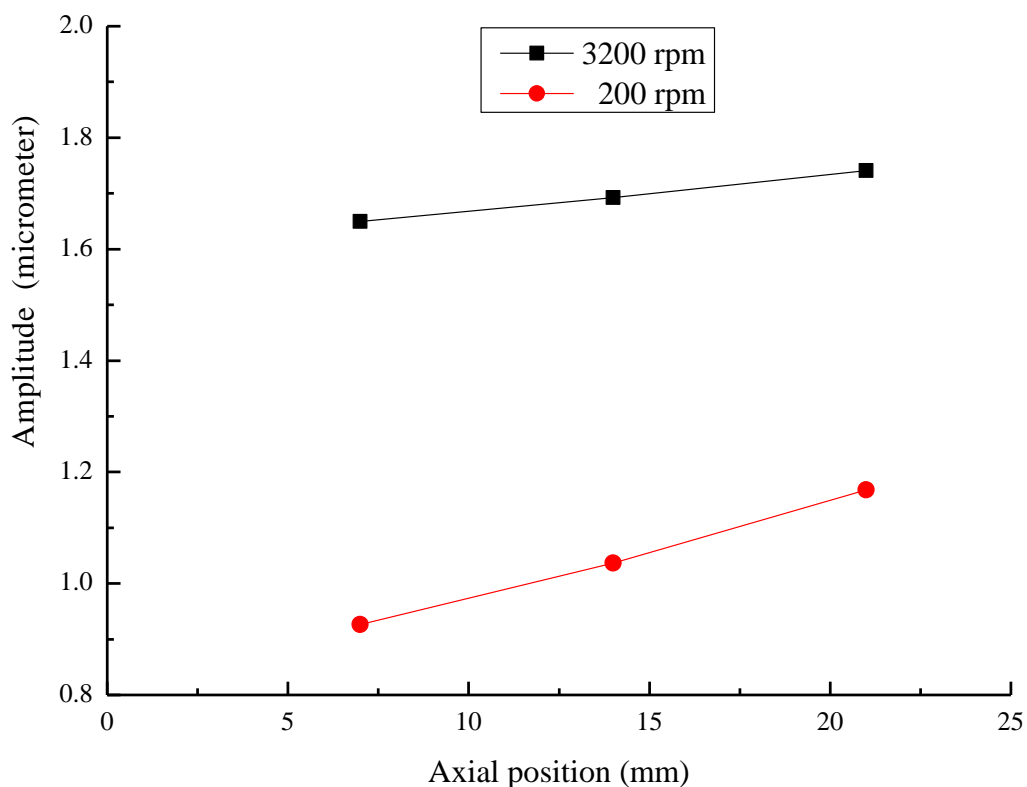
Fig. 4.12 Position drift of the AAL at different axial positions

4.5 Summary

The chapter aims to investigate the position drift of the axis average line (AAL) of the aerostatic bearing spindle, and its effects on slow slide servo (S^3) assisted diamond turning of microstructures on roller surfaces. An error model is developed to analyze the error of depth of cut during two consecutive machining

steps, i.e. the rough turning and S^3 machining. An experiment of the fabrication of the microstructures through the S^3 machining is conducted to validate the position drift of the AAL. The main conclusions are drawn as follows:

(1) The analysis based on the developed error model reveals that the error of depth of cut during the S^3 machining is mainly dependent on the spindle error motion, the positioning error of the X-axial slide and position drift of the AAL. In addition, the thermal effects during the machining can be neglected when machining within a short time.

(2) For each region on the workpiece, the amplitude of the microstructures fluctuates along the circumferential direction, which are mainly caused by the spindle error motion, i.e. the spindle unbalance induced eccentricity. On the other hand, the amplitude remains almost unchanged in the axial direction, indicating that the thermal effect can be neglected during this short machining process.

(3) The AAL drifts further away from the bearing center with the increase of spindle speed. This results in the increase of the amplitude of microstructure. The measurement results of the machined microstructures indicate that the variation of the position drift in terms of spindle speed is nonlinear. In addition, the position drift of AAL slightly varies at different axial positions of spindle due to the angular drift of AAL.

Chapter 5 Algorithm for surface generation and cutting force calculation

5.1 Introduction

In Chapter 3 and Chapter 4, the spindle dynamic error motions have been analyzed with both theoretical and experimental approaches. Although a spindle dynamic model was developed in Chapter 3, the actual cutting process has not been considered and only constant cutting forces are used in the model. Motivated by this, a comprehensive model considering the actual cutting process is proposed based on the work in Chapter 5 and Chapter 6. In this chapter, an algorithm is firstly developed for the cutting force and surface topography, which will is incorporated with the spindle dynamic model and error model in order to construct the comprehensive dynamic model which is discussed in Chapter 6.

In this algorithm, the position and attitude of the cutting tool is described in the fixed coordinates of the cylindrical workpiece with a coordinate transformation operation. The initial surface of the cylindrical workpiece is defined by discretizing the workpiece in both the axial and circumferential directions. The cutting force can be calculated by considering the relative position between the cutting tool and the workpiece, and the new surface of the workpiece can be obtained at the same time.

As the ultra-precision cutting process is conducted in the micron range, the effects of minimum chip thickness and elastic recovery are usually significant, these effects are taken into account in the algorithm.

5.2 Chip thickness and cutting force calculation

5.2.1 Discretization of the workpiece

The cylindrical workpiece is discretized in the both circumferential and axial directions, with increments $\Delta\theta$ and Δz respectively in the workpiece cylindrical coordinates, as shown in Fig. 5.1. An arbitrary point of the workpiece is expressed as (ρ, θ, z) in the cylindrical coordinate system, where ρ denotes the surface height of the workpiece in the radial direction. The spindle rotational speed is regarded as a constant and denoted as n. The time step for the model is then determined by the following equation:

$$\Delta t = \Delta\theta / \left(n \cdot 2\pi/60\right) \tag{5.1}$$

The coordinates of the cutting tool tip in the workpiece cylindrical coordinate system are:

$$\rho_t = X_0 + X(t) \tag{5.2}$$

$$\theta_t = \theta_0 + 2\pi nt / 60 \tag{5.3}$$

$$z_t = Z_0 + Z(t) \tag{5.4}$$

where X_0 and Z_0 represent the initial positions of cutting tool tip in the reference coordinate system, θ_0 is the initial azimuth of the tool tip in the workpiece cylindrical coordinate system, and $X(t)$ and $Z(t)$ represent the tool

path in the reference coordinate system.
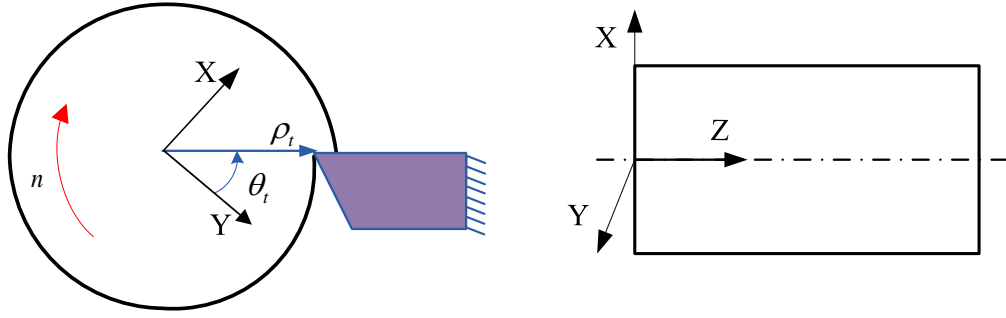
Fig. 5.1 Schematic of the tool tip coordinate in workpiece coordinate system

As the workpiece has been discretized by the mesh grid, θ_t and z_t must be rounded to the nearest mesh point $(\hat{\theta}_t, \hat{z}_t)$. The workpiece surface height at the mesh point corresponding to the tool tip is:

$$\rho_w = \rho(\hat{\theta}_t, \hat{z}_t) \tag{5.5}$$

At each time step, in order to determine the undeformed chip thickness and the corresponding cutting force the workpiece surface points swept by the cutting tool must firstly be found out. Since only the radial tool vibration is considered, the axis of the cylindrical workpiece is assumed in the tool rake face plane (the rake angle of the cutting tool is zero in the present study) and the thrust direction of the cutting tool is perpendicular to the axis of the cylindrical workpiece. Thus, the surface points swept by the cutting tool have the same azimuth coordinate $\hat{\theta}_t$ and the mesh points at $\hat{\theta}_t$ can be denoted as:

$$G_{\hat{\theta}_t} = \left\{ (\hat{\theta}_t, z_i) \mid i \in \left[1, \, round(|z_a - z_b|/\Delta z) \right] \right\} \tag{5.6}$$

and the workpiece surface points at azimuth $\hat{\theta}_t$ are denoted as:

$$S_{\hat{\theta}_t} = \left\{ (\rho(\hat{\theta}_t, z_i), \hat{\theta}_t, z_i) \right\} \tag{5.7}$$

where $round(\cdot)$ denotes the rounding operator, $\rho(\cdot)$ denotes the surface height

of the workpiece at the corresponding mesh point, and $z_i = z_a + (i-1) \cdot \Delta z$ is for

$z_i \in [z_a, z_b]$.

5.2.2 Searching the surface points swept by the cutting tool

The cutting process is illustrated in Fig 5.2 where the cutting plane is located at

$\hat{\theta}_t$. The surface points swept by the cutting tool are denoted as:

$$S_{swept} = \left\{ P_i \mid |P_i O_t| < r_t \right\} \tag{5.8}$$

where $S_{swept} \subseteq S_{\hat{\theta}_t}$, P_i is the corresponding surface point at $(\hat{\theta}_t, z_i)$, O_t is the

cutting tool central point in the cutting plane, and R_t is the tool nose radius. The

corresponding mesh points of S_{swept} are denoted as:

$$G_{swept} = \left\{ (\hat{\theta}_t, z_i) \mid |P_i O_t| < r_t \right\} \tag{5.9}$$

Fig. 5.2 Illustration for searching surface points swept by the cutting tool at $\hat{\theta}_t$

azimuth

The set mesh point G_{swept} can be divided into several subsets and the corresponding mesh points of successive surface points are included in the same subset:

$$G_{swept} = \{G_1, ..., G_l, ..., G_m\} \tag{5.10}$$

5.2.3 Cutting force calculation

The calculation of elemental uncut chip thickness and cutting force, and the surface updating are all implemented and constrained in each mesh point subset. The elemental uncut chip thickness is:

$$t_c = \overline{Q_i P_k} \tag{5.11}$$

where Q_i is a point on the cutting edge at mesh point $(\hat{\theta}_t, z_i)$, P_k is the intersection between the line $\overline{O_t Q_i}$ and the previous machined workpiece surface. The elemental width of cut is:

$$db = \overline{Q_i Q_{i+1}} \tag{5.12}$$

To take into account of the effect of the tool edge radius in the micro cutting process, the cutting force is regarded as a piecewise function of the uncut chip thickness (Liu et al. 2004). When the uncut chip thickness is larger than a certain limit value $t_{c\max}$, which will be introduced in Section 5.2.4, the elemental cutting force is:

$$\begin{cases} dF_t = (K_{tc} t_c + K_{te}) db \\ dF_c = (K_{cc} t_c + K_{ce}) db \end{cases} \tag{5.13}$$

If the uncut chip thickness is less than $t_{c\max}$, another function is employed:

$$\begin{cases} dF_t = A_{tw} \cdot \left(\dfrac{t_c}{t_{c\max}} \right)^{A_{tt}} dw \\[4mm] dF_c = A_{cw} \cdot \left(\dfrac{t_c}{t_{c\max}} \right)^{A_{ct}} dw \end{cases} \qquad (5.14)$$

where A_{tw}, A_{tt}, A_{cw} and A_{ct} are coefficients. In Eq. (5.13) and Eq. (5.14), the direction of thrust cutting force is along the normal direction of the cutting edge. The elemental thrust cutting force should be transformed into radial and axial direction in the workpiece coordinate and then the cutting force at each time step is the summation of all the transformed elemental cutting forces:

$$\begin{cases} F_t = \sum dF_t \cos\phi_i \\ F_c = \sum dF_c \\ F_f = \sum dF_t \sin\phi_i \end{cases} \qquad (5.15)$$

where ϕ_i is the azimuth angle of the elemental thrust force.

5.2.4 Surface point updating

The updated surface point is denoted as $P_{k'}$, which is dependent on the elastic recovery:

$$t_{elastic} = \overline{Q_i P_{k'}} \qquad (5.16)$$

In the present study, an assumption of the elastic recovery is that if the undeformed chip thickness is less than the minimum chip thickness, the material only undergoes elastic deformation. When the undeformed chip thickness is larger than the minimum chip thickness and less than a certain chip thickness $t_{c\max}$, the chip is formed and combined with a portion of elastic recovery. The material is entirely removed when the undeformed chip thickness is larger than the thickness $t_{c\max}$. The assumption of elastic recovery can be expressed as the

following equation:

$$t_{elastic} = \begin{cases} 0, & t_{c\max} < t_c \\ t_{c\min} \cdot \dfrac{t_c - t_{c\max}}{t_{c\min} - t_{c\max}}, & t_{c\min} \le t_c \le t_{c\max} \\ t_c, & 0 \le t_c < t_{c\min} \end{cases} \qquad (5.17)$$

where $t_{c\min}$ represents the minimum chip thickness, and $t_{c\max}$ denotes the upper limit of chip thickness for elastic recovery.

The surface point $P_{k'}$ is then determined based on this assumption. For a mesh point subset G_l, the entire corresponding updated surface points are generated with the same procedure by traversing all the mesh points of the subset and these updated surface points are denoted as S_{update_l}. The updated surface points can have influence on the succeeding cutting process.

5.3 Experimental and simulation setup

To investigate the effect of tool edge radius on the cutting force in micro turning, two micro-groove cutting experiments were conducted with a fresh tool and a slightly worn diamond tool respectively. In these experiments, several grooves were machined on the cylindrical surface with different feed rates. The experimental conditions are summarized in Table 5.1. The experimental setup is shown in Fig. 5.3. A force sensor is mounted on the tool holder to measure the cutting force. During the groove cutting, the diamond tool keeps moving in the radial direction of the cylindrical workpiece at a given feed rate to remove the work material until the cutting tool tip reaches the given depth of groove. Then the tool remains still and maintains contact with the workpiece surface for a

while, and the cutting tool will eventually move away from the workpiece.

Table 5.1 Cutting conditions

Tool material	Diamond
Tool rake angle	0°
Tool clearance angle	10°
Tool nose radius	0.24 mm
Workpiece material	Al6061
Workpiece diameter	15 mm
Spindle speed	2000 rpm
Feed rate	0.5, 1, 1.5 mm/min
Nominal depth of groove	3 μm

a
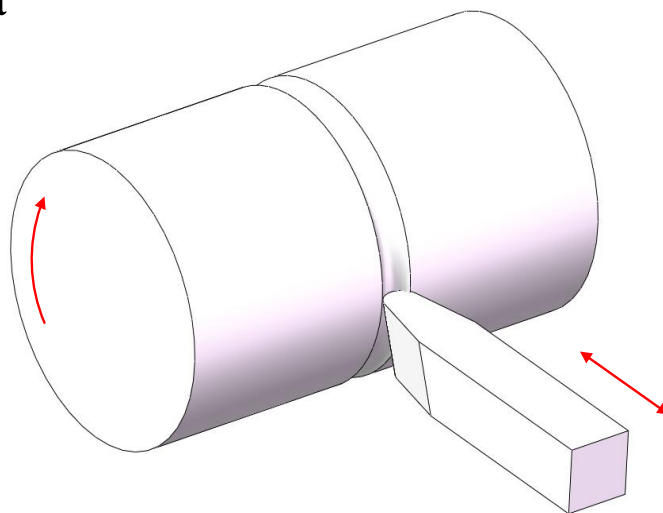
Fig. 5.3 Experimental setup

Only the cutting force and thrust force are considered in the present study as they make the main contribution to the machining dynamics in cylindrical turning. The cutting force coefficients used for simulation are K_{tc} =280, K_{te} =0.33, K_{cc} =1410, K_{ce} =0.2007, A_{tw} =0.4, A_{tt} =1.3569, A_{cw} =0.5532 and A_{ct} =4.1423, based on cutting test results. The cutting conditions taken for simulation are the same as the experimental conditions.

5.4 Results and discussion

5.4.1 Effect of tool edge radius on cutting force

In the groove cutting experiment shown in Fig. 5.3, the tool displacement relative to the uncut cylindrical surface and the nominal cutting depth at the tool tip vary with time as shown in Fig. 5.4. The tool displacement increases linearly until it is

equal to the depth of the groove at time t_2, and then the tool will remain still before the cutting process is completed at time t_4. Differing from the variation of the tool displacement, the nominal cutting depth at the tool tip only increases in the first revolution, and then it remains unchanged until time t_2. From time t_2 to t_3, the cutting depth decreases to zero and it will remain zero from t_3 to t_4 if the elastic recovery has not been considered during this period.
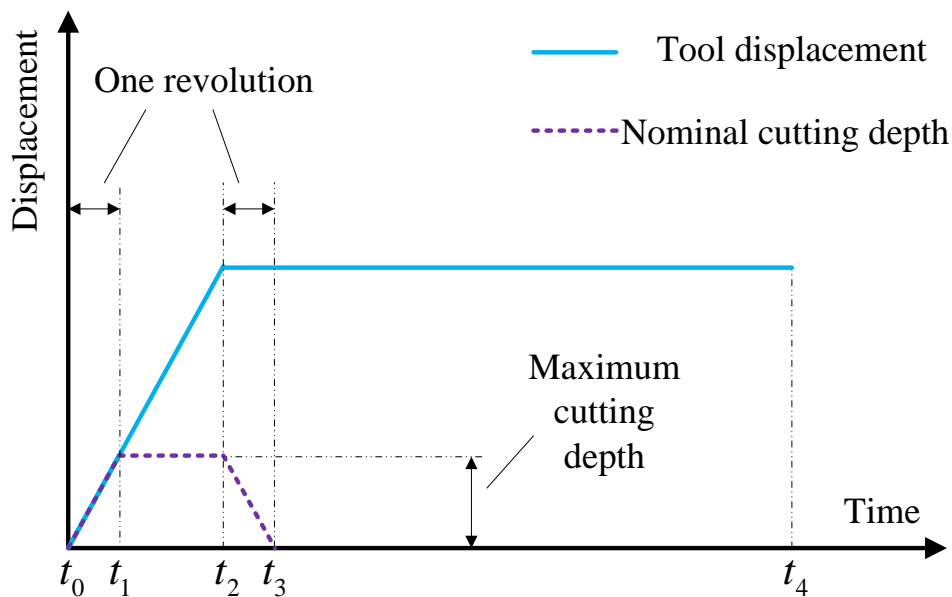
Fig. 5.4 The variation of tool displacement and nominal cutting depth without consideration of elastic recovery

As shown in Fig. 5.5, the measured cutting force significantly undergoes cutting and rubbing phase. During the rubbing phase, the cutting force is not equal to zero even though the nominal cutting depth is zero in the rubbing phase, and the cutting force fluctuates with spindle rotating frequency. This indicates that the material cannot be entirely removed due to elastic recovery. As shown in Fig. 5.4, there is a maximum cutting depth for the cutting process, and the maximum cutting depths for cutting with feed rates of 0.5, 1 and 1.5 mm/min are 250 nm, 500 nm and 750 nm respectively. The cutting force during the rubbing phase is

continuous for feed rate of 0.5, whereas it is intermittently for feed rates of 1 and 1.5 mm/min as shown in Fig. 5.5. This means that a portion of cutting depths during the period of t_3 to t_4 is larger than the upper limit of chip thickness $t_{c\max}$ for elastic recovery for feed rate of 1 and 1.5 mm/min, whereas all cutting depths are less than $t_{c\max}$ for feed rate of 0.5 mm/min. So $t_{c\max}$ is in the range of 250 to 500 nm. For feed rate 1 and 1.5 mm/min, the ratio of $t_{c\max}$ to the maximum cutting depth is equal to the duty ratio of the cutting force in each rotating period of spindle in the rubbing phase. Based on this principle, the estimated value of $t_{c\max}$ is about 250 nm in this experiment. Similarly, as the peak value of the cutting force in the rubbing phase corresponds to the minimum chip thickness, the estimated value of minimum chip thickness is about 150 nm by considering the ratio of minimum chip thickness to maximum cutting depth of the corresponding feed rate in the experiment, even though the tool edge radius is unknown in the experiment.

a1
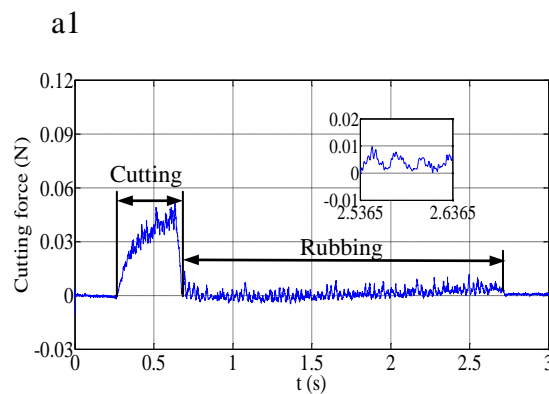
a2
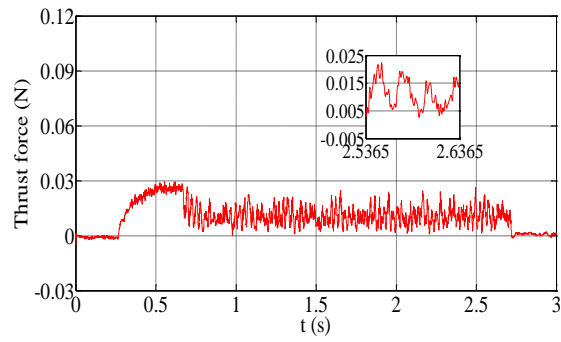
b1
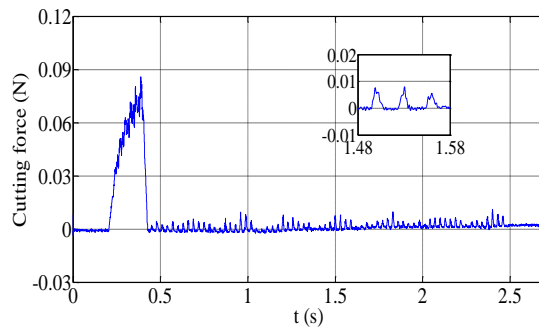
b2
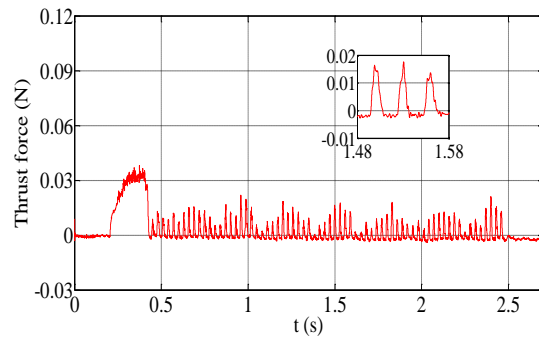
c1
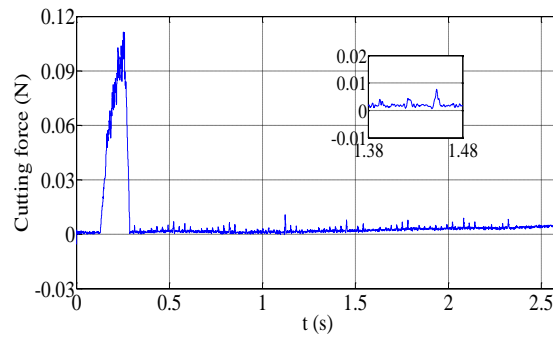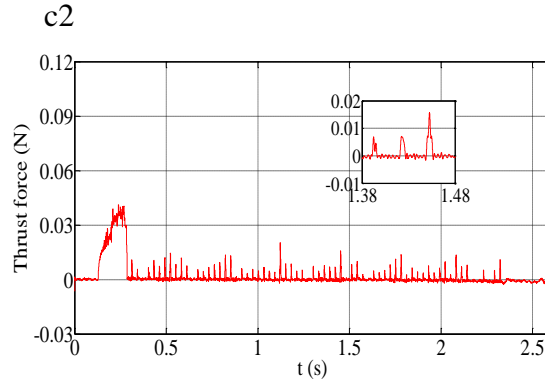
Fig. 5.5 Measured force in groove cutting with fresh tool: (a) 0.5 mm/min, (b) 1 mm/min, (c) 1.5mm/min.

5.4.2 Comparison between simulated and measured cutting force

For the simulating cutting force based on the prediction algorithm, $t_{c\max}$ of 250 nm and the minimum chip thickness of 150 nm are adopted. The simulated values are shown in Fig. 6, where the effect of minimum chip thickness and elastic recovery is taken into account. The measured and simulated peak values of the cutting force in cutting and rubbing phase are shown in Table 2. Due to the fluctuation of force in rubbing phase, the mean value of the measured peak values in rubbing phase is used to represent the peak force of rubbing phase in Table 2.

Table 5.2 Comparison of peak cutting forces in the cutting and rubbing phase

Feed rate (mm/min)	Cutting force (N)				Thrust force (N)			
	Cutting phase		Rubbing phase		Cutting phase		Rubbing phase	
	Measured	Simulated	Measured	Simulated	Measured	Simulated	Measured	Simulated
0.5	0.0437	0.0407	0.0053	0.0048	0.0276	0.02953	0.0152	0.0144
1	0.0767	0.0657	0.0047	0.0048	0.0339	0.0346	0.0117	0.0144
1.5	0.1024	0.0894	0.0024	0.0048	0.0379	0.03926	0.0073	0.0144

a1

a2

b1

b2

c1
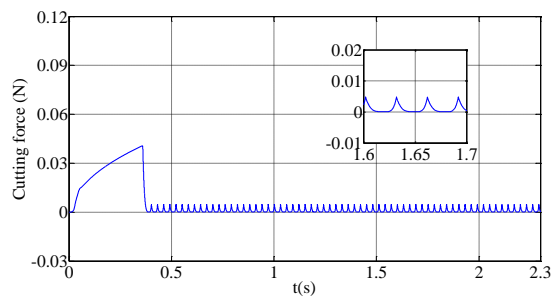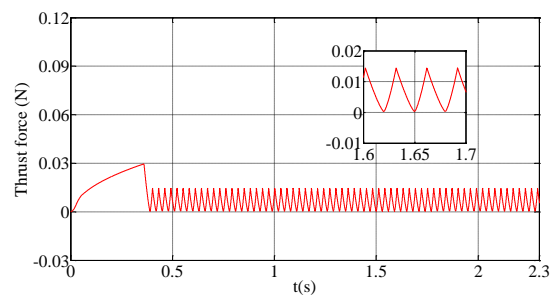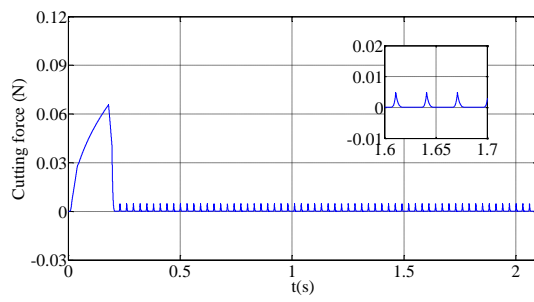
c2
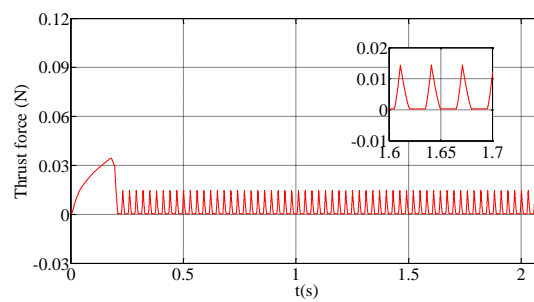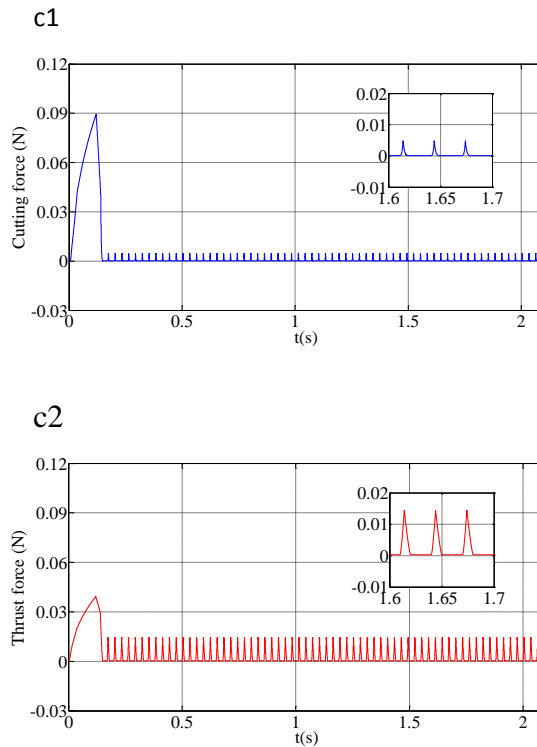
Fig. 5.6 Simulated cutting force with consideration of elastic recovery: (a) 0.5 mm/min, (b) 1 mm/min, (c) 1.5mm/min.

The simulation results show good agreement with the measured results. Firstly, Both the measured and simulated results show that the peak value of the main cutting force and the thrust force in the cutting phase linearly increase with the increase of feed rate, i.e. the increase of maximum cutting depth from 250 nm to 750 nm. Secondly, both the measured and simulated force in the rubbing face show the effect of elastic recovery as the forces are not equal to zero. Besides, the peak values, which correspond to the minimum chip thickness, of both the measured and simulated force in the rubbing phase show sudden drop when they are compared with the peak value in the cutting phase.

Some differences between the simulated and measured results are also observed. To begin with, the measured forces have a low frequency fluctuation that is less

than the spindle rotating frequency during the rubbing phase. This is due to the effect of the double high frequency vibration of the spindle. Then, According to the enlarged view of the main cutting force in the rubbing phase, the curve of the simulated force does not fit very well with the measured one. This means a more precise cutting force function is needed in the future to describe the cutting force when the uncut chip thickness is less than a certain value. Furthermore, as shown in Table 2, the measured peak value of the main cutting force in the cutting phase increases with the increase of feed rate at a slightly higher rate than the simulated one. This is result from the inaccuracy in the cutting coefficients obtained from the cutting tests.

5.4.3 Effect of elastic recovery on friction induced vibration

Under the same cutting conditions, another set of grooves was also machined with a slightly worn diamond cutting tool. The measured cutting forces are plotted in Fig. 5.7. The results show that the cutting process remains stable during the cutting phase, but then it becomes unstable during the rubbing phase. This unstable process is related to friction induced vibration. The slightly worn tool makes the tool edge radius larger and this makes the minimum chip thickness larger. Therefore, a larger portion of the material cannot be removed when the maximum cutting thickness denoted in Fig. 5.4 remains unchanged for the same feed rate. The unremoved material rubs against the cutting tool during the rubbing phase with larger friction and cutting force than for a new tool. A cutting process with a low feed rate will have more intense vibration as the cutting force in the rubbing phase is continuous, resulting in friction induced oscillation (Ibrahim 1994). This can be validated from the machined grooves

shown in Fig. 5.8 where there are vibration marks for feed rates of 0.5 and 1 mm/min, while tool marks cannot be observed for a feed rate of 1.5 mm/min, as the maximum cutting depth is larger than the other two feed rates.

a1

a2

b1

b2

c1

c2
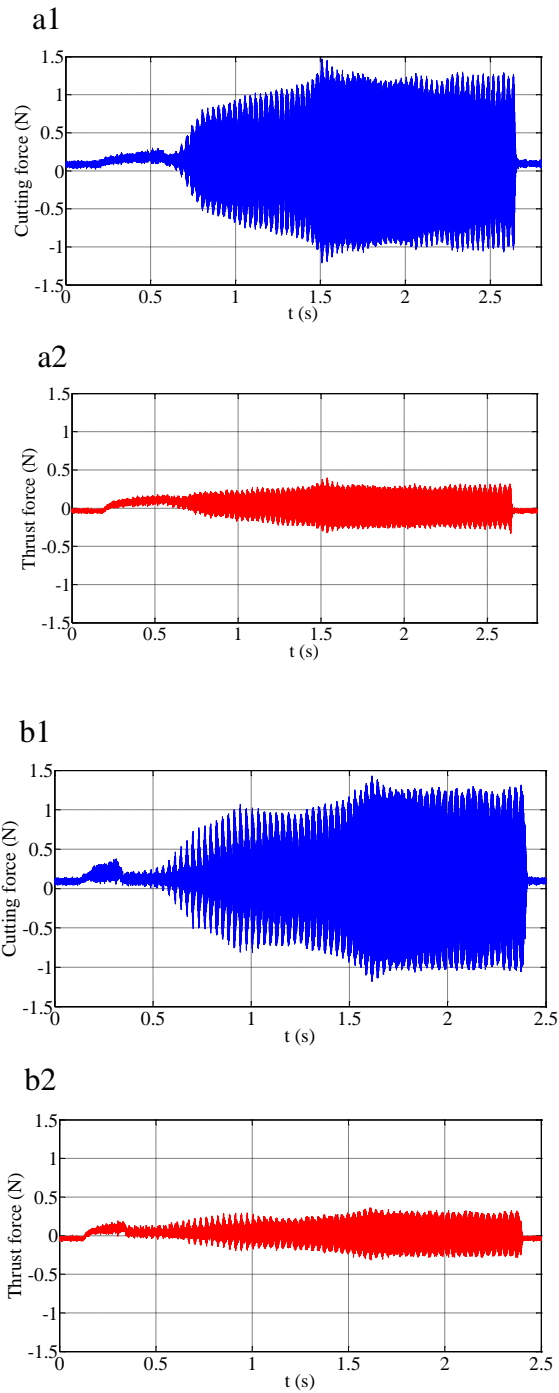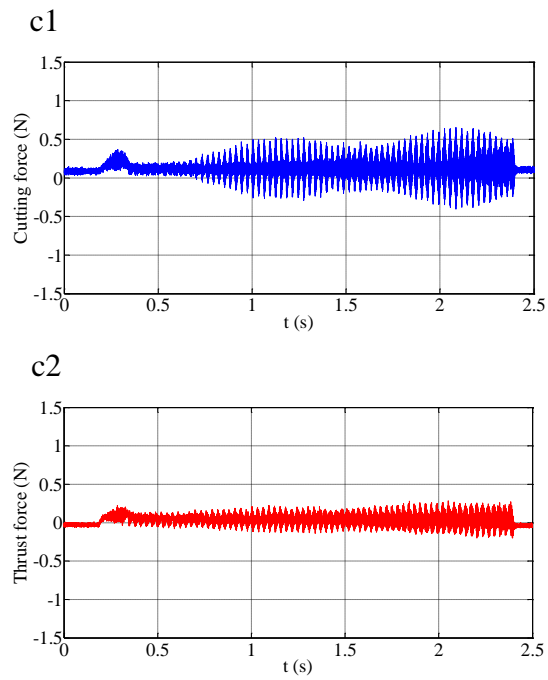
Fig. 5.7 Measured force in cutting process with slightly worn tool: (a) 0.5 mm/min, (b) 1 mm/min, (c) 1.5mm/min.
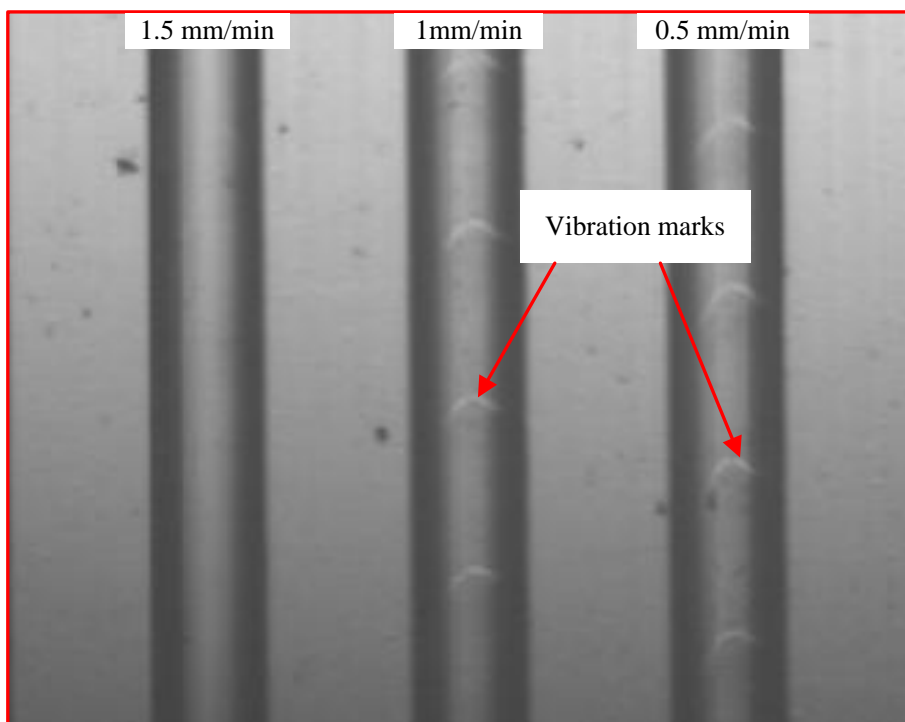
Fig. 5.8 The effect of vibration on machined grooves with different feed rate

5.5 Summary

In present study, a cutting force model considering the effect of tool edge radius is established in the ultra precision cylindrical diamond turning. The main conclusions are drawn as follows:

(1) The cutting force model for diamond turning can take into account the effect of tool edge radius based on the proposed relationship between the elastic recovery and uncut chip thickness, as well as the piecewise cutting force function.

(2) The simulated and experimental results reveal that the material cannot be entirely removed when the uncut chip thickness is less than the minimum chip thickness, whereas almost all the material can be removed when the uncut chip thickness is larger than a certain chip thickness.

(3) The upper limit of chip thickness for elastic recovery and minimum chip thickness can be estimated based on the measured cutting force of cutting groove on cylindrical surface by diamond turning.

(4) The micro cutting process with a slightly worn cutting tool is unstable because of friction induced vibration resulting from the severe friction and the larger tool edge radius which increase the minimum chip thickness and elastic recovery.

Chapter 6 Comprehensive model for dynamic surface generation

6.1 Introduction

In Chapter 5, an algorithm is established to compute the cutting force and simulate the surface topography in the micro cutting process, considering the minimum chip thickness and elastic recovery. In this chapter, a dynamic model for surface generation is developed, in which the spindle dynamics, the machining errors and the cutting mechanism are integrated. The spindle dynamics model and the cutting mechanism are discussed in Chapter 3 and Chapter 5 respectively. Thus, in this chapter only the machining error model is required to be established.

The error model is developed based on the multi-body kinematic method. The error model can take into account various errors such as straightness errors, position errors and squareness errors among the different axes. In addition, the spindle error motions can also be incorporated in this error model, and this allows the effect of spindle error motions on surface generation and cutting depth to be included in the comprehensive model. Finally, the dynamics of the cutting system can be solved by using the central difference method. Simulation verification is conducted to investigate the effect of the system dynamics on surface generation at different spindle speeds.

6.2 Modeling

6.2.1 Error modeling

6.2.1.1 Description of geometric errors

For a motion axis of a machine tool, the motion inaccuracy relative to the nominal motion can be described with six geometric errors: three translational errors and three angular errors. As shown in Fig. 6.1, the three translational errors can be represented with δ_x, δ_y and δ_z, and the angular errors are represented with ε_x, ε_y and ε_z, where the subscript are used to represent the related error direction. In a translational axis of a machine tool, these six geometric errors are one positioning error, two straightness errors and three angular errors, and all errors are position-dependent. The six errors for a rotational axis contains one axial error, two radial errors, one angular positional error and two tilt errors, and they are also dependent on the position.

In addition, the motion axis of the machine tool also has six location errors, which are independent of the motion of the axis. The most important location errors in a machine tool are squareness errors between different motion axes as shown in Fig. 6.2, and ε_{xy}, ε_{yz} and ε_{zx} are used to represent the squareness error between the X and Y axes, the squareness error between the Y and Z axes, and squareness error between X and Z axes respectively.
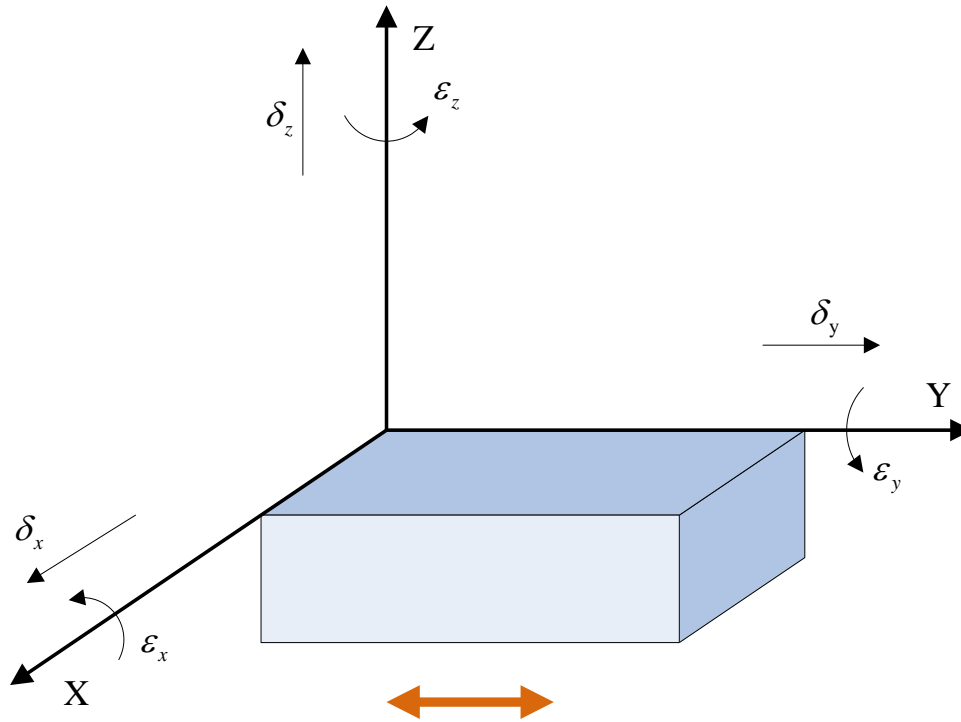
Fig. 6.1 Six geometric errors of motion axis
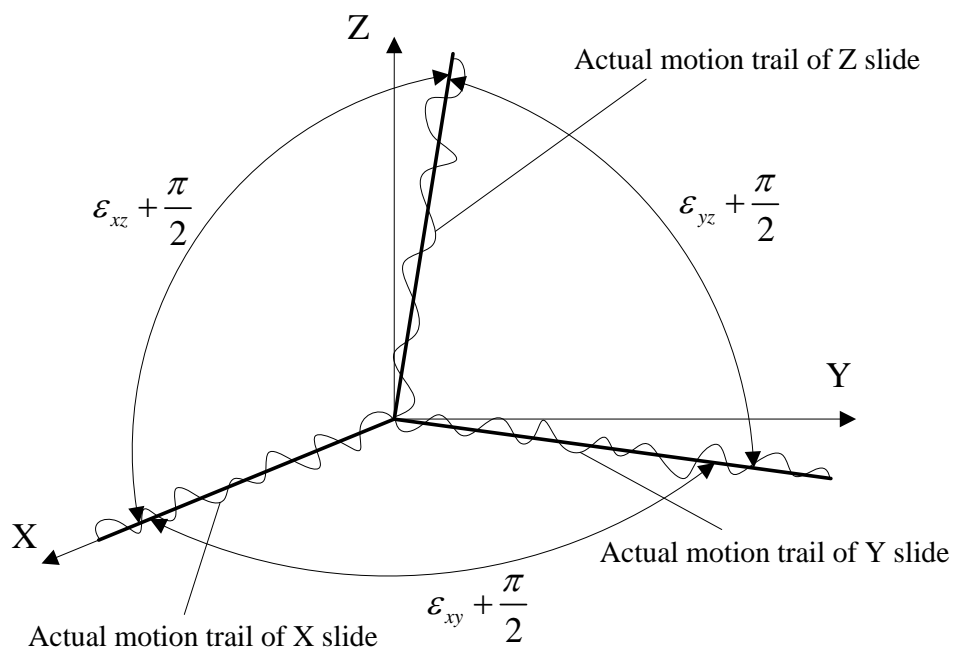
Fig. 6.2 Squareness errors

6.2.1.2 Error modeling for machine tools

If a homogeneous vector in a coordinate system CS1 needs to be represented in another coordinate system CS2, a general homogeneous transformation matrix is needed, and it has the following form:

$$T = \begin{bmatrix} \cos\alpha\cos\gamma & \sin\alpha\sin\beta\cos\gamma - \cos\alpha\sin\gamma & \cos\alpha\sin\beta\cos\gamma + \sin\alpha\sin\gamma & d_x \\ \cos\beta\sin\gamma & \sin\alpha\sin\beta\sin\gamma + \cos\alpha\cos\gamma & \cos\alpha\sin\beta\sin\gamma - \sin\alpha\cos\gamma & d_y \\ -\sin\beta & \sin\alpha\cos\beta & \cos\alpha\cos\beta & d_z \\ 0 & 0 & 0 & 1 \end{bmatrix}$$

(6.1)

where the CS1 can be obtained by rotating CS2 around its X, Y and Z axes with an angle α, β and γ respectively, and then translating CS2 along its X, Y and Z axes with a displacement d_x, d_y and d_z.
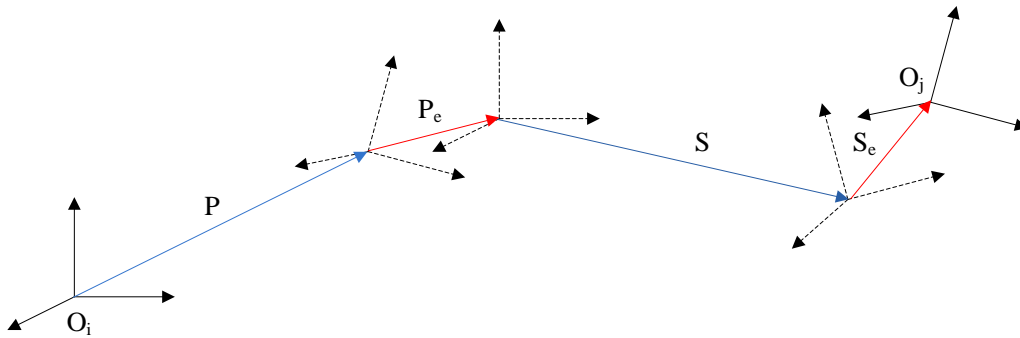
Fig. 6.3 Actual kinematics transformation

In a multi-body system, the actual position and orientation of a motion body j can be derived from the position and orientation of a body i with a transformation process as shown in Fig. 6.3. The transformation process contains four successive transformation matrixes: the initial position transformation matrix $_j^i T_P$,

the initial position error transformation matrix ${}^{i}_{j}T_{Pe}$, the ideal motion

transformation matrix ${}^{i}_{j}T_{S}$ and the error motion transformation matrix ${}^{i}_{j}T_{Se}$.

The integrated transformation matrix between body i and motion body j can be

obtained as:

$$\ {}^{i}_{j}T = {}^{i}_{j}T_{P}\ {}^{i}_{j}T_{Pe}\ {}^{i}_{j}T_{S}\ {}^{i}_{j}T_{Se} \tag{6.2}$$

Based on the assumption of a small angle and neglecting higher order terms, the

position error matrix and motion error matrix can be represented as follows:

$$\ {}^{i}_{j}T_{Pe} = \begin{bmatrix} 1 & -\varepsilon^{P}_{zij} & \varepsilon^{P}_{yij} & \delta^{P}_{xij} \\ \varepsilon^{P}_{zij} & 1 & -\varepsilon^{P}_{xij} & \delta^{P}_{yij} \\ -\varepsilon^{P}_{yij} & \varepsilon^{P}_{xij} & 1 & \delta^{P}_{zij} \\ 0 & 0 & 0 & 1 \end{bmatrix} \tag{6.3}$$

$$\ {}^{i}_{j}T_{Se} = \begin{bmatrix} 1 & -\varepsilon^{S}_{zij} & \varepsilon^{S}_{yij} & \delta^{S}_{xij} \\ \varepsilon^{S}_{zij} & 1 & -\varepsilon^{S}_{xij} & \delta^{S}_{yij} \\ -\varepsilon^{S}_{yij} & \varepsilon^{S}_{xij} & 1 & \delta^{S}_{zij} \\ 0 & 0 & 0 & 1 \end{bmatrix} \tag{6.4}$$

where δ^{P}_{xij}, δ^{P}_{yij} and δ^{P}_{zij} denote the initial translational position error along the

X, Y and Z axes; ε^{P}_{xij}, ε^{P}_{yij} and ε^{P}_{zij} denote the initial angular position error

around X, Y and Z axes; δ^{S}_{xij}, δ^{S}_{yij} and δ^{S}_{zij} denote the translational motion error

along X, Y and Z axes; and ε^{S}_{xij}, ε^{S}_{yij} and ε^{S}_{zij} denote the angular motion error

around X, Y and Z axes.

For an ultra-precision diamond tuning machine with a T-shape configuration as

shown in Fig. 6.4, it contains two translational motion axes. The spindle and the

tool are mounted on the X-axis and Z-axis respectively. O_{R} is the reference

coordinate system (CS). CS O_{1} and CS O_{T} are attached on the Z-axis motion

slide and tool holder respectively. CS O_2 and CS O_W are fixed on the X-axis motion slide and spindle respectively. The machine contains a workpiece-machine bed kinematics chain branch O_R-O_1-O_T and a tool-machine bed kinematics chain branch O_R-O_2-O_W. Fig. 6.5 shows the topological structure map of the diamond turning machine.
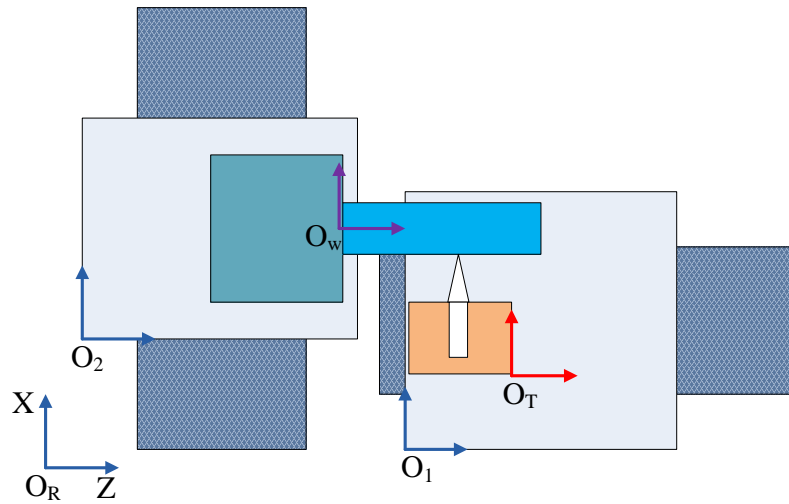
Fig. 6.4 Configuration of machine tool
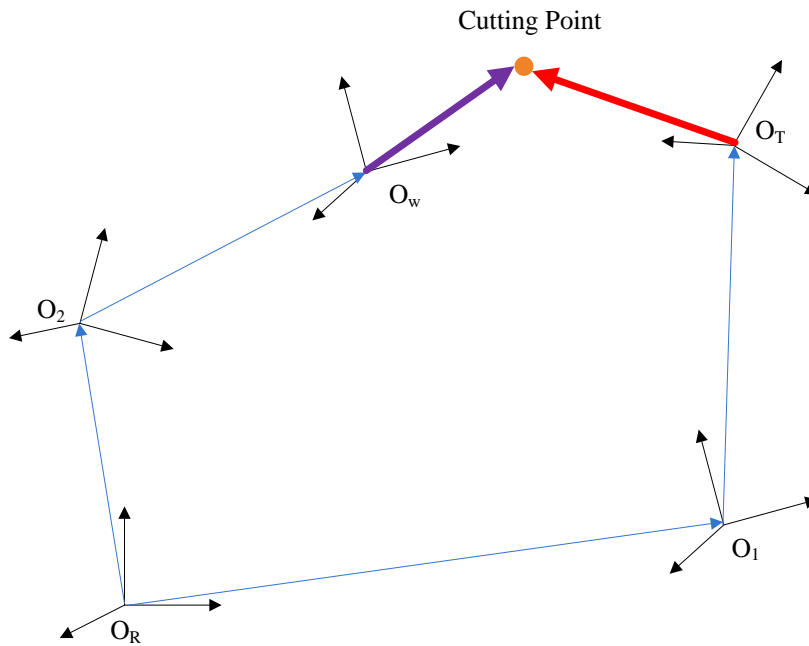
Fig. 6.5 Topologic structure map of machine tool

The homogeneous transformation matrix for representing the position and orientation of the Z-axis carriage in the reference coordinate system is described as follows:

$$ {}_1^R T = {}_1^R T_P \; {}_1^R T_{Pe} \; {}_1^R T_S \; {}_1^R T_{Se} \tag{6.5}$$

The initial position transformation matrix, initial position error transformation matrix, the ideal motion transformation matrix and the motion error transformation matrix of the Z-axis carriage are given as:

$$ {}_1^R T_P = \begin{bmatrix} 1 & 0 & 0 & d_{x1} \\ 0 & 1 & 0 & d_{y1} \\ 0 & 0 & 1 & d_{z1} \\ 0 & 0 & 0 & 1 \end{bmatrix} \tag{6.6a}$$

$$ {}_1^R T_{Pe} = \begin{bmatrix} 1 & 0 & \varepsilon_{XZ} & 0 \\ 0 & 1 & 0 & 0 \\ -\varepsilon_{XZ} & 0 & 1 & 0 \\ 0 & 0 & 0 & 1 \end{bmatrix} \tag{6.6b}$$

$$ {}_1^R T_S = \begin{bmatrix} 1 & 0 & 0 & 0 \\ 0 & 1 & 0 & 0 \\ 0 & 0 & 1 & z \\ 0 & 0 & 0 & 1 \end{bmatrix} \tag{6.6c}$$

$$ {}_1^R T_{Se} = \begin{bmatrix} 1 & -\varepsilon_z(z) & \varepsilon_y(z) & \delta_x(z) \\ \varepsilon_z(z) & 1 & -\varepsilon_x(z) & \delta_y(z) \\ -\varepsilon_y(z) & \varepsilon_x(z) & 1 & \delta_z(z) \\ 0 & 0 & 0 & 1 \end{bmatrix} \tag{6.6d}$$

where d_{x1}, d_{y1} and d_{z1} are the initial offsets between O_R and O_1; ε_{XZ} is the squareness error between the X-axis and Z-axis of the machine tool; $\delta_x(z)$, $\delta_y(z)$ and $\delta_z(z)$ are the horizontal, vertical straightness and position errors of

the Z-axis respectively; $\varepsilon_x(z)$, $\varepsilon_y(z)$ and $\varepsilon_z(z)$ are the pitch, yaw and roll errors of the Z-axis respectively.

The homogeneous transformation matrix for representing the position and orientation of CS O_T fixed on the tool holder with respect to the Z-axis carriage is described as follows:

$$
{}^1_T T = {}^1_T T_P \; {}^1_T T_{Pe} \; {}^1_T T_S \; {}^1_T T_{Se}
\tag{6.7}
$$

The initial position transformation matrix, the initial position error transformation matrix, the ideal motion transformation matrix and the motion error transformation matrix of the CS O_T are given as:

$$
{}^1_T T_P =
\begin{bmatrix}
1 & 0 & 0 & d_{xT} \\
0 & 1 & 0 & d_{yT} \\
0 & 0 & 1 & d_{zT} \\
0 & 0 & 0 & 1
\end{bmatrix}
\tag{6.8a}
$$

$$
{}^1_T T_{Pe} =
\begin{bmatrix}
1 & -\varepsilon_{zT} & \varepsilon_{yT} & \delta_{xT} \\
\varepsilon_{zT} & 1 & -\varepsilon_{xT} & \delta_{yT} \\
-\varepsilon_{yT} & \varepsilon_{xT} & 1 & \delta_{zT} \\
0 & 0 & 0 & 1
\end{bmatrix}
\tag{6.8b}
$$

$$
{}^1_T T_S =
\begin{bmatrix}
1 & 0 & 0 & 0 \\
0 & 1 & 0 & 0 \\
0 & 0 & 1 & 0 \\
0 & 0 & 0 & 1
\end{bmatrix}
\tag{6.8c}
$$

$$
{}^1_T T_{Se} =
\begin{bmatrix}
1 & 0 & 0 & 0 \\
0 & 1 & 0 & 0 \\
0 & 0 & 1 & 0 \\
0 & 0 & 0 & 1
\end{bmatrix}
\tag{6.8d}
$$

where d_{xT}, d_{yT} and d_{zT} are the initial offset between O_1 and O_T.

The homogeneous transformation matrix for representing the position and orientation of the X-axis carriage in the reference coordinate system is described as follows:

$$
{}_2^R T = {}_2^R T_P \, {}_2^R T_{Pe} \, {}_2^R T_S \, {}_2^R T_{Se} \tag{6.9}
$$

The initial position transformation matrix, initial position error transformation matrix, the ideal motion transformation matrix and the motion error transformation matrix of the X-axis carriage are given as:

$$
{}_2^R T_P =
\begin{bmatrix}
1 & 0 & 0 & d_{x2} \\
0 & 1 & 0 & d_{y2} \\
0 & 0 & 1 & d_{z2} \\
0 & 0 & 0 & 1
\end{bmatrix}
\tag{6.10a}
$$

$$
{}_2^R T_{Pe} =
\begin{bmatrix}
1 & 0 & 0 & 0 \\
0 & 1 & 0 & 0 \\
0 & 0 & 1 & 0 \\
0 & 0 & 0 & 1
\end{bmatrix}
\tag{6.10b}
$$

$$
{}_2^R T_S =
\begin{bmatrix}
1 & 0 & 0 & 0 \\
0 & 1 & 0 & 0 \\
0 & 0 & 1 & 0 \\
0 & 0 & 0 & 1
\end{bmatrix}
\tag{6.10c}
$$

$$
{}_2^R T_{Se} =
\begin{bmatrix}
1 & -\varepsilon_z(x) & \varepsilon_y(x) & \delta_x(x) \\
\varepsilon_z(x) & 1 & -\varepsilon_x(x) & \delta_y(x) \\
-\varepsilon_y(x) & \varepsilon_x(x) & 1 & \delta_z(x) \\
0 & 0 & 0 & 1
\end{bmatrix}
\tag{6.10d}
$$

where d_{x2}, d_{y2} and d_{z2} are the initial offsets between O_R and O_2; $\delta_x(x)$, $\delta_y(x)$ and $\delta_z(x)$ are the position, vertical and horizontal straightness errors of the X-axis respectively; $\varepsilon_x(x)$, $\varepsilon_y(x)$ and $\varepsilon_z(x)$ are the roll, yaw and pitch errors of the X-axis.

The homogeneous transformation matrix for representing the position and orientation of CS O_W fixed on the workpiece (spindle) with respect to the X-axis carriage is described as follows:

$$^2_W T = \, ^2_W T_P \, ^2_W T_{Pe} \, ^2_W T_S \, ^2_W T_{Se} \tag{6.11}$$

The initial position transformation matrix, initial position error transformation matrix, the ideal motion transformation matrix and the motion error transformation matrix of the CS O_W are given as:

$$^2_W T_P = \begin{bmatrix} 1 & 0 & 0 & d_{xW} \\ 0 & 1 & 0 & d_{yW} \\ 0 & 0 & 1 & d_{zW} \\ 0 & 0 & 0 & 1 \end{bmatrix} \tag{6.12a}$$

$$^2_W T_{Pe} = \begin{bmatrix} 1 & 0 & \varepsilon_{XW} & 0 \\ 0 & 1 & 0 & 0 \\ -\varepsilon_{XW} & 0 & 1 & 0 \\ 0 & 0 & 0 & 1 \end{bmatrix} \tag{6.12b}$$

$$^2_W T_S = \begin{bmatrix} \cos\theta & -\sin\theta & 0 & 0 \\ \sin\theta & \cos\theta & 0 & 0 \\ 0 & 0 & 1 & 0 \\ 0 & 0 & 0 & 1 \end{bmatrix} \tag{6.12c}$$

$$^2_W T_{Se} = \begin{bmatrix} 1 & -\varepsilon_z(\theta) & \varepsilon_y(\theta) & \delta_x(\theta) \\ \varepsilon_z(\theta) & 1 & -\varepsilon_x(\theta) & \delta_y(\theta) \\ -\varepsilon_y(\theta) & \varepsilon_x(\theta) & 1 & \delta_z(\theta) \\ 0 & 0 & 0 & 1 \end{bmatrix} \tag{6.12d}$$

where d_{xW}, d_{yW} and d_{zW} are the initial offsets between O_2 and O_T; ε_{XW} is the squareness error between the X-axis and the spindle center line of the machine tool; $\delta_x(\theta)$, $\delta_y(\theta)$ and $\delta_z(\theta)$ are the horizontal, vertical radial error motion and axial error of spindle respectively; $\varepsilon_x(\theta)$, $\varepsilon_y(\theta)$ and $\varepsilon_z(\theta)$ are the two tilt and rotating position errors of the spindle.

For the cutting point of the cutting tool, it can be represented as a vector in the CS O_T:

$$\vec{r} = [x_T, \quad y_T, \quad z_T]^T \tag{6.13}$$

This vector can be transformed to the workpiece coordinate system by multiplying by a homogeneous transformation matrix:

$$\vec{r}^W = {}_T^W T \square \vec{r} \tag{6.14}$$

where the homogeneous transformation matrix is given as follows:

$${}_T^W T = ({}_2^R T \, {}_W^2 T)^{-1} {}_1^R T \, {}_T^1 T \tag{6.15}$$

6.2.2 Integrated surface generation model

6.2.2.1 Description of the model

The spindle dynamics model, the surface and cutting force computing model and the error model of the machine tool have been established in Chapter 3, Chapter 4 and Section 5.2.1 of this chapter respectively. This makes it is possible to develop an integrated surface generation model which can consider both the spindle dynamics response in the cutting process and the error motion of the machine tool. Fig. 5.6 shows a schematic of the integrated surface generation model developed in this chapter. The ideal tool path locus used for machining is inputted with the integrated model to generate a surface by considering the spindle dynamics and error motion of the machine tool.
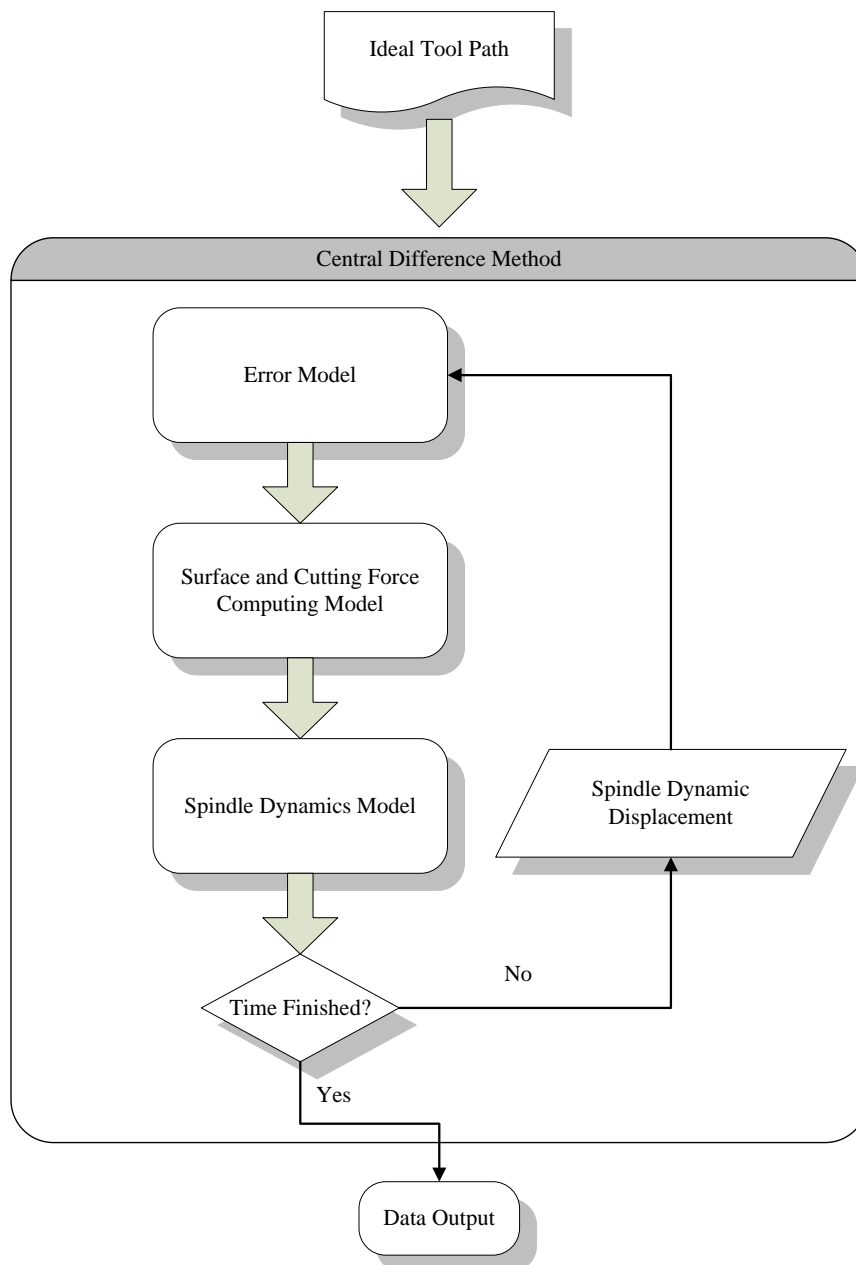
Fig. 6.6 Schematic of the integrated surface generation model

To calculate the spindle dynamics in the cutting process, the central difference method is adopted. At each time step, an ideal cutting point is firstly input to the error model to obtain the actual cutting point at the workpiece coordinate system. The actual cutting point determines the position of the cutting tool in the workpiece coordinate system, and the surface points of the workpiece and the cutting force at this time step are updated and calculated respectively by the

surface and cutting force computing model. The calculated cutting force is used as an input of the spindle dynamics model to calculate the motion of the spindle at the next time step. The calculated spindle motion, the ideal cutting point and the related error motion of the machine tool are prepared for computing at the next time step if the simulating process continues. When the simulation is finished, the simulated surface and the dynamic response of the system is the output.

6.2.2.2 Central difference method

The spindle motion equation is given as follow:

$$M\ddot{Q} + C\dot{Q} + KQ = F \qquad (6.16)$$

where M is the mass matrix of the spindle; C is the damping matrix of the spindle; K is the stiffness matrix of the spindle; Q is the displacement vector of the spindle; and F is the load matrix.

When the central difference method is adopted to calculate the spindle dynamic response, some initial conditions are firstly required:

$$\ddot{Q}_0 = M^{-1}(F_0 - C\dot{Q}_0 - KQ_0) \qquad (6.17a)$$

$$Q_{-1} = Q_0 - \Delta t\dot{Q}_0 + \frac{\Delta t^2}{2}\ddot{Q}_0 \qquad (6.17b)$$

The equivalent stiffness matrix used for the calculation is given as follows:

$$\widehat{K} = \frac{M}{\Delta t^2} + \frac{C}{2\Delta t} \qquad (6.18)$$

At each time step i, the equivalent load matrix is:

$$\widehat{F}_i = F_i - aQ_i - bQ_{i-1} \tag{6.19}$$

where

$$a = K - \frac{2M}{\Delta t^2} \tag{6.20}$$

$$b = \frac{M}{\Delta t^2} - \frac{C}{2\Delta t} \tag{6.21}$$

Based on the conditions given at the time step i, the spindle motion at the next time step $i+1$ can be obtained:

$$Q_{i+1} = \widehat{K}^{-1}\widehat{F}_i \tag{6.22}$$

Consequently, the velocity and acceleration of spindle at time step i can be obtained:

$$\dot{Q}_i = \frac{Q_{i+1} - Q_{i-1}}{2\Delta t} \tag{6.23}$$

$$\ddot{Q}_i = \frac{Q_{i+1} - 2Q_i + Q_{i-1}}{\Delta t^2} \tag{6.24}$$

To make the calculating process stable, the time step Δt must meet the following condition:

$$\Delta t \le \frac{T_n}{\pi} \tag{6.25}$$

where T_n is the minimum natural vibration period of the dynamics system.

6.3 Simulation and experimental results

A round diamond cutting tool with a nose radius of 0.25 mm, a spindle speed of 2000 rpm, a cutting depth of 1 μm and a feed rate of 5 μm/rev were used for the simulation. The cutting conditions for the experiment were also used as the input

of the simulation. The flow chart of the simulation process with consideration spindle dynamics is illustrated in Fig. 6.6. The simulation was realized by writing a Matlab programme based on the flow chart (refer to Appendix V). Fig. 6.7 shows the simulated ideal surface topography in cylindrical turning. In an ideal case, the ideal surface topography remains unchanged, no matter what the spindle speed is, and the surface topography is only dependent on the tool geometry. When the spindle dynamics is considered in the comprehensive dynamic surface generation model, the simulated surface at a spindle speed of 2000 rpm is shown in Fig. 6.8. As can be seen from Fig. 6.8, a set of stripes are generated on the surface. The width of the stripe is larger than the width of the ideal tool marks in each revolution. This can be attributed to the low frequency enveloping phenomenon resulting from the double frequency of the spindle discussed in Chapter 3.
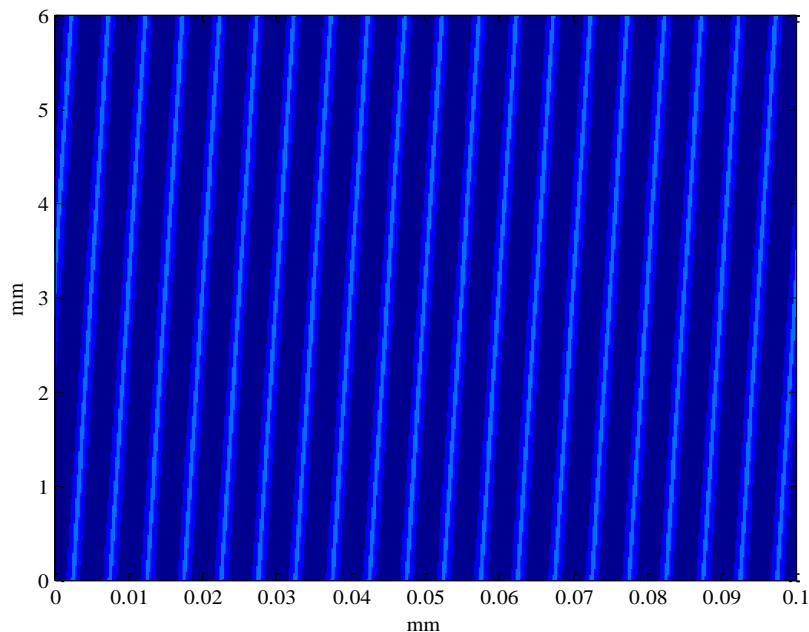
Fig. 6.7 Simulated ideal surface
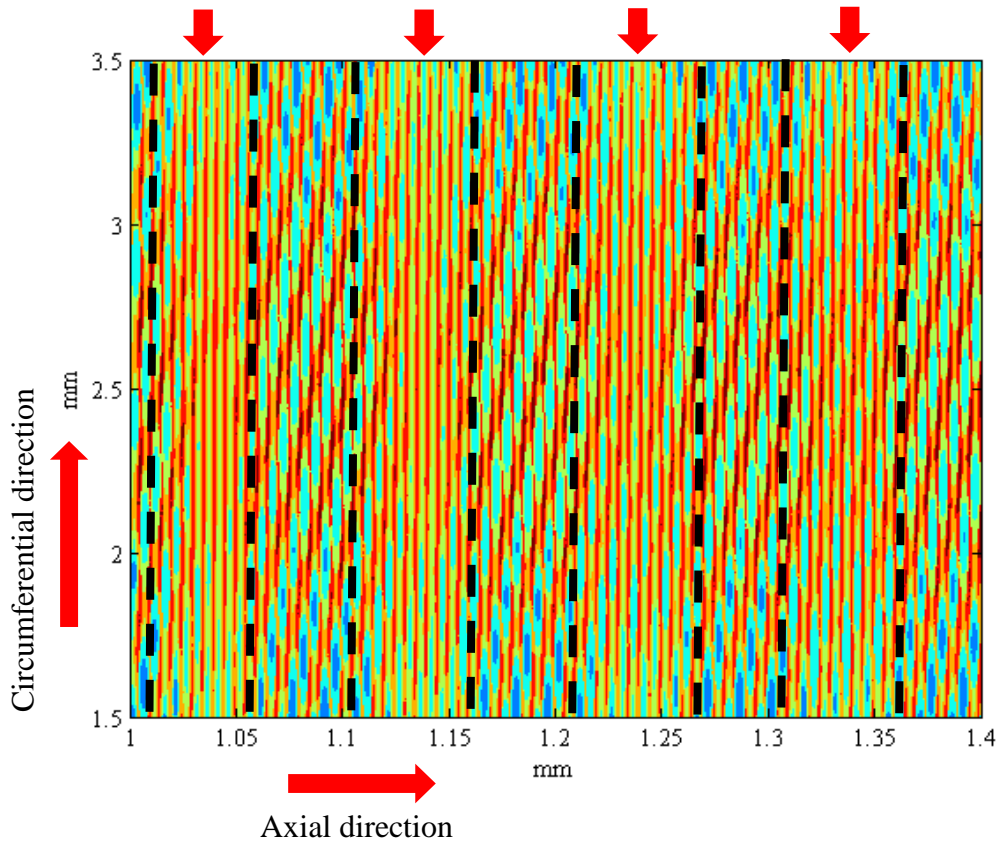
Fig. 6.8 Simulated surface by considering spindle dynamics

Two cylinder workpieces of aluminum and brass were machined with cylindrical turning and the machined cylindrical surfaces were measured with an optical measurement instrument (Zygo Nexview Optical Profiler). A spindle speed of 3200 rpm, feed rate of 5 μm/rev, cutting depth of 1 μm and tool nose radius of 0.25 mm were employed as the cutting conditions in the experiment. The measured surfaces are shown in Fig. 6.9, where stripes can be clearly observed on both two machined surfaces. The width of the stripes is also larger than the tool mark each revolution. This indicates that a low frequency component exists in the machined surface, and the frequency is lower than the spindle rotating frequency. The experimental results shows good agreement with the simulated surface shown in Fig. 6.8, and this indicates that the double frequency vibration of the spindle is a reasonable explanation for the generation of the stripes on a

machined surface. The stripes on the surface of the aluminum workpiece are clearer than on the machined brass surface. This is due to the material properties, including elastic recovery.
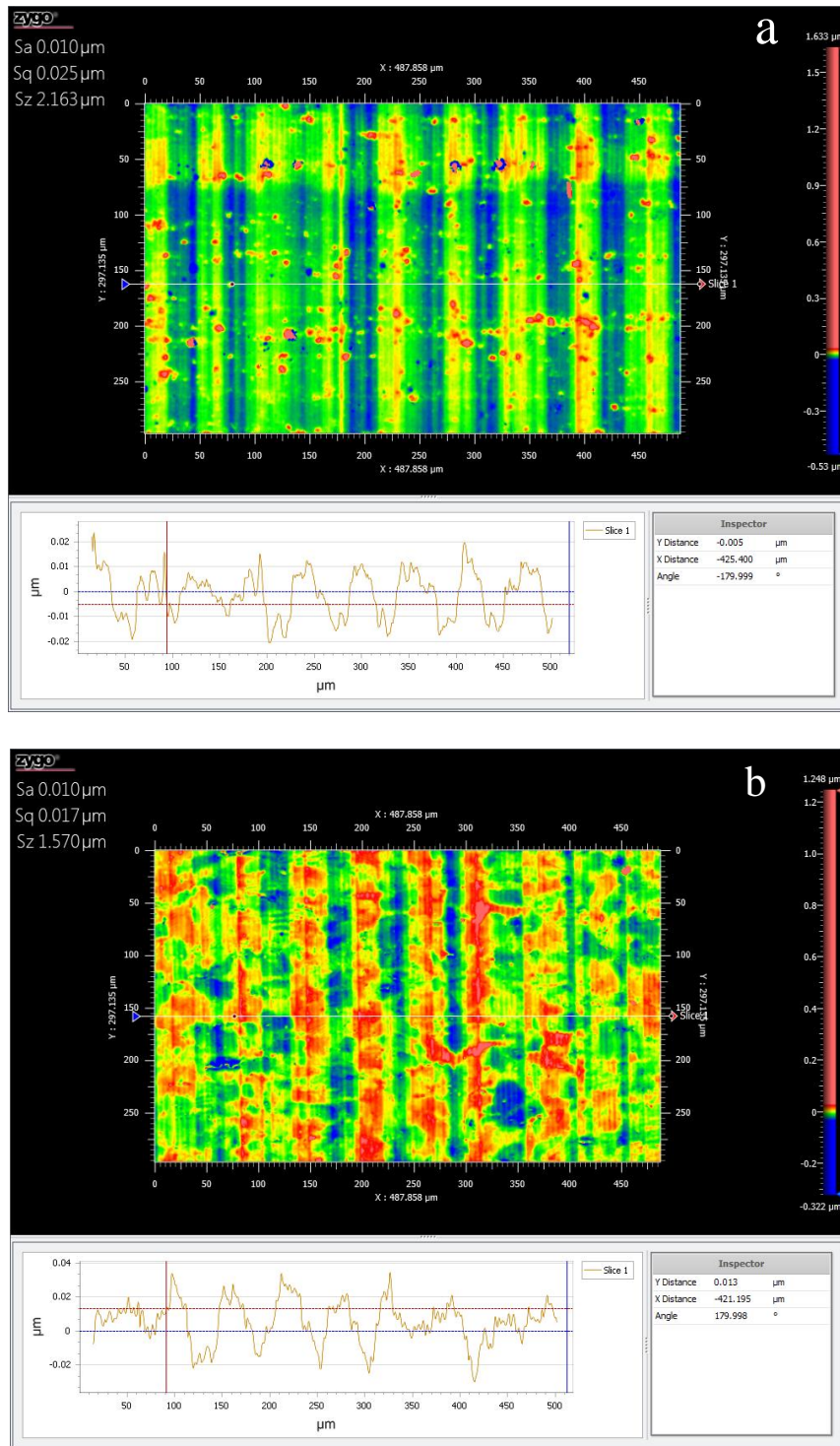
Fig. 6.9 Machined surface at spindle speed of 3200 rpm: a) Al, b) Brass

6.4 Summary

In this chapter, a comprehensive dynamic surface generation model is developed by considering the spindle dynamics. An error model is integrated to consider the machining errors, and the central difference method is utilized in the comprehensive model. The major conclusions can be drawn as follows:

(1) A comprehensive dynamic surface generation model considering the spindle dynamics, cutting mechanism and machining errors was developed to predict the surface topography in cylindrical turning process. Based on this model, stripes can be observed on the simulated surface. The stripes result from the low frequency enveloping phenomenon of the double frequency vibration of the spindle.

(2) The measured experimental results from the cylindrical turning experiment indicate that stripes with a width larger than the width of the tool marks of each revolution can be generated. This means that the machined surface topography contains a low frequency component, and the frequency is lower than the spindle rotating frequency.

Chapter 7 Overall conclusions and suggestions for future studies

7.1 Overall conclusions

Ultra-precision components are widely used in many industrial fields such as national defense, aerospace, astronomy and biomedical. These components usually have a form accuracy in the range of sub-micrometers and a surface roughness of several nanometers. Many machining techniques including ultra-precision diamond turning, ultra-precision micro milling, ultra-precision grinding, ultra-precision polishing, fast tool servo (FTS) and slow slide servo (S^3) have been developed to fabricate various symmetrical or non-symmetrical optical components with high accuracy, high surface quality and high efficiency. The quality of the machined surface is dependent on many factors such as the cutting condition (e.g. spindle speed, feed rate, cutting depth and tool nose radius), the relative vibration between the cutting tool and workpiece, the material properties (e.g. material swelling, pile-up and recovery), and tool wear.

The performance of the spindle is a vital factor in determining the surface quality in a machining process. Many techniques have been developed to measure the spindle error motions. These techniques can be divided into three categories, which are the reversal method, multi-probe method and multi-step method. They can be adopted to measure the ultra-precision spindle errors with sub-nanometer uncertainty. The measuring process is usually conducted using an artifact in the

air machining process. Therefore, the effect of the spindle dynamics in the actual machining process cannot be evaluated. In addition, some studies have developed a variety of models to predict the surface topography. These models considered the influences of many factors including tool geometry, spindle speed, cutting depth, tool shank deflection and measured vibration. However, few models have taken the spindle dynamics into account.

Motivated by the aforementioned problems, the study aims to investigate the effect of spindle dynamics on machining quality. A spindle dynamic model for an aerostatic bearing spindle is proposed to analyze the spindle characteristics by considering the spindle unbalance. This theoretical analysis is verified by conducting a series of groove cutting experiments on cylindrical surfaces. The cutting forces in the machining process and the machined groove are measured for analysis. To investigate the drift of the axis average line (AAL) of the spindle rotation axis due to hydrodynamic effect of the aerostatic bearing spindle and its effect on the microstructure, an experiment for fabrication of microstructures on a cylindrical surface with S^3 was also conducted. Moreover, to develop a dynamic model for surface generation by taking into account the spindle dynamics, an algorithm is firstly proposed to compute the cutting force and the generate surface profile, where the concept of minimum chip thickness and elastic recovery are considered, as the cutting depth is in the micrometer range. An error model is also proposed, which can take into account the spindle error motions and other machining errors. Finally, a comprehensive dynamic model for surface generation is proposed, where the spindle dynamics, the cutting mechanism and the machining error model are integrated.

The major findings and contributions are summarized as follows:

(1) A spindle dynamics model has been proposed for an aerostatic bearing. The model reveals that the spindle has a double frequency vibration under excitation, including spindle unbalance. These two frequencies are related to the forward and backward whirl mode induced by the gyroscopic effect. By using the FFT technique to analyze the simulated spindle dynamics response and the measured cutting force, the two frequencies can be identified.

(2) Based on the spiral groove cutting experiment, the depth of the machined spiral groove fluctuates along the axial direction of the workpiece with a relatively lower frequency than the rotational frequency of the aerostatic bearing (ABS). This results from the low frequency enveloping phenomenon induced by the double frequency vibration of the spindle. The experimental results are consistent with the simulation results.

(3) The spindle unbalance induced eccentricity has a significant effect on the machining accuracy in ultra-precision diamond turning process, even though it has a small amplitude. This can be identified in the groove cutting experiments. The amplitude of the eccentricity is dependent on the spindle speed. Nonetheless, the diameter of the machined cylindrical workpiece remains unchanged with different spindle speeds.

(4) The mean value of the depth of the machined groove on the circumference changes with different spindle speeds. This is due to the variation of the relative distance between the AAL of the spindle rotation axis and the tool tip at different spindle speeds. The hydrodynamic effect of the ABS essentially contributes to the variation.

(5) An experiment for the fabrication of microstructures with slow slide servo (S^3) machining was designed and conducted to investigate the effect of the hydrodynamic effect of the ABS on the drift of AAL of the spindle rotation axis at different spindle speeds.

(6) The analysis based on the proposed error model reveals that the cutting depth error during the S^3 machining process is mainly dependent on the spindle error motion, the positioning error of the X-axis slide and the drift of AAL of the spindle rotation axis. If the S^3 machining is conducted in a short time period, the thermal effect can be neglected.

(7) In the S^3 machining experiment, the amplitude of the machined microstructures on the circumference fluctuates. This is due to the effect of the spindle error motions, including unbalance induced eccentricity. On the other hand, the amplitude of the microstructures remain almost unchanged and only has a variation of few tens nanometers, thereby excluding the thermal effect on the machining error.

(8) The drift of AAL of the spindle rotation axis increases with the increase of the spindle speed. As a consequence, the amplitude of the microstructure will increase in S^3 machining. Based on the measurement results, the drift with spindle speed is repeatable. It increases at a high rate at low spindle speed, with a low rate at high spindle speed. This indicates that the drift of AAL of the spindle rotation axis with spindle speed is nonlinear.

(9) An algorithm for surface generation and cutting force in ultra-precision cylindrical cutting process was developed by considering the minimum chip thickness and elastic recovery. At each time step, the cutting force with varying cutting depth along the cutting tool edge can be calculated by searching the

surface points swept by the cutting tool. The effect of the minimum chip thickness and elastic recovery in the preceding cutting step can be considered in the current machining step by updating the surface points. This algorithm is an important part in constructing the dynamic surface generation model.

(10) The simulated and experimental results verify that the workpiece material cannot be removed until the cutting depth is larger than the minimum chip thickness.

(11) A worn cutting tool can make the micro cutting process unstable due to severe friction and larger tool edge radius which can increase the minimum chip thickness. Thus, friction induced vibration may occur.

(12) A dynamic surface generation model was developed, which takes into account the spindle dynamics, machining errors and cutting mechanism. This model can be used to predict and optimize the surface topography in ultra-precision diamond turning process.

(13) The simulation and experiment results indicate that the double frequency vibration of ASB has a significant effect on the surface topography in the cylindrical turning process. When the feed rate of each revolution remains unchanged, the surface topography is dependent on the spindle speed.

7.2 Suggestions for future work

The dynamic spindle error motions and their effect in the ultra-precision machining process have been studied with theoretical and experimental approaches. Some dynamic spindle error motions, including unbalance induced eccentricity, double frequency vibration and drift of AAL of the spindle rotation axis have been identified with simulation and experimental methods. A dynamic

surface generation model considering the spindle dynamics, cutting mechanism and machining errors has been proposed. However, how to precisely measure the dynamic spindle error motion and reduce its effect on the machining quality has not been addressed in this thesis. The following are some suggestions for further studies to improve the machining quality in ultra-precision machining:

(1) To measure the unbalance induced eccentricity with an on-line method.

In the present study, the effect of unbalance induced eccentricity on form error has been investigated by conducting groove cutting and S^3 machining. The results indicate that the eccentricity error motion makes a significant contribution to form accuracy in ultra-precision machining, even though the amplitudes are in the range of several tens nanometer. One method to reduce the effect of eccentricity is to have a well balancing operation. Nonetheless, to entirely eliminate the unbalance is difficult. Thus, an on-line measurement method can be developed to measure the eccentricity and compensate for it.

(2) To measure and compensate the drift of AAL of spindle rotation axis.

In the present study, the drift of AAL of the spindle rotation axis with spindle speed due to the hydrodynamic effect of the aerostatic bearing has been investigated. The effect of this drift can have a dramatic effect when multi-spindle-speed machining is employed. For instance, in the fabrication of microstructures, a high spindle speed is used for finish turning while a slow spindle speed is adopted for the S^3 machining process, where the finish surface is used as the benchmark for the S^3 machining process. As the displacement of drift is different for different spindle speeds, the actual cutting depth is not equal to its

nominal value in the S^3 machining process. In addition, the studies reported in this thesis also reveal that the drift of the spindle rotation axis with spindle speed is a nonlinear process. To improve the machining accuracy, it is necessary to measure and compensate for the drift.

(3) To characterize the dynamic behavior of ABS and optimize the machining parameters in ultra-precision machining.

The dynamic behavior of the spindle can affect the machining dynamics. The present studies reveal that ASB can have a double frequency vibration under excitation such as spindle unbalance and cutting force. The simulation and experimental results indicate that the effect of the double frequency vibration on surface topography has a tight relationship with the spindle speed. As such, it is critical to characterize the dynamics of the spindle in ultra-precision machining. An effective technique should be proposed to obtain better understanding of the spindle dynamics. Most studies reveal that the spindle dynamics can be affected by the spindle speed. Therefore, a technique for characterization of the spindle dynamics should be applied at different spindle speeds. Frequency response functions (FRF) are suggested for representing the spindle dynamics. Based on FRF, the effect of spindle dynamics on the machining dynamics can be evaluated and the cutting parameters can be optimized.

Appendices

Appendix Ⅰ　　Form Talysurf PGI 1240 Freeform Profiler
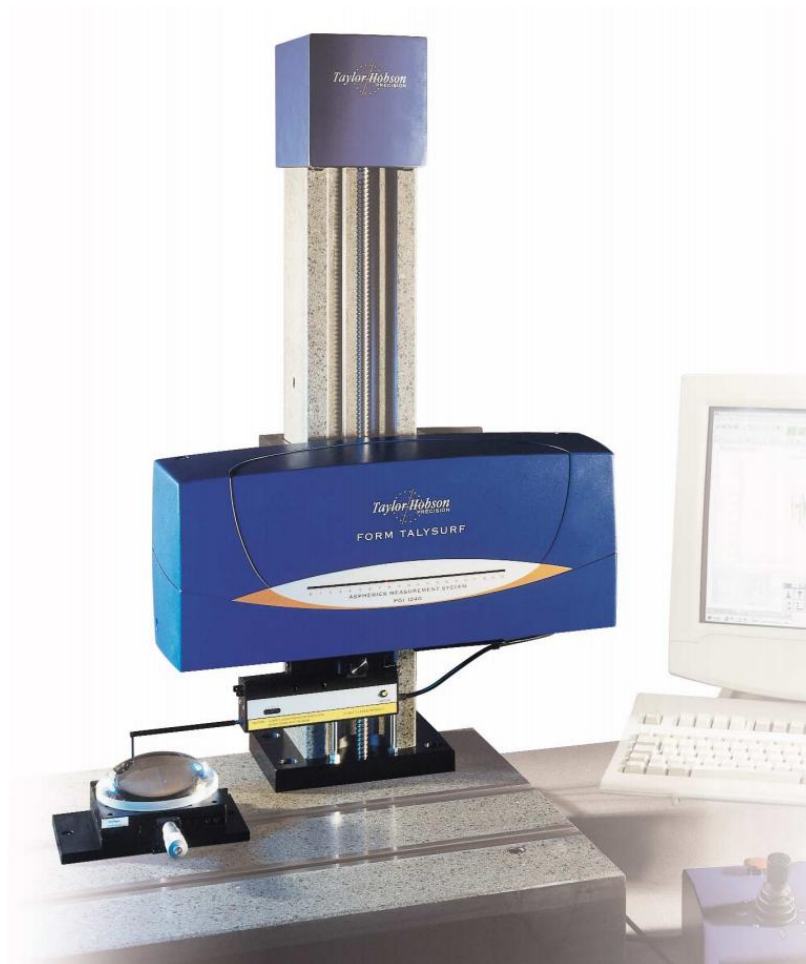
The Form Talysurf PGI 1240 from Taylor Hobson is a contact stylus measurement instrument, and can be used to measure the small to medium sized aspheric optics components. The typical applications contain: Cameras, Mobile

phones, Projection systems, Contact lens molds and Flat panel displays etc. The critical features of this instrument are as follows:

a) The horizontal traverse is 200 mm with a straightness of 0.11 μm\200 mm;

b) The vertical measuring range is 12.5 mm with a 0.8 nm vertical resolution;

c) A Gauge range of 50 mm is possible with special styli;

d) 1 nm RMS noise floor provides market-leading optics surface finish measurement capability;

e) Extensive range of optional accessories, including styli for demanding applications

Cited from:

http://www.azooptics.com/optics-equipment-details.aspx?EquipID=628

Appendix Ⅱ　Zygo Nexview Optical Profiler
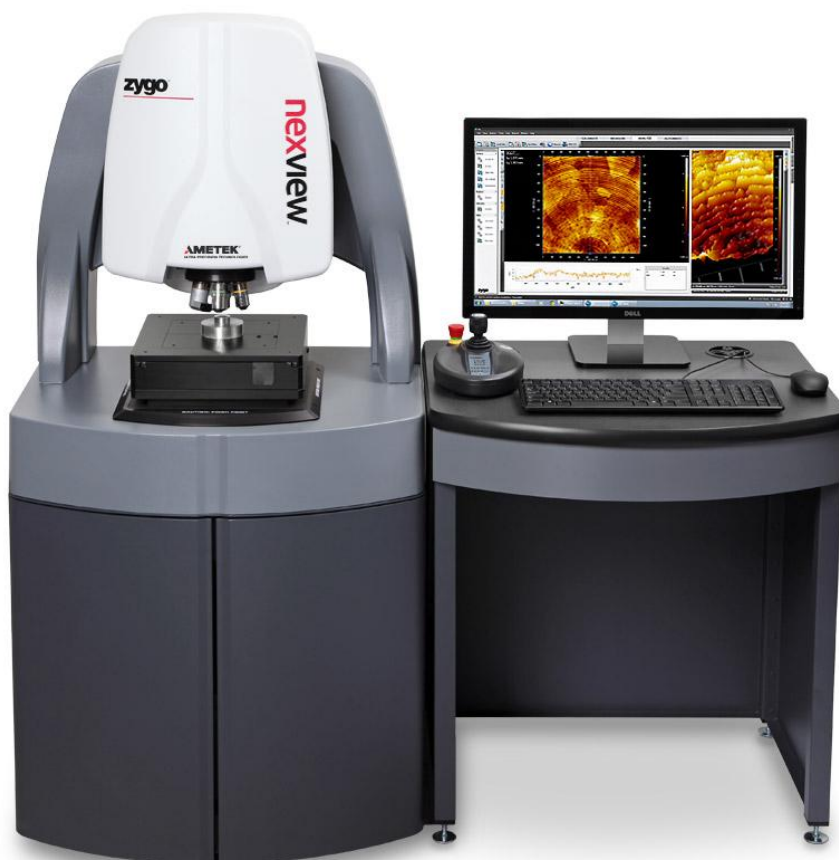
Nexview 3D optical surface profiler can measure many types of surfaces including fatness, roughness, large steps and segments, thin films, and steep slopes. The feature height range is from sub-nanometer up to 20 mm. The key features summarized as follows:

a) Capable of measuring various surfaces from rough to super smooth;

b) A STR (Surface Topography Repeatability) of 0.08 nm;

c) CSI (coherence scanning interferometry) and PSI (phase shifting interferometry) technology;

d) Automated X/Y/Z stage;

e) ISO 25178 surface measurement parameters

f) Robust operation due to high tolerance for vibration;

g) More powerful and user-friendly software.

Cited from:

http://www.zygo.com/?/met/profilers/nexview/

Appendix Ⅲ　Nanotech 350FG ultra-precision machine

The Moor Nanotech 350FG is a 4-axis computer controlled ultra-precision machine. This ultra-precision machine is capable of machining a variety of surfaces including aspheric and toroidal axisymmetric surface, freeform surfaces machined with slow tool servo machining and raster flycutting. The key features are:

a) 0.01 nanometer linear/0.0000001° rotary programming resolution;

b) 500 mm diameter $\times 300$ mm long workpiece capacity;

c) 350 mm travel on X-axis, 300 mm travel on Z-axis and 150 mm travel on Y-axis;

d) 0.034 nanometer feedback resolution for linear axis;

c) 0.3μm over full travel straightness for X- and Z- axis, and 0.5μm over full travel straightness for Y-axis in critical direction;

d) ±0.5°F temperature control for workholding spindle;

e) Spindle axial and radial motion accuracy are ≤ 12.5 nanometers;

f) Oil hydrostatic bearing linear axis and groove compensated air bearing spindle;

g) ± 1.0 arc seconds positioning accuracy and 0.07 arc seconds feedback resolution for C-axis.

Cited from:

http://www.nanotechsys.com/wp-content/uploads/file/PDFs/Nanotech%20350FG%20Specifications%20-%20Rev_0812.pdf

Appendix Ⅳ Nanoform 200 ultra-precision machine

The Nanoform 200 is a two-axis computer controlled diamond turning machine. Its two linear axis are equipped with hydrostatic oil bearing while an aerostatic, slot-type thrust bearing is utilized for the spindle. The fast & slow tool servo, oil hydrostatic rotary B-axis and grinding spindle are optional. The key features of this machine are:

a) 190 mm travel range for X and Z axis;

b) 0.2 μm/full travel horizontal straightness and 0.5 μm/full travel vertical straightness for X and Z axis;

c) Air or water cooling for spindle thermal control;

d) Axial/radial spindle motion accuracy ≤ 50 nm;

e) Slot-type thrust bearing for spindle;

f) The spindle is driven by integral DC brushless motor with 1000 a line encoder.

Cited from:

https://www.google.com.hk/url?sa=t&rct=j&q=&esrc=s&source=web&cd=1&ve

d=0ahUKEwjvkJmOv73JAhWE46YKHSjuDDEQFggfMAA&url=http%3A%2F

%2Fwww.sterlingint.com%2Fdocs%2FNanoformEngSpec.doc&usg=AFQjCNH

UxrYx9jKRL4BVt6nMlafNPbHMZg

Appendix Ⅴ Program for surface generation

Function[PolarR,Ft,Fc]=

Force_PointCloud(PolarR,Tw,Xt_actual,Del_rad,Del_z,Za,Zb,rt,StepNumber)

[m,n]=size(PolarR);%%

if mod(StepNumber,m)==0;

    Index_Theta=m-1;

else

    Index_Theta=mod(StepNumber,m)-1;

End

Tw(1)=Index_Theta*Del_rad;

if Za<=Tw(3) && Tw(3)<=Zb;

   Index_Z=round((Tw(3)-Za)/Del_z);

else

   Index_Z=-1

   Tw(3)

end

Tw(3)=Index_Z*Del_z+Za;

%Xt_actual=Tw(2)+X_vib;

```
  if Index_Theta==m;

          Index_Theta=0;

  end


if Index_Z>=n;

          Index_Z=n-1;

end


SemiWidth=rt*0.3;

SearchRange=2*floor(SemiWidth/Del_z);

Search_Lowerlimit=(Index_Z+1)-SearchRange/2;

Search_Upperlimit=(Index_Z+1)+SearchRange/2;


if Search_Lowerlimit<1;

    Search_Lowerlimit=1;

end


if Search_Upperlimit>n;

    Search_Upperlimit=n;

end


Number_Cut=zeros(1,n);

for j=Search_Lowerlimit:Search_Upperlimit;
```

```
Point_GivenTheta=PolarR(Index_Theta+1,j);

P1=[Xt_actual+rt,Tw(3)];

P2=[Point_GivenTheta,Za+(j-1)*Del_z];

Distance=norm(P1-P2);


if Distance<rt;

    Number_Cut(j)=1;

end


end


tip_location=0;

update_location=0;

update_value=0;

TTC=0;


PolarR_Copy=PolarR(Index_Theta+1,:);

PolarR_Empty=zeros(1,n);

for j=Search_Lowerlimit:Search_Upperlimit;

    if   Number_Cut(j)==1;

        k=Intersection(Del_z,Index_Z,Za,Xt_actual,j-1,rt,PolarR_Copy);

        [X_update,           Index_update,           ft(j),fc(j),

ttc]=CalulateNewValue_V3(PolarR_Empty,PolarR_Copy,k-1,j-1,Index_Z,Del_z,

rt,Xt_actual,Za);
```

```
        [PolarR_Empty]=RecordNewValue(          PolarR_Empty,X_update,

Index_update, Index_Z);

            if (j-1)==Index_Z;

                tip_location=Index_Z;

                update_location= Index_update;

                update_value=X_update;

                TTC=ttc;

            end

    else

        ft(j)=0;

        fc(j)=0;

    end

end


[ PolarR(Index_Theta+1,:) ]=UpdateValue( PolarR_Empty,Number_Cut,PolarR_

Copy,Index_Z,Del_z,rt,Xt_actual);


Ft=sum(ft);

Fc=sum(fc);


end


function[k]=Intersection(Increment_z,index_Ztip,Z_low,xt,index_Zcurrent,rt,Pol

arR_Copy1 )

%UNTITLED Summary of this function goes here
```

```
%       Detailed explanation goes here


Z_tip=Z_low+Increment_z*index_Ztip;

Z_current=Z_low+index_Zcurrent*Increment_z;

d=abs(Z_current-Z_tip);

hight=sqrt(rt^2-d^2);

tanLine=d/hight;

SinLine=d/rt;

if SinLine<0 || SinLine>1;

     Error=1

end


if Z_tip>Z_current;

     f=index_Ztip-index_Zcurrent;

     for p=1:f;

          h1=p*Increment_z/tanLine;


          x1=xt+rt-h1;

          ab1=x1-PolarR_Copy1(index_Ztip+1-p);


          abs1=abs(ab1);

          A(p)=abs1;

     end


     [v,j]=min(A);
```

```
    k=index_Ztip+1-j;

elseif Z_tip<Z_current;

    f=index_Zcurrent-index_Ztip;

    for p=1:f;

        h1=p*Increment_z/tanLine;

        x1=xt+rt-h1;

        ab1=x1-PolarR_Copy1(index_Ztip+1+p);

        abs1=abs(ab1);

        A(p)=abs1;

    end

    [v,j]=min(A);

    k=index_Ztip+1+j;

elseif Z_tip==Z_current;

    k=index_Ztip+1;

end

end


function   [polarR_Empty]   =   RecordNewValue(   polarR_Empty,x_update,

index_update, index_tip )

%UNTITLED Summary of this function goes here

%    Detailed explanation goes here

v_update=index_update+1;

v_tip=index_tip+1;

L=length(polarR_Empty);
```

```
if v_update==v_tip;

    polarR_Empty(v_update)=x_update;

elseif v_update<v_tip;

    status_needUpdate=1;

    for g=(v_update+1):v_tip;

        if   polarR_Empty(g)>0;

            status_needUpdate=0;

        end

    end


    if status_needUpdate==1;

        polarR_Empty(v_update)=x_update;

    end


elseif v_update>v_tip;

    polarR_Empty(v_update)=x_update;

    for g=(v_update+1):L

        if polarR_Empty(g)>0;

            polarR_Empty(g)=0;

        end

    end
end
end
```

```
function[polarR_updated]=

UpdateValue( polarR_Empty,number_Cut,polarR_copy,index_tip,del_z,rt1,xt )

%UNTITLED2 Summary of this function goes here

%    Detailed explanation goes here

L_cut=length(number_Cut);

%Sum_cut=sum(number_Cut);


p=0;

q=0;

Sa(1)=0;

Sb(1)=0;

for g=1:L_cut;


if(g==1&&number_Cut(g)==1)||(g~=1&&number_Cut(g)-number_Cut(g-1)==1

)||(g==L_cut && number_Cut(g)-number_Cut(g-1)==1);

        p=p+1;

        Sa(p)=g;

    end


    if g==L_cut &&    number_Cut(g)==1;

        q=q+1;

        Sb(q)=g;

    elseif g~=1 && number_Cut(g)-number_Cut(g-1)==-1;

        q=q+1;

        Sb(q)=g-1;
```

```
        end

end


if length(Sa)~=length(Sb);

    error=1

end


L_Sa=length(Sa);

for g=1:L_Sa;

    u=Sa(g);

    v=Sb(g);

    if u==0;

            break;

    end


    if polarR_Empty(u)==0;

        dd=del_z*abs(index_tip+1-u);

        hig=sqrt(rt1^2-dd^2);

        x_u=xt+rt1-hig;

        polarR_Empty(u)= x_u;

    end


    if polarR_Empty(v)==0;

        dd=del_z*abs(index_tip+1-v);

        hig=sqrt(rt1^2-dd^2);
```

```matlab
        x_v=xt+rt1-hig;

        polarR_Empty(v)= x_v;

    end


    for c=u:v;

        if polarR_Empty(c)==0;

            for d=c:v;

                if polarR_Empty(d)>0;

                    value_up=polarR_Empty(d);

                    indx_up=d;

                    break;

                end

            end

            tan_k=(value_up-polarR_Empty(c-1))/((indx_up-c+1)*del_z);

            polarR_Empty(c)=tan_k*del_z+polarR_Empty(c-1);

        end

    end


end %%



for g=1:L_cut;

    if number_Cut(g)==1;

        polarR_copy(g)=polarR_Empty(g);

    end
```

```
end
```

```
polarR_updated=polarR_copy;
```

```
end
```

References

Abouelatta O B, Madl J., "Surface roughness prediction based on cutting parameters and tool vibrations in turning operations", Journal of materials processing technology, 118(1), 269-277 (2001).

Altintaş Y, Lee P., "A general mechanics and dynamics model for helical end mills", CIRP Annals-Manufacturing Technology, 45(1), 59-64 (1996).

Altintas Y, Woronko A., "A piezo tool actuator for precision turning of hardened shafts. CIRP Annals-Manufacturing Technology", 51(1), 303-306 (2002).

Arizmendi M, Fernández J, de Lacalle L N L, et al., "Model development for the prediction of surface topography generated by ball-end mills taking into account the tool parallel axis offset", Experimental validation. CIRP Annals-Manufacturing Technology, 57(1), 101-104 (2008).

Arizmendi M, Campa F J, Fernández J, et al., "Model for surface topography prediction in peripheral milling considering tool vibration", CIRP Annals-Manufacturing Technology, 58(1), 93-96 (2009).

Anandan K P, Ozdoganlar O B., "An LDV-based methodology for measuring axial and radial error motions when using miniature ultra-high-speed (UHS) micromachining spindles", Precision Engineering, 37(1), 172-186 (2013).

Anandan K P, Ozdoganlar O B., "Analysis of error motions of ultra-high-speed (UHS) micromachining spindles", International Journal of Machine Tools and Manufacture, 70, 1-14 (2013).

Anandan K P, Ozdoganlar O B., "A multi-orientation error separation technique for spindle metrology of miniature ultra-high-speed spindles", Precision Engineering, 40, 119-131 (2015).

An C H, Zhang Y, Xu Q, et al., "Modeling of dynamic characteristic of the aerostatic bearing spindle in an ultra-precision fly cutting machine", International Journal of Machine Tools and Manufacture, 50(4), 374-385 (2010).

ANSI/ASME B89.3.4M, 1985. Axes of rotation: methods for specifying and testing; 1985.

Balsamo A., Marques D., & Sartori S., "A method for thermal-deformation corrections of CMMs", CIRP Annals-Manufacturing Technology, 39(1), 557-560 (1990).

Bediz B., Gozen B. A., Korkmaz E., Ozdoganlar O. B., "Dynamics of ultra-high-speed (UHS) spindles used for micromachining", International Journal of Machine Tools & Manufacture, 87, 27–38 (2014).

Beekhuis B. L., Brinksmeier E., Garbrecht M., & Sölter J., "Improving the shape quality of bearing rings in soft turning by using a Fast Tool Servo", Production Engineering, 3(4-5), 469-474 (2009).

Beekhuis B., Stöbener D., Brinksmeier E., & Goch G., "Compensation of part distortion in soft-turning of bearing rings", Materialwissenschaft und Werkstofftechnik, 43(1-2), 42-47 (2012).

Bringmann B., & Knapp W., "Model-based 'chase-the-ball' calibration of a 5-axes machining center", CIRP Annals-Manufacturing Technology, 55(1), 531-5342006).

Bringmann B., & Knapp W., "Machine tool calibration: Geometric test uncertainty depends on machine tool performance", Precision Engineering, 33(4), 524-529 (2009).

Bringmann B., & Maglie P. "A method for direct evaluation of the dynamic 3D path accuracy of NC machine tools", CIRP Annals-Manufacturing Technology, 58(1), 343-346 (2009).

Brinksmeier E, Riemer O, Gläbe R, et al., "Submicron functional surfaces generated by diamond machining", CIRP Annals-Manufacturing Technology, 59(1), 535-538 (2010).

Bryan J. B., "A simple method for testing measuring machines and machine tools Part 1: Principles and applications", Precision Engineering, 4(2), 61-69 (1982a).

Bryan J. B., "A simple method for testing measuring machines and machine tools Part 2: Construction details", Precision Engineering, 4(3), 125-138 (1982b).

Cappa S, Reynaerts D, Al-Bender F., "A sub-nanometre spindle error motion separation technique", Precision Engineering, 38(3), 458-471 (2014).

Chapman M. A., "Limitations of laser diagonal measurements", Precision Engineering, 27(4), 401-406 (2003).

Chen C H, Kang Y, Yang D W, et al., "Influence of the number of feeding holes on the performances of aerostatic bearings", Industrial lubrication and Tribology, 62(3), 150-160 (2010).

Chen G., Yuan J., & Ni J., "A displacement measurement approach for machine geometric error assessment" International Journal of Machine Tools and Manufacture, 41(1), 149-161 (2001).

Chen J S, Hsu W Y., "Characterizations and models for the thermal growth of a motorized high speed spindle", International Journal of Machine Tools and Manufacture, 43(11), 1163-1170 (2003).

Chen M Q, Yang C H., "Dynamic compensation technology of the spindle error motion of a precision lathe", Precision Engineering, 11(3), 135-138 (1989).

Cheung C. F., Lee W. B., "A theoretical and experimental investigation of surface roughness formation in ultra-precision diamond turning", International Journal of Machine Tools and Manufacture, 40(7), 979-1002 (2000).

Cheung C. F., Lee W. B., "Characterisation of nanosurface generation in single-point diamond turning", International Journal of Machine Tools and Manufacture, 41(6), 851-875 (2001).

Cheng M. N., Cheung C. F., Lee W. B., et al., "Theoretical and experimental analysis of nano-surface generation in ultra-precision raster milling", International Journal of Machine Tools and Manufacture, 48(10), 1090-1102 (2008).

Devitt D., "Axis of rotation metrology", Bearing Specialists Association, 1-7(2009).

Donaldson R.R., "A simple method for separating the spindle error from test ball roundness error", CIRP Annals, 21(1), 125–6 (1972).

Donaldson R. R., Patterson S. R., "Design and construction of a large, vertical axis diamond turning machine", 27th Annual Techincal Symposium, International Society for Optics and Photonics, 62-67 (1983).

Donmez M. A., Blomquist D. S., Hocken R. J., Liu C. R., & Barash M. M., "A general methodology for machine tool accuracy enhancement by error compensation", Precision Engineering, 8(4), 187-196 (1986).

Ehmann K. F., Hong M. S., "A generalized model of the surface generation process in metal cutting", CIRP Annals-Manufacturing Technology, 43(1), 483-486 (1994).

Elfizy A. T., Bone G. M., Elbestawi M. A., "Design and control of a dual-stage feed drive", International Journal of Machine Tools and Manufacture, 45(2), 153-165 (2005).

Estler W. T., "Calibration and use of optical straightedges in the metrology of precision machines", Optical Engineering, 24(3), 243372-243372 (1985).

Estler W. T., Evans C. J., Shao L. Z., "Uncertainty estimation for multiposition form error metrology", Precision Engineering, 21(2), 72-82 (1997).

Evans C. J., Hocken R. J., Estler W. T., "Self-calibration: reversal, redundancy, error separation, and 'absolute testing'", CIRP Annals-Manufacturing Technology, 45(2), 617-634 (1996).

Fang F. Z., Zhang X. D., Hu X. T., "Cylindrical coordinate machining of optical freeform surfaces", Optics Express, 16(10), 7323-7329 (2008).

Fang N., "Slip-line modeling of machining with a rounded-edge tool—Part I: new model and theory", Journal of the Mechanics and Physics of Solids, 51(4), 715-742 (2003).

Filiz S., Ozdoganlar O. B., "A three-dimensional model for the dynamics of micro-endmills including bending, torsional and axial vibrations", Precision Engineering, 35, 24–37 (2011).

Fujimaki K., Mitsui K., "Radial error measuring device based on auto-collimation for miniature ultra-high-speed spindles", International Journal of Machine Tools and Manufacture, 47(11), 1677-1685 (2007).

Gao W., Kiyono S., Nomura T., "A new multiprobe method of roundness measurements", Precision Engineering, 19(1), 37-45 (1996).

Gao W., Kiyono S., Sugawara T., "High-accuracy roundness measurement by a new error separation method", Precision engineering, 21(2), 123-133 (1997a).

Gao W., Kiyono S., "On-machine roundness measurement of cylindrical workpieces by the combined three-point method", Measurement, 21(4), 147-156 (1997b).

Gao W., Kiyono S., Satoh E., et al., "Precision measurement of multi-degree-of-freedom spindle errors using two-dimensional slope sensors", CIRP Annals-Manufacturing Technology, 51(1), 447-450 (2002).

Gao W., Araki T., Kiyono S., et al., "Precision nano-fabrication and evaluation of a large area sinusoidal grid surface for a surface encoder", Precision Engineering, 27(3), 289-298 (2003).

Gao W., Arai Y., Shibuya A., Kiyono S., & Park C. H., "Measurement of multi-degree-of-freedom error motions of a precision linear air-bearing stage", Precision engineering, 30(1), 96-103 (2006).

Gao W., Tano M., Araki T., et al., "Measurement and compensation of error motions of a diamond turning machine", Precision engineering, 31(3), 310-316 (2007).

Grejda R., Marsh E., Vallance R., "Techniques for calibrating spindles with nanometer error motion", Precision Engineering, 29(1), 113-123 (2005).

Guo P., Ehmann K.F., "An analysis of the surface generation mechanics of the elliptical vibration texturing process", International Journal of Machine Tools and Manufacture, 64, 85-95 (2013).

Hosseini S.A.A., Zamanian M., Shams Sh., Shooshtari A., "Vibration analysis of geometrically nonlinear spinning beams", Mechanism and Machine Theory, 78, 15–35 (2014).

Huang P., Lee W. B., Chan C. Y., "Investigation of the effects of spindle unbalance induced error motion on machining accuracy in ultra-precision diamond turning", International Journal of Machine Tools and Manufacture, 94, 48-56 (2015).

Ibaraki S., Oyama C., & Otsubo H., "Construction of an error map of rotary axes on a five-axis machining center by static R-test", International Journal of Machine Tools and Manufacture, 51(3), 190-200 (2011).

Ibrahim R. A., "Friction-induced vibration, chatter, squeal, and chaos—part II: Dynamics and modeling", Applied Mechanics Reviews, 47(7), 227-253 (1994).

Ikawa N., Donaldson R. R., Komanduri R., et al., "Ultraprecision metal cutting—the past, the present and the future", CIRP Annals-Manufacturing Technology, 40(2), 587-594 (1991).

ISO 230-7:2006. "Test code for machine tools—Part 7: geometric accuracy of axes of rotation", (2006).

Jang D. Y., Choi Y. G., Kim H. G., et al., "Study of the correlation between surface roughness and cutting vibrations to develop an on-line roughness measuring technique in hard turning", International Journal of Machine Tools and Manufacture, 36(4), 453-464 (1996).

Kakino Y., Ihara Y., Nakatsu Y., & Okamura K., "The measurement of motion errors of NC machine tools and diagnosis of their origins by using telescoping magnetic ball bar method", CIRP Annals-Manufacturing Technology, 36(1), 377-380 (1987).

Kango S., Singh D., Sharma R. K., "Numerical investigation on the influence of surface texture on the performance of hydrodynamic journal bearing", Meccanica, 47(2), 469-482 (2012).

Khanfir H., Bonis M., Revel P., "Improving waviness in ultra precision turning by optimizing the dynamic behavior of a spindle with magnetic bearings", International Journal of Machine Tools and Manufacture, 45(7), 841-848 (2005).

Kim H. S., Kim E. J., "Feed-forward control of fast tool servo for real-time correction of spindle error in diamond turning of flat surfaces", International Journal of Machine Tools and Manufacture, 43(12), 1177-1183 (2003).

Kim H. S., Kim E. J., Song B. S., "Diamond turning of large off-axis aspheric mirrors using a fast tool servo with on-machine measurement", Journal of Materials Processing Technology, 146(3), 349-355 (2004).

Knapp B., Arneson D., "Dynamic Characterization of a Micro-machining Spindle", 9th international conference on micromanufacturing, (2014).

Knapp W., & Matthias E., "Test of the three-dimensional uncertainty of machine tools and measuring machines and its relation to the machine errors", CIRP Annals-Manufacturing Technology, 32(1), 459-464 (1983).

Knapp W., & Weikert S., "Testing the contouring performance in 6 degrees of freedom", CIRP Annals-Manufacturing Technology, 48(1), 433-436 (1999).

Kong L. B., Cheung C. F., Jiang X. Q., et al., "Characterization of surface generation of optical microstructures using a pattern and feature parametric analysis method", Precision Engineering, 34(4), 755-766 (2010).

Kong L. B., Cheung C. F., "Prediction of surface generation in ultra-precision raster milling of optical freeform surfaces using an integrated kinematics error model", Advances in Engineering Software, 45(1), 124-136 (2012).

Kunzmann H., Trapet E., & Wäldele F., "A uniform concept for calibration, acceptance test, and periodic inspection of coordinate measuring machines using

reference objects", CIRP Annals-Manufacturing Technology, 39(1), 561-564 (1990).

Lee J. C., Gao W., Shimizu Y., et al., "Spindle error motion measurement of a large precision roll lathe", International Journal of Precision Engineering and Manufacturing, 13(6), 861-867 (2012).

Lee J. C., Shimizu Y., Gao W., et al., "Precision evaluation of surface form error of a large-scale roll workpiece on a drum roll lathe", Precision Engineering, 38(4), 839-848 (2014).

Lee K. I., Lee D. M., & Yang S. H., "Parametric modeling and estimation of geometric errors for a rotary axis using double ball-bar", The International Journal of Advanced Manufacturing Technology, 62(5-8), 741-750 (2012).

Lee W. B., Cheung C. F., Chiu W. M., et al., "An investigation of residual form error compensation in the ultra-precision machining of aspheric surfaces", Journal of Materials Processing Technology, 99(1), 129-134 (2000).

Lin S. C., Chang M. F., "A study on the effects of vibrations on the surface finish using a surface topography simulation model for turning", International Journal of Machine Tools and Manufacture, 38(7), 763-782 (1998).

Liu C. H., Jywe W. Y., Lee H. W., "Development of a simple test device for spindle error measurement using a position sensitive detector", Measurement Science and Technology, 15(9), 1733 (2004).

Liu C. H., Jywe W. Y., Shyu L. H., & Chen C. J., "Application of a diffraction grating and position sensitive detectors to the measurement of error motion and angular indexing of an indexing table", Precision engineering, 29(4), 440-448 (2005).

Liu Q., Zhou X., Wang L., "A new hybrid macro-and micro-range fast tool servo", Mechanic Automation and Control Engineering (MACE), 2010 International Conference on. IEEE, 3124-3127 (2010).

Liu X., Jun M. B. G., DeVor R. E., et al., "Cutting mechanisms and their influence on dynamic forces, vibrations and stability in micro-endmilling", ASME 2004 International Mechanical Engineering Congress and Exposition, American Society of Mechanical Engineers, 583-592 (2004).

Liu X., DeVor R. E., Kapoor S. G., "Model-based analysis of the surface generation in microendmilling—Part I: model development", Journal of manufacturing science and engineering, 129(3), 453-460 (2007a).

Liu X., DeVor R. E., Kapoor S. G., "Model-based analysis of the surface generation in microendmilling—part II: experimental validation and analysis", Journal of manufacturing science and engineering, 129(3), 461-469 (2007b).

Liu Y. T., Li B. J., "Precision positioning device using the combined piezo-VCM actuator with frictional constraint", Precision Engineering, 34(3), 534-545 (2010).

Ludwick S. J., Chargin D. A., Calzaretta J. A., et al., "Design of a rotary fast tool servo for ophthalmic lens fabrication", Precision Engineering, 23(4), 253-259 (1999).

Lu X., Jamalian A., "A new method for characterizing axis of rotation radial error motion: Part 1. Two-dimensional radial error motion theory", Precision engineering, 35(1), 73-94 (2011).

Lu X., Jamalian A., Graetz R., "A new method for characterizing axis of rotation radial error motion: Part 2. Experimental results", Precision Engineering, 35(1), 95-107 (2011).

Lu X. D., Trumper D. L., "Ultrafast tool servos for diamond turning", CIRP Annals-Manufacturing Technology, 54(1), 383-388 (2005).

Lv Y.J., Zhang Y.F., Yu L., Liu H., "Analysis of dynamic characteristics of hydrodynamic journal bearing-Rotor system (in Chinese)", Lubrication Engineering, 3, 6-9 (2004).

Ma H., Hu D., Zhang K., "A fast tool feeding mechanism using piezoelectric actuators in noncircular turning", The International Journal of Advanced Manufacturing Technology, 27(3-4), 254-259 (2005).

Marsh E., Arneson D. A., Van Doren M. J., et al., "The effects of spindle dynamics on precision flycutting", Proceedings of the American society for precision engineering 2005 annual meeting, (2005).

Marsh E., Couey J., Vallance R., "Nanometer-level comparison of three spindle error motion separation techniques", Journal of manufacturing science and engineering, 128(1), 180-187 (2006).

Marsh E. R., Arneson D. A., Martin D. L., "A comparison of reversal and multiprobe error separation", Precision engineering, 34(1), 85-91 (2010).

Martin D. L., Tabenkin A. N., Parsons F. G., "Precision spindle and bearing error analysis", International Journal of Machine Tools and Manufacture, 35(2), 187-193 (1995).

Matta P., Arghir M., Bonneau O., "Experimental analysis of cylindrical air-bearing dynamic coefficients", Tribology Transactions, 53(3), 329-339 (2010).

Meinel A. B., Meinel M. P., Stacy J. E., et al., "Wave-front correctors by diamond turning. Applied optics", 25(6), 824 (1986).

Mekid S., Ogedengbe T., "A review of machine tool accuracy enhancement through error compensation in serial and parallel kinematic machines", International Journal of Precision Technology, 1(3-4), 251-286 (2010).

Merchant M. E., "Mechanics of the metal cutting process. II. Plasticity conditions in orthogonal cutting", Journal of applied physics, 16(6), 318-324 (1945).

Montgomery D., Altintas Y., "Mechanism of cutting force and surface generation in dynamic milling", Journal of Manufacturing Science and Engineering, 113(2), 160-168 (1991).

Murakami H., Kawagoishi N., Kondo E., et al., "Optical technique to measure five-degree-of-freedom error motions for a high-speed microspindle", International Journal of Precision Engineering and Manufacturing, 11(6), 845-850 (2010).

Murakami H., Katsuki A., Sajima T., "Simple and simultaneous measurement of five-degrees-of-freedom error motions of high-speed microspindle: Error analysis", Precision Engineering, 38(2), 249-256 (2014).

Nakkiew W., Lin C. W., Tu J. F., "A new method to quantify radial error of a motorized end-milling cutter/spindle system at very high speed rotations", International Journal of Machine Tools and Manufacture, 46(7), 877-889 (2006).

Ni J., "CNC Machine Accuracy Enhancement Through Real-Time Error Compensation", Journal of Manufacturing Science and Engineering, 119(4B), 717-725 (1997).

Ohishi S., Matsuzaki Y., "Experimental investigation of air spindle unit thermal characteristics", Precision engineering, 26(1), 49-57 (2002).

Omar O., El-Wardany T., Ng E., et al., "An improved cutting force and surface topography prediction model in end milling", International Journal of Machine Tools and Manufacture, 47(7), 1263-1275 (2007).

Pahk H. J., Kim Y. S., & Moon J. H., "A new technique for volumetric error assessment of CNC machine tools incorporating ball bar measurement and 3D volumetric error model", International Journal of Machine Tools and Manufacture, 37(11), 1583-1596 (1997).

Patterson S. R., Magrab E. B., "Design and testing of a fast tool servo for diamond turning", Precision Engineering, 7(3), 123-128 (1985).

Ramesh R., Mannan M. A., & Poo A. N., "Error compensation in machine tools—a review: Part I: geometric, cutting-force induced and fixture-dependent errors", International Journal of Machine Tools and Manufacture, 40(9), 1235-1256 (2000).

Schellekens P., Rosielle N., Vermeulen H., Vermeulen M. M. P. A., Wetzels S. F. C. L., & Pril W., "Design for precision: current status and trends", CIRP Annals-Manufacturing Technology, 47(2), 557-586 (1998).

Sartori S., & Zhang G. X., "Geometric error measurement and compensation of machines", CIRP Annals-Manufacturing Technology, 44(2), 599-609 (1995).

Sastry S., Kapoor S. G., DeVor R. E., "Compensation of progressive radial run-out in face-milling by spindle speed variation", International Journal of Machine Tools and Manufacture, 40(8), 1121-1139 (2000).

Schwenke H., Franke M., Hannaford J., & Kunzmann H., "Error mapping of CMMs and machine tools by a single tracking interferometer", CIRP Annals-Manufacturing Technology, 54(1), 475-478 (2005).

Schwenke H., Knapp W., Haitjema H., Weckenmann A., Schmitt R., & Delbressine F., "Geometric error measurement and compensation of machines—an update", CIRP Annals-Manufacturing Technology, 57(2), 660-675 (2008).

Soons J. A., Theuws F. C., & Schellekens P. H., "Modeling the errors of multi-axis machines: a general methodology", Precision Engineering, 14(1), 5-19 (1992).

Srinivasa N., Ziegert J. C., Mize C. D., "Spindle thermal drift measurement using the laser ball bar", Precision Engineering, 18(2), 118-128 (1996).

Stoebener D., & Dijkman M., "An ultrasound in-process-measuring system to ensure a minimum roundness deviation for rings during turning", CIRP Annals-Manufacturing Technology, 56(1), 513-516 (2007).

Sze-Wei G., Han-Seok L., Rahman M., & Watt F., "A fine tool servo system for global position error compensation for a miniature ultra-precision lathe", International Journal of Machine Tools and Manufacture, 47(7), 1302-1310 (2007).

Tala-Ighil N., Fillon M., Maspeyrot P., "Effect of textured area on the performances of a hydrodynamic journal bearing", Tribology International, 44(3), 211-219 (2011).

Tauhiduzzaman M., Yip A., Veldhuis S. C., "Form error in diamond turning", Precision Engineering, 42, 22–36 (2015).

Tohme Y., "Principles and Applications of the Slow Slide Servo", http://www.nanotechsys.com/technology/technical-papers/, (2004).

Tong S., "Two-step method without harmonics suppression in error separation", Measurement Science and Technology, 7(11), 1563 (1996).

Trapet E., & Wäldele F., "A reference object based method to determine the parametric error components of coordinate measuring machines and machine tools", Measurement, 9(1), 17-22 (1991).

Trapet E., Martín J. J. A., Yagüe J. A., Spaan H., & Zelený V., "Self-centering probes with parallel kinematics to verify machine-tools", Precision Engineering, 30(2), 165-179 (2006).

Trumper D. L., and Lu X., "Fast tool servos: advances in precision, acceleration, and bandwidth", Towards Synthesis of Micro-/Nano-systems, Springer, London, 11-19 (2007).

Tsutsumi M., & Saito A., "Identification and compensation of systematic deviations particular to 5-axis machining centers", International Journal of Machine Tools and Manufacture, 43(8), 771-780 (2003).

Tu J. F., Bossmanns B., Hung S. C. C., "Modeling and error analysis for assessing spindle radial error motions", Precision engineering, 21(2), 90-101(1997).

Umetsu K., Furutnani R., Osawa S., Takatsuji T., & Kurosawa T., "Geometric calibration of a coordinate measuring machine using a laser tracking system", Measurement science and technology, 16(12), 2466 (2005).

Wang H., Yang S., "Design and control of a fast tool servo used in noncircular piston turning process", Mechanical Systems and Signal Processing, 36(1), 87-94 (2013).

Wang S. B., Geng L., Zhang Y. F., et al., "Cutting force prediction for five-axis ball-end milling considering cutter vibrations and run-out", International Journal of Mechanical Sciences, 96, 206-215 (2015).

Wang S. J., To S., Cheung C. F., "Effect of workpiece material on surface roughness in ultraprecision raster milling", Materials and Manufacturing Processes, 27(10), 1022-1028 (2012).

Weck M., Oezmeral H., Mehlkopp K., Terwei T., "A New Hybrid Concept for a Long Stroke Fast Tool Servo System", Proceedings of ASPE 1995 Annual Meeting, 211–214 (1995).

Weikert S., "R-test, a new device for accuracy measurements on five axis machine tools", CIRP Annals-Manufacturing Technology, 53(1), 429-432 (2004).

Whitehouse D. J., "Some theoretical aspects of error separation techniques in surface metrology", Journal of Physics E: Scientific Instruments, 9(7), 531 (1976).

Wu D., Chen K., Wang X., "Tracking control and active disturbance rejection with application to noncircular machining", International Journal of Machine Tools and Manufacture, 47(15), 2207-2217 (2007).

Yang S. H., Kim K. H., Park Y. K., "Measurement of spindle thermal errors in machine tool using hemispherical ball bar test", International Journal of Machine Tools and Manufacture, 44(2), 333-340 (2004).

Yang Z.Y., Zhang D.W., Huang T., Wu J., "Kinematic stability and critical velocity of a high-speed painting automizor with gas bearing support (in Chinese)", Journal of Tianjin University, 37 (11), 980-984 (2004).

Yin Z. Q., Dai Y. F., Li S. Y., et al., "Fabrication of off-axis aspheric surfaces using a slow tool servo", International Journal of Machine Tools and Manufacture, 51(5), 404-410 (2011).

Yi A. Y., Li L., "Design and fabrication of a microlens array by use of a slow tool servo", Optics letters, 30(13), 1707-1709 (2005).

Yi A. Y., Raasch T. W., "Design and fabrication of a freeform phase plate for high-order ocular aberration correction", Applied optics, 44(32), 6869-6876 (2005).

Yu D. P., Wong Y. S., Hong G. S., "Ultraprecision machining of micro-structured functional surfaces on brittle materials", Journal of micromechanics and microengineering, 21(9), 095011 (2011).

Zhang G., Ouyang R., Lu B., Hocken R., Veale R., & Donmez A., "A displacement method for machine geometry calibration", CIRP Annals-Manufacturing Technology, 37(1), 515-518 (1988).

Zhang G. X., Zhang Y. H., Yang S. M., et al., "A multipoint method for spindle error motion measurement", CIRP Annals-Manufacturing Technology, 46(1), 441-445 (1997).

Zhang S. J., To S., Cheung C. F., et al., "Dynamic characteristics of an aerostatic bearing spindle and its influence on surface topography in ultra-precision diamond turning", International Journal of Machine Tools and Manufacture, 62, 1-12 (2012).

Zhang S. J., To S., "A theoretical and experimental study of surface generation under spindle vibration in ultra-precision raster milling", International Journal of Machine Tools and Manufacture, 75, 36-45 (2013).

Zhang S. J., To S., "The effects of spindle vibration on surface generation in ultra-precision raster milling", International Journal of Machine Tools and Manufacture, 71, 52-56 (2013b).

Zhang X. D., Fang F. Z., Wang H. B., et al., "Ultra-precision machining of sinusoidal surfaces using the cylindrical coordinate method", Journal of Micromechanics and Microengineering, 19(5), 054004 (2009).

Zhang X., Gao H., Guo Y., et al., "Machining of optical freeform prisms by rotating tools turning", CIRP Annals-Manufacturing Technology, 61(1), 519-522 (2012).

Zhang X. D., Fang F. Z., Wu Q. Q., et al., "Coordinate transformation machining of off-axis aspheric mirrors", The International Journal of Advanced Manufacturing Technology, 67(9-12), 2217-2224 (2013a).

Zhang X., Fang F., Yu L. H., et al., "Slow slide servo turning of compound eye lens", Optical Engineering, 52(2), 023401-023401(2013b).

Zhu Z., Zhou X., Luo D., et al., "Development of pseudo-random diamond turning method for fabricating freeform optics with scattering homogenization", Optics express, 21(23), 28469-28482 (2013).

Zhu Z., Zhou X., Liu Z., et al., "Development of a piezoelectrically actuated two-degree-of-freedom fast tool servo with decoupled motions for micro-/nanomachining", Precision Engineering, 38(4), 809-820 (2014).

Zhu Z., To S., Zhang S., "Large-scale fabrication of micro-lens array by novel end-fly-cutting-servo diamond machining", Optics express, 23(16), 20593-20604 (2015).

Zhu Z., and To S., "Adaptive tool servo diamond turning for enhancing machining efficiency and surface quality of freeform optics", Optics express, 23(16), 20234-20248 (2015).

Ziegert J. C., & Mize C. D., "The laser ball bar: a new instrument for machine tool metrology", Precision engineering, 16(4), 259-267 (1994).